Repository Istituzionale dei Prodotti della Ricerca del Politecnico di Bari

Design and Characterization of Microwave and Optical Resonators for Biomedical Applications

This is a PhD Thesis

Original Citation:
Design and Characterization of Microwave and Optical Resonators for Biomedical Applications / Laneve, Dario. - ELETTRONICO. - (2020). [10.60576/poliba/iris/laneve-dario_phd2020]

Availability:
This version is available at http://hdl.handle.net/11589/191031 since: 2020-02-19

Published version
DOI:10.60576/poliba/iris/laneve-dario_phd2020
Politecnico di Bari

Terms of use:
Altro tipo di accesso

(Article begins on next page)

04 May 2024

LIBERATORIA PER L'ARCHIVIAZIONE DELLA TESI DI DOTTORATO

Al Magnifico Rettore del Politecnico di Bari

Il sottoscritto Dario Laneve, nato a Taranto il 10/12/1987, residente a Bisceglie in via Strada Pastore 15, e-mail dario.laneve@poliba.it, iscritto al 3° anno di Corso di Dottorato di Ricerca in Ingegneria Elettrica e dell'Informazione ciclo XXXII, essendo stato ammesso a sostenere l'esame finale con la prevista discussione della tesi dal titolo *Design and Characterization of Microwave and Optical Resonators for Biomedical Applications*

DICHIARA

1. di essere consapevole che, ai sensi del D.P.R. n. 445 del 28.12.2000, le dichiarazioni mendaci, la falsità negli atti e l'uso di atti falsi sono puniti ai sensi del codice penale e delle Leggi speciali in materia, e che nel caso ricorressero dette ipotesi, decade fin dall'inizio e senza necessità di nessuna formalità dai benefici conseguenti al provvedimento emanato sulla base di tali dichiarazioni;
2. di essere iscritto al Corso di Dottorato di Ricerca in Ingegneria Elettrica e dell'Informazione, ciclo XXXII, corso attivato ai sensi del "*Regolamento dei Corsi di Dottorato di ricerca del Politecnico di Bari"*, emanato con D.R. n.286 del 01.07.2013;
3. di essere pienamente a conoscenza delle disposizioni contenute nel predetto Regolamento in merito alla procedura di deposito, pubblicazione e autoarchiviazione della tesi di dottorato nell'Archivio Istituzionale ad accesso aperto alla letteratura scientifica;
4. di essere consapevole che attraverso l'autoarchiviazione delle tesi nell'Archivio Istituzionale ad accesso aperto alla letteratura scientifica del Politecnico di Bari (IRIS-POLIBA), l'Ateneo archivierà e renderà consultabile in rete (nel rispetto della Policy di Ateneo di cui al D.R. 642 del 13.11.2015) il testo completo della tesi di dottorato, fatta salva la possibilità di sottoscrizione di apposite licenze per le relative condizioni di utilizzo (di cui al sito http://www.creativecommons.it/Licenze), e fatte salve, altresì, le eventuali esigenze di "embargo", legate a strette considerazioni sulla tutelabilità e sfruttamento industriale/commerciale dei contenuti della tesi, da rappresentarsi mediante compilazione e sottoscrizione del modulo in calce (Richiesta di embargo);
5. che la tesi da depositare in IRIS-POLIBA, in formato digitale (PDF/A) sarà del tutto identica a quelle **consegnate**/inviate/da inviarsi ai componenti della commissione per l'esame finale e a qualsiasi altra copia depositata presso gli Uffici del Politecnico di Bari in forma cartacea o digitale, ovvero a quella da discutere in sede di esame finale, a quella da depositare, a cura dell'Ateneo, presso le Biblioteche Nazionali Centrali di Roma e Firenze e presso tutti gli Uffici competenti per legge al momento del deposito stesso, e che di conseguenza va esclusa qualsiasi responsabilità del Politecnico di Bari per quanto riguarda eventuali errori, imprecisioni o omissioni nei contenuti della tesi;
6. che il contenuto e l'organizzazione della tesi è opera originale realizzata dal sottoscritto e non compromette in alcun modo i diritti di terzi, ivi compresi quelli relativi alla sicurezza dei dati personali; che pertanto il Politecnico di Bari ed i suoi funzionari sono in ogni caso esenti da responsabilità di qualsivoglia natura: civile, amministrativa e penale e saranno dal sottoscritto tenuti indenni da qualsiasi richiesta o rivendicazione da parte di terzi;
7. che il contenuto della tesi non infrange in alcun modo il diritto d'Autore né gli obblighi connessi alla salvaguardia di diritti morali od economici di altri autori o di altri aventi diritto, sia per testi, immagini, foto, tabelle, o altre parti di cui la tesi è composta.

Luogo e data: Bari, 17/02/2020 Firma Laneve Dario

Il sottoscritto, con l'autoarchiviazione della propria tesi di dottorato nell'Archivio Istituzionale ad accesso aperto del Politecnico di Bari (POLIBA-IRIS), pur mantenendo su di essa tutti i diritti d'autore, morali ed economici, ai sensi della normativa vigente (Legge 633/1941 e ss.mm.ii.),

CONCEDE

- al Politecnico di Bari il permesso di trasferire l'opera su qualsiasi supporto e di convertirla in qualsiasi formato al fine di una corretta conservazione nel tempo. Il Politecnico di Bari garantisce che non verrà effettuata alcuna modifica al contenuto e alla struttura dell'opera;
- al Politecnico di Bari la possibilità di riprodurre l'opera in più di una copia per fini di sicurezza, back-up e conservazione.

Luogo e data: Bari, 17/02/2020 Firma Laneve Dario

Department of Electrical and Information Engineering
Electrical and Information Engineering
Ph.D. Program
SSD: ING-INF/02 – ELECTROMAGNETIC FIELDS

Final Dissertation

Design and Characterization of Microwave and Optical Resonators for Biomedical Applications

by

Dario LANEVE

Supervisor:

Prof. Francesco PRUDENZANO

Coordinator of Ph.D. Program:
Prof. Luigi Alfredo GRIECO

Course n° 32, 01/11/2016 – 31/10/2019

Department of Electrical and Information Engineering
Electrical and Information Engineering
Ph.D. Program
SSD: ING-INF/02 – ELECTROMAGNETIC FIELDS

Final Dissertation

Design and Characterization of Microwave and Optical Resonators for Biomedical Applications

by

Dario LANEVE

Referees:

Dr. Maurizio FERRARI

Dr. Gualtiero NUNZI CONTI

Supervisor:

Prof. Francesco PRUDENZANO

Coordinator of Ph.D. Program:
Prof. Luigi Alfredo GRIECO

Course n° 32, 01/11/2016 – 31/10/2019

Dedicated to the loving memory of my father.

ABSTRACT

In this Ph.D. dissertation, the feasibility investigation, design and characterization of different microwave and optical resonator devices with applications in the fields of medicine, such as cancer radiotherapy, and diagnostic, such as chemical/biological fluid sensing, is detailed. Different microwave and optical resonant structures have been considered, the common thread among them is related to the electromagnetic field theory and the exploitation of the resonance effect to improve their performance. Ad-hoc homemade computer codes have been developed, for accurate investigations, and validated via experimental data.

- The design and optimization of side-coupled proton linear accelerator microwave cavities via a novel hybrid numerical/analytical approach is reported in [1], [2]. Such microwave cavities are typically used in proton linear accelerators devoted to hadron therapy applications. The design hybrid approach has been validated through measurements. An excellent agreement between simulation and experiment has been found in terms of accelerator frequency (simulation: 2.997 916 GHz, experiment: 2.997 796 GHz) and accelerating field nonuniformity (simulation: 1.806 %, experiment: 1.585 %);

- By exploiting the same foregoing hybrid approach, the design and optimization of a novel proton linear accelerator based on on-axis coupled electromagnetic band-gap (EBG) cavities for hadron therapy applications is reported in [3]. The use of EBG cavities allows a very strong reduction (by about 65 %) of the peak surface electric field, paving the way to the design and fabrication of very high gradient proton linear accelerators.

- The design of optical whispering gallery mode (WGM) microresonators efficiently and selectively excited via tapered optical fibers and long period gratings is reported in [4]. The design has been well validated via experimental data. A microbubble-based set-up for chemical and biomedical fluid sensing has been also investigated [5], [6]. By proper coupling the WGMs with the tapered fiber modes, resonance shifts higher than i) −40 GHz/wt.% at 1550 nm and ii) −3 GHz/wt.% at 589 nm, have been calculated for a sodium chloride (NaCl) and glucose ($C_6H_{12}O_6$) fluid sensing set-ups, respectively.

The foregoing main research topics are detailed in this Ph.D. dissertation. In addition to them, during the three-year Ph.D. course, I have contributed to the following side research activities concerning microwave and optical electromagnetic field applications:

- the design and characterization of an optically transparent wideband graphene-based planar antenna for microwave applications (GPS, WiFi, Bluetooth, and 5G) [7]. In particular, I have performed the measurement of the gain and radiation pattern of the fabricated antenna through the anechoic chamber SATIMO StarLab, supplied by the "Electromagnetic Fields" laboratory led by Prof. Francesco Prudenzano;

- the design and characterization of a reconfigurable antenna loaded by a gated-graphene capacitor [8]. In particular, I have performed the measurement of the gain and radiation pattern of the fabricated antenna via the foregoing anechoic chamber SATIMO StarLab;

- the design of a pulsed Dy^{3+}:ZBLAN laser emitting at about 3 μm, by exploiting an in-band pumping scheme and the gain-switching regime for pulse generation [9]. In particular, I have contributed to the numerical homemade codes for the design of the pulsed Dy^{3+}:ZBLAN laser;

- the design of a multi-wavelength fiber laser based on Tm:Er:Yb:Ho co-doped germanate glass (simultaneous emission at 1550 nm, 1800 nm and 2050 nm) [10]. In particular, I have contributed to the numerical homemade codes for the design of the multi-wavelength fiber laser;

- the design and characterization of a microwave planar sensor for the dielectric assessment of different vegetable oils [11]. In particular, I have performed the fabrication of the microwave planar sensor by means of the PCB prototyping system LPKF ProtoLaser U3, supplied by the "Electromagnetic Fields" laboratory led by Prof. Francesco Prudenzano.

Finally, I have also contributed to two review papers reporting the recent advances on middle-infrared fiber lasers and photonic crystal fiber sensors [12], [13].

ACKNOWLEDGMENTS

These few words are really not enough to express my most heartfelt thanks to my Ph.D. Supervisor, Prof. Francesco Prudenzano. These three years of doctoral research activity (and not only that) spent with Prof. Prudenzano have contributed in a truly significant way to my scientific and technical education. And, above all, to my personal growth. The scientific insights, the enthusiastic encouragement and the constructive criticism which Prof. Prudenzano provided throughout my doctoral work have always been very helpful and very much appreciated.

I wish to thank my family for giving me a valuable moral support throughout my graduate and doctoral studies. In this regard, very special thanks go to my sweetheart, Roberta.

I would like to thank my colleagues and friends Giuseppe, Vincenza and Christian for their useful technical and humane suggestions.

I wish to thank my long-standing friends. They are my extended family. I am very grateful to them for their support.

Last but not least, I want to sincerely thank my father. I will be forever grateful to him for what he taught me. I am very proud to be his son.

Bari, October 2019 Dario Laneve

Ph.D. PUBLICATIONS

papers in international journals

[1] M. C. Falconi, D. Laneve, and F. Prudenzano, "Advances in Mid-IR Fiber Lasers: Tellurite, Fluoride and Chalcogenide," *Fibers*, vol. 5, no. 2, pp. 23–34, Jun. 2017. DOI: 10.3390/fib5020023.

[2] M. Grande, G. V. Bianco, D. Laneve, P. Capezzuto, V. Petruzzelli, M. Scalora, F. Prudenzano, G. Bruno, and A. D'Orazio, "Optically transparent wideband CVD graphene-based microwave antennas," *Appl. Phys. Lett.*, vol. 112, no. 25, 251103, Jun. 2018. DOI: 10.1063/1.5037409.

[3] F. Chiavaioli, D. Laneve, D. Farnesi, M. C. Falconi, G. Nunzi Conti, F. Baldini, and F. Prudenzano, "Long Period Grating-Based Fiber Coupling to WGM Microresonators," *Micromachines*, vol. 9, no. 7, 366, Jul. 2018. DOI: 10.3390/mi9070366.

[4] D. Laneve, M. C. Falconi, M. Bozzetti, G. Rutigliani, R. A. Prisco, V. Dimiccoli, and F. Prudenzano, "Electromagnetic Design of Microwave Cavities for Side-Coupled Linear Accelerators: A Hybrid Numerical/Analytical Approach," *IEEE Trans. Nucl. Sci.*, vol. 65, no. 8, pp. 2233–2239, Aug. 2018. DOI: 10.1109/TNS.2018.2851387.

[5] M. C. Falconi, D. Laneve, M. Bozzetti, T. T. Fernandez, G. Galzerano, and F. Prudenzano, "Design of an Efficient Pulsed Dy^{3+}:ZBLAN Fiber Laser Operating in Gain Switching Regime," *J. Lightw. Technol.*, vol. 36, no. 23, pp. 5327–5333, Dec. 2018. DOI: 10.1109/JLT.2018.2871665.

[6] D. Laneve, M. C. Falconi, M. Bozzetti, G. Rutigliani, R. A. Prisco, V. Dimiccoli, and F. Prudenzano, "Efficient hybrid approach to the electromagnetic design of resonant cavities for side-coupled linacs," *IET J. Eng.*, vol. 2019, no. 6, pp. 4617–4621, Mar. 2019. DOI: 10.1049/joe.2018.5145.

[7] V. Portosi, D. Laneve, M. C. Falconi, and F. Prudenzano, "Advances on Photonic Crystal Fiber Sensors and Applications," *Sensors*, vol. 19, no. 8, 1892, Apr. 2019. DOI: 10.3390/s19081892.

[8] M. Grande, G. V. Bianco, D. Laneve, P. Capezzuto, V. Petruzzelli, M. Scalora, F. Prudenzano, G. Bruno, and A. D'Orazio, "Gain and phase control in a graphene-loaded reconfigurable antenna," *Appl. Phys. Lett.*, vol. 115, no. 13, 133103, Sep. 2019. DOI: 10.1063/1.5111868.

[9] A. Ivanov, T. Agliullin, D. Laneve, V. Portosi, A. Vorobev, R. R. Nigmatullin, A. Nasybullin, O. Morozov, F. Prudenzano, A. D'Orazio, and M. Grande, "Design and Characterization of a Microwave Planar Sensor for Dielectric Assessment of Vegetable Oils," *Electronics*, vol. 8, no. 9, 1030, Sep. 2019. DOI: 10.3390/electronics8091030.

[10] M. C. Falconi, D. Laneve, V. Portosi, S. Taccheo, and F. Prudenzano, "Design of a Multi-wavelength Fiber Laser Based on Tm:Er:Yb:Ho Co-doped Germanate Glass," *J. Lightw. Technol.*, Jan. 2020, *early access*. DOI: 10.1109/JLT.2020.2966999.

[11] D. Laneve, V. Portosi, M. C. Falconi, G. Rutigliani, R. A. Prisco, V. Dimiccoli, and F. Prudenzano, "Design of Electromagnetic Band-Gap Cavities for High-Gradient On-Axis Coupled-Cavity Linear Accelerators," *IEEE Trans. Nucl. Sci.*, Oct. 2019, *submitted*.

PAPERS IN PROCEEDINGS OF INTERNATIONAL AND NATIONAL CONFERENCES

[12] D. Laneve, M. C. Falconi, G. Palma, A. Crudele, and F. Prudenzano, "Optical microresonators for biomedicine applications," in *Proc. ICTON 2017*, Girona, Spain, Jul. 2017, We.B4.4. DOI: 10.1109/ICTON.2017.8025017.

[13] M. C. Falconi, D. Laneve, C. Clemente, D. Gurban, T. T. Fernandez, G. Galzerano, and F. Prudenzano, "Global optimization via evolutionary approach of a Dy^{3+}:ZBLAN fiber amplifier for MID-IR applications," in *Proc. SPIE 2018*, vol. 10683, Strasbourg, France, May 2018, p. 106830L. DOI: 10.1117/12.2306473.

[14] M. C. Falconi, D. Laneve, M. Bozzetti, T. T. Fernandez, G. Galzerano, and F. Prudenzano, "Continuos-wave and pulsed optical fiber lasers for medium infrared applications," in *Proc. ICTON 2018*, Bucharest, Romania, Jul. 2018, Mo.B6.5. DOI: 10.1109/ICTON.2018.8473783.

[15] M. Grande, G. V. Bianco, D. Laneve, P. Capezzuto, V. Petruzzelli, M. Scalora, F. Prudenzano, G. Bruno, and A. D'Orazio, "Graphene for Optically Transparent Telecommunication Devices," in *Proc. ICTON 2018*, Bucharest, Romania, Jul. 2018, Mo.C2.2. DOI: 10.1109/ICTON.2018.8473815.

[16] D. Laneve, M. C. Falconi, F. Chiavaioli, D. Farnesi, G. Nunzi Conti, S. Soria, F. Baldini, and F. Prudenzano, "Optical coupling of spherical microresonators with tapered fibers for chemical/biomedical applications," in *Proc. MetroSea 2018*, Bari, Italy, Oct. 2018, pp. 247–251. DOI: 10.1109/MetroSea.2018.8657862.

[17] D. Laneve, M. C. Falconi, G. Palma, C. Scarnera, F. Chiavaioli, D. Farnesi, T. Kishi, A. Chiappini, G. Nunzi Conti, S. Soria, V. Nazabal, F. Baldini, M. Ferrari, and F. Prudenzano, "Passive and active whispering gallery mode microresonators in optical engineering," in *Proc. SPIE 2019*, vol. 10904, San Francisco, CA, US, Mar. 2019, p. 1 090 417. DOI: 10.1117/12.2512038.

[18] M. C. Falconi, D. Laneve, C. Clemente, G. Ricchiuti, A. Loconsole, V. Portosi, A. Crudele, G. Galzerano, and F. Prudenzano, "Fluoride Glass Pulsed Laser in Middle Infrared Wavelength Range," in *Proc. CLEO/Europe-EQEC 2019*, Munich, Germany, Jun. 2019, cj_p_33. DOI: 10.1109/CLEOE-EQEC.2019.8872425.

[19] M. C. Falconi, D. Laneve, V. Portosi, S. Taccheo, and F. Prudenzano, "Design of ultra-wideband Yb:Er:Tm:Ho co-doped germanate glass devices," in *Proc. ICTON 2019*, Angers, France, Jul. 2019, Th.B6.3. DOI: 10.1109/ICTON.2019.8840460.

[20] V. Marrocco, V. Basile, I. Fassi, M. Grande, D. Laneve, F. Prudenzano, and A. D'Orazio, "Dielectric Resonant Antennas via Additive Manufacturing for 5G Communications," in *Proc. PIERS 2019*, *in press*, Rome, Italy, 2019.

[21] M. C. Falconi, D. Laneve, V. Portosi, S. Taccheo, and F. Prudenzano, "Modeling of a 980-nm pumped Yb:Er:Tm:Ho co-doped glass device for homogeneous gain and lasing over a 600-nm wavelength interval," in *Proc. ASSL 2019*, Vienna, Austria, Oct. 2019, JTu3A.31. DOI: 10.1364/ASSL.2019.JTu3A.31.

[22] D. Laneve, M. C. Falconi, G. Palma, F. Chiavaioli, G. Nunzi Conti, G. C. Righini, C. Trono, and F. Prudenzano, "Microspheres and Microbubbles for Chemical and Biomedicine Optical Sensing," in *Proc. FOTONICA 2017*, Padua, Italy, Jun. 2017. DOI: 10.1049/cp.2017.0195.

[23] M. C. Falconi, D. Laneve, Y. Wang, T. T. Fernandez, G. Galzerano, and F. Prudenzano, "Modelling of Dysprosium-Doped ZBLAN Fiber Laser," in *Proc. FOTONICA 2017*, Padua, Italy, Jun. 2017. DOI: 10.1049/cp.2017.0194.

[24] M. C. Falconi, D. Laneve, M. Bozzetti, T. T. Fernandez, G. Galzerano, and F. Prudenzano, "Design of an In-Band Pumped Dysprosium-Doped ZBLAN Fiber Amplifier Operating at 2.9-3.2 Micron," in *Proc. RiNEm 2018*, Cagliari, Italy, Sep. 2018, pp. 229–232. [Online]. Available: http://www.elettromagnetismo.it/wp-content/uploads/2018/09/XXII-RiNEm-Conference-Proceedings.pdf.

ABSTRACTS OF INTERNATIONAL AND NATIONAL CONFERENCES

[25] D. Laneve, M. C. Falconi, G. Palma, F. Chiavaioli, G. Nunzi Conti, G. C. Righini, C. Trono, and F. Prudenzano, "Optical microresonators for chemical and biological sensing applications," presented at the 7th EOS Topical Meeting on Optical MicroSystems (OμS'17), Anacapri, Italy, Sep. 10–14, 2017.

[26] M. C. Falconi, D. Laneve, T. T. Fernandez, G. Galzerano, and F. Prudenzano, "Numerical modeling of a Dy^{3+}:ZBLAN fiber laser operating in gain switching regime," presented at the 7th International Workshop on Photoluminescence in Rare Earths: Photonic Materials and Devices (PRE'17), Rome, Italy, Nov. 30–Dec. 2, 2017.

[27] D. Laneve, M. C. Falconi, F. Chiavaioli, D. Farnesi, G. Nunzi Conti, S. Soria, F. Baldini, and F. Prudenzano, "Optical Resonators for Chemical/Biological Sensing," presented at the 1st International Conference on Dielectric Photonic Devices and Systems Beyond Visible (D-Photon 2018), Bari, Italy, Oct. 1–2, 2018.

[28] M. C. Falconi, D. Laneve, C. Clemente, A. Crudele, T. T. Fernandez, G. Galzerano, and F. Prudenzano, "Mid-IR Fiber Amplifier Based on Dysprosium-Doped ZBLAN Glass," presented at the 1st International Conference on Dielectric Photonic Devices and Systems Beyond Visible (D-Photon 2018), Bari, Italy, Oct. 1–2, 2018.

[29] M. C. Falconi, D. Laneve, and F. Prudenzano, "Feasibility Investigation of Fiber Lasers for Mid-IR applications," presented at the COST Action MP1401 4th Annual Conference, Warsaw, Poland, Oct. 24–26, 2018.

[30] D. Laneve, M. C. Falconi, G. Palma, V. Nazabal, F. Starecki, L. Bodiou, J. Charrier, and F. Prudenzano, "Rare Earth Doped Integrated Microcavities for Active Sensing Applications," presented at the 41st PhotonIcs & Electromagnetics Research Symposium (PIERS 2019), Rome, Italy, Jun. 17–20, 2019.

[31] D. Laneve, M. C. Falconi, F. Chiavaioli, D. Farnesi, G. Nunzi Conti, S. Soria, F. Baldini, and F. Prudenzano, "Optical Microcavities Resonances: Chemical and Biological Sensing Applications," presented at the 41st PhotonIcs & Electromagnetics Research Symposium (PIERS 2019), Rome, Italy, Jun. 17–20, 2019.

[32] M. C. Falconi, D. Laneve, S. Taccheo, and F. Prudenzano, "Design and Optimization of Wideband Spectrum Lasing," presented at the 41st PhotonIcs & Electromagnetics Research Symposium (PIERS 2019), Rome, Italy, Jun. 17–20, 2019.

[33] M. C. Falconi, D. Laneve, C. Clemente, G. Ricchiuti, A. Crudele, M. Bozzetti, V. Nazabal, I. T. Sorokina, and F. Prudenzano, "Mid-IR Supercontinuum Generation in Rare Earth-doped Optical Fibers," presented at the 41st PhotonIcs & Electromagnetics Research Symposium (PIERS 2019), Rome, Italy, Jun. 17–20, 2019.

[34] S. Berneschi, A. Barucci, F. Chiavaioli, M. C. Falconi, D. Farnesi, G. Frigenti, I. A. Grimaldi, D. Laneve, S. Pelli, G. Persichetti, S. Soria, G. Testa, C. Trono, F. Prudenzano, R. Bernini, and G. Nunzi Conti, "Managing Coupled Wavelengths and Modes in Waveguide-microresonator Systems," presented at the 41st PhotonIcs & Electromagnetics Research Symposium (PIERS 2019), Rome, Italy, Jun. 17–20, 2019.

[35] M. C. Falconi, D. Laneve, V. Portosi, S. Taccheo, and F. Prudenzano, "Numerical investigation of simultaneous lasing at three different wavelengths in an Yb:Er:Tm:Ho co-doped germanate glass," presented at the 8th International Workshop on Photoluminescence in Rare Earths: Photonic Materials and Devices (PRE'19), Nice, France, Sep. 4–6, 2019.

[36] D. Laneve, M. C. Falconi, G. Palma, V. Gallo, A. Rizzuti, F. Chiavaioli, G. Nunzi Conti, G. C. Righini, S. Soria, C. Trono, and F. Prudenzano, "Feasibility Investigation of Microspherical Resonators for Fluid Sensing in Medicine," presented at the 20th Italian National Conference on Photonic Technologies (FOTONICA 2018), Lecce, Italy, May 23–25, 2018.

[37] M. C. Falconi, D. Laneve, M. Bozzetti, T. T. Fernandez, G. Galzerano, and F. Prudenzano, "Design of a Gain-Switched Dy^{3+}:ZBLAN Fibre Laser," presented at the 20th Italian National Conference on Photonic Technologies (FOTONICA 2018), Lecce, Italy, May 23–25, 2018.

CONTENTS

LIST OF FIGURES xiii
LIST OF TABLES xiv
LIST OF ACRONYMS AND ABBREVIATIONS xiv
INTRODUCTION 1
1 COUPLED-CAVITY LINEAR ACCELERATORS THEORY 3
1.1 On-axis energy gain in an RF accelerating gap 4
1.2 Linac figures of merit 7
1.3 Coupled oscillators circuit model 8
1.4 Dispersion curve of biperiodic structures 11
1.5 Properties of the $\pi/2$ mode 11
1.6 Biperiodic linear accelerating structures 14
1.7 Finite-length CCL tanks: half-cells termination 16
1.8 Finite-length CCL tanks: full-cells termination 18
2 ELECTROMAGNETIC DESIGN OF MICROWAVE CAVITIES FOR SIDE-COUPLED LINEAR ACCELERATORS: A HYBRID NUMERICAL/ANALYTICAL APPROACH 20
2.1 Introduction 20
2.2 Design overview 21
2.2.1 HA code details 22
2.2.2 Design specifications 25
2.3 Simulation results 26
2.3.1 End Cells 29
2.4 Measurements 29
2.5 Concluding remarks 32
3 DESIGN OF ELECTROMAGNETIC BAND-GAP CAVITIES FOR HIGH-GRADIENT ON-AXIS COUPLED-CAVITY LINEAR ACCELERATORS 33
3.1 Introduction 33
3.2 Design overview 34
3.2.1 HA code details 35
3.2.2 Design specifications 36
3.3 Simulation results 36
3.3.1 End Cells 38
3.4 Performance comparison between SCL and EBG ACs 38
3.5 Concluding remarks 42
4 WHISPERING GALLERY MODE THEORY 47
4.1 Analytical model of a multilayer WGM microresonator 47
4.2 Coupling model 51
5 OPTICAL COUPLING OF WGM MICRORESONATORS WITH TAPERED FIBERS FOR CHEMICAL/BIOLOGICAL SENSING APPLICATIONS 53
5.1 WGM-based sensing applications 53
5.2 Overview of the WGM microresonator-taper coupling system 54
5.3 Manufacturing of WGM microresonators, tapers and LPGs . . 54
5.4 Design and experimental validation of the coupling system . . 56
5.4.1 Microsphere-based set-up 56
5.4.2 Microbubble-based set-up 58
5.5 Microbubbles for chemical/biological fluid sensing 60
5.6 Concluding remarks 66
CONCLUSION 67

BIBLIOGRAPHY 69

LIST OF FIGURES

Figure 1.1 Periodic disk-loaded cylindrical waveguide 3
Figure 1.2 RF accelerating gap 4
Figure 1.3 Stable synchronous phase for longitudinal focusing . 5
Figure 1.4 Equivalent circuit model of a CCL 8
Figure 1.5 Dispersion curve of a CCL 12
Figure 1.6 Electric field patterns for 0, $\pi/2$, and π modes 13
Figure 1.7 Biperiodic linear accelerating structures 15
Figure 1.8 Half-cells termination of finite-length CCLs 16
Figure 1.9 Full-cells termination of finite-length CCLs 18
Figure 2.1 CAD sketches of the SCL's ACs and CCs 22
Figure 2.2 Boundary conditions for simulating SCL quintuplets . 23
Figure 2.3 Flowchart of the HA code 24
Figure 2.4 Convergence of the HA code 28
Figure 2.5 Fabricated five-cavity SCL tank with end cells (ECs) . 30
Figure 2.6 Simulated and measured longitudinal electric field intensity 31
Figure 3.1 CAD sketches of the EBG's ACs and CCs 34
Figure 3.2 3D sketch of a full EBG accelerating cavity 35
Figure 3.3 Accelerating electric field distribution in the optimized EBG tank 39
Figure 3.4 On-axis electric field intensity in the optimized EBG tank 40
Figure 3.5 Dispersion curves of the optimized SCL and EBG tanks 42
Figure 3.6 Longitudinal wakefields in the EBG and SCL tanks . . 43
Figure 3.7 Transverse wakefields in the EBG and SCL tanks . . . 44
Figure 3.8 Transverse wake potentials for each mode in the EBG and SCL tanks 45
Figure 4.1 Multilayer WGM sphere resonator coupled with a tapered fiber 48
Figure 4.2 Cross-section of a multilayer WGM sphere resonator . 48
Figure 5.1 Simulated WGM microresonator-taper coupling system 54
Figure 5.2 Microsphere and microbubble-based set-ups 55
Figure 5.3 Microsphere-based set-up: simulation vs experiment 57
Figure 5.4 Microsphere-based set-up: transmittance vs gap . . . 58
Figure 5.5 Microbubble-based set-up: simulation vs experiment 59
Figure 5.6 Microbubble-based set-up: transmittance vs gap . . . 60
Figure 5.7 Electric field distribution in microbubble and taper . . 61
Figure 5.8 Microbubble-based NaCl sensor: $WGM_{1149,1149,1}$ coupled with $LP_{0,10}$ 62
Figure 5.9 Microbubble-based NaCl sensor: $WGM_{1117,1117,2}$ coupled with $LP_{0,12}$ 63
Figure 5.10 Microbubble-based NaCl sensor: $WGM_{1067,1067,3}$ coupled with $LP_{0,12}$ 63
Figure 5.11 Microbubble-based NaCl sensor: detuning shift vs concentration 64
Figure 5.12 Microbubble-based $C_6H_{12}O_6$ sensor: detuning shift vs concentration 65

LIST OF TABLES

Table 2.1 SCL design: HA tank period calculation settings . . . 26
Table 2.2 SCL design: ACs and CCs optimized geometrical parameters . . . 27
Table 2.3 SCL design: ACs and CCs constant geometrical parameters . . . 27
Table 2.4 SCL design: HA optimization settings . . . 27
Table 2.5 EM parameters of the optimized SCL cavities . . . 29
Table 3.1 EBG design: ACs and CCs optimized geometrical parameters . . . 36
Table 3.2 EBG design: ACs and CCs constant geometrical parameters . . . 37
Table 3.3 EM parameters of the optimized EBG cavities . . . 38
Table 3.4 Performance comparison between the SCL ACs and the EBG ACs . . . 40
Table 5.1 Refractive index dispersion of an aqueous NaCl solution 62
Table 5.2 Refractive index dispersion of an aqueous $C_6H_{12}O_6$ solution . . . 65

LIST OF ACRONYMS AND ABBREVIATIONS

AC	accelerating cavity
CC	coupling cavity
CCL	coupled-cavity linac
em	electromagnetic
EBG	electromagnetic band-gap
EC	end cell
FEM	finite element method
FSR	free spectral range
HA	hybrid approach
HOM	high-order mode
linac	linear accelerator
LP	linearly polarized
LPG	long period grating
NIR	near infrared
OACL	on-axis-coupled linac
PEC	perfect electric conductor
PMC	perfect magnetic conductor
PML	perfect matched layer
PSO	particle swarm optimization

RF	radio frequency
SCL	side-coupled linac
TE	transverse electric
TM	transverse magnetic
VNA	vector network analyzer
WGM	whispering gallery mode

INTRODUCTION

In recent years, the role of microwave and optical resonator devices in the fields of the medicine diagnostic and biological investigations is considerably increased, opening the way for novel opportunities and interesting applications. The huge potential and flexibility of resonant electromagnetic fields can be effectively exploited in chemical and biomedical applications ranging from microwave to optical frequencies. For instance, electromagnetic fields resonating at microwave frequencies are at the basis of adavanced real-time mini- or non-invasive diagnostic systems for cancer radiation therapy using particle linear accelerators (linacs). On the other hand, several applications in biology, health care and environmental monitoring can greatly benefit from the exploitation of optical resonances arising in sub-millimeter dielectric structures.

An innovative form of radiotherapy, known as hadron therapy (or particle therapy), has been recently established as a new technique in therapeutic treatment of tumors [14]. It basically consists of cancerous tissues irradiation by means of high-energy heavy ion beams, in partricular protons and carbon ions [14]–[16]. In fact, the depth-dose energy distributions of protons and carbon ions interacting with the matter largely increase at the end of their path, where a narrow peak (Bragg peak) arises. This is a favourable feature when treating deep-seated and radioresistant tumours, i.e. tumours tissues which are less sensitive to the conventional X rays irradiation than the surrounding healthy tissues. Microwave cavity-based particle linacs are very promising for the development of precise and high target selectivity hadron therapy machines. In fact, linacs have several advantages compared to other particle accelerators, such as synchrotrons and cyclotrons: i) they are modular, each accelerating module can be powered by independently controlled pulsed klystrons; ii) the output beam energy can be continuously varied on a pulse-to-pulse basis, by adjusting the amplitude and/or phase of the klystron RF pulses; iii) the tumour target can be covered several times by applying the spot scanning technique [15]; iv) very low proton currents are enough to deliver the typical doses required by the cancer treatment protocols; v) there is no power loss from synchrotron radiation, beacuse of the linear path traversed by the particle beam; vi) beam injection and extraction are simpler than in circular accelerators, beacuse of the open ends of the linacs; vii) high-intensity charged-particle beams of high beam quality (i. e. small beam diameter and energy spread) can be produced through linacs [17]. The fabrication and acceleration tests of the first 3-GHz proton linac prototype devoted to the hadron therapy is described in [18]. It was based on a well-known coupled-cavity accelerating structure, known as side-coupled linac (SCL) [19], in which a proton beam was accelerated from 62 to 74 MeV by an average electric field of 16 MV/m. Since then, a number of design and fabrication projects involving proton linacs for hadron therapy have been undertaken [20]–[24].

In addition to microwave resonators, optical dielectric microresonator-based devices are also fundamental in a wide class of applications, including chemical sensing and label-free detection of biomolecules [25]–[27]. Optical resonators are also very promising for diagnosing different cancer biomarkers [28]–[32]. Optical resonators allow light to be confined in very compact volumes where hundreds of roundtrips takes place. This dramatically increases the interaction

length with the surroinding environment, compared to waveguide-based sensors, in which light–matter interaction is limited by single-pass propagation. This aspect can greatly help the detection of low concentration analytes and it is related to the high quality factor which optical microresonators typically exhibit. Other remarkable properties of optical microresonator-based set-ups are compactness, low response time, immunity to electromagnetic interference and limited fabrication costs. The most common optical resonators are Fabry-Pérot cavities and whispering gallery mode (WGM) resonators. In Fabry-Pérot cavities the light oscillation is achieved by using mirrors [33], which is a well-established and simple method. However, Fabry-Pérot cavities suffer from the limited compactness and the low integration density, resulting in poor suitability for modern photonics applications. A valuable alternative to Fabry-Pérot cavities, especially in the fields of biology and medicine, is given by dielectric microcavities with circular geometries, such as rings, disks, spheres, bubbles and toroids [34]–[43]. The light propagation in such microcavities are described by the well-known WGM theory [44]. WGM resonators are characterized by very high power density, extremely small mode volume, very narrow spectral linewidth, very high quality factors, potentially low material absorption and minimal reflection losses [44]. All these properties make the WGM resonators very attractive for developing chemical and biosensing applications.

In view of the foregoing discussion, this thesis has been devoted to the theoretical study, design, optimization and characterization of novel devices and systems for biomedical/chemical and environmental diagnosis applications, based on microwave and optical resonant structures. In particular:

THE FIRST CHAPTER illustrates the analytical theory describing the coupled-cavity linacs (CCLs), which has been exploited for the electromagnetic design of radio frequency (RF) CCL-based particle accelerators;

THE SECOND CHAPTER describes a novel hybrid analytical/numerical approach for the design and optimization of the coupled microwave cavities of an SCL. The experimental validation of the design hybrid approach is also reported;

THE THIRD CHAPTER illustrates the design of a novel proton linac based on on-axis coupled electromagnetic band-gap (EBG) cavities, by means of the same foregoing hybrid approach. The performance comparison with the SCL cavities is also reported;

THE FOURTH CHAPTER reports a general and comprehensive theoretical model concerning multilayer WGM microresonators evanescently coupled to input/ouput optical waveguides;

THE FIFTH CHAPTER illustrates the design and characterization of novel WGM microresonator-based coupling systems for efficient and selective addressing of (quasi-)distributed WGM microresonators via tapered optical fibers and long period gratings (LPGs). The use of a microbubble-based coupling system for chemical/biological sensing applications has been also investigated.

1 COUPLED-CAVITY LINEAR ACCELERATORS THEORY

An electromagnetic (em) field can provide energy gain to an electrically charged moving particle, if the following two conditions are met [17]:

1. the em field must have an electric component with the same direction of the particle motion;

2. the propagating em field and the moving particle must have the same velocity to maintain synchronism.

The first condition can be satisfied by a transverse magnetic (TM) em field propagating in a uniform cylindrical waveguide. But the second condition is not satisfied for a uniform cylindrical waveguide, because $v_p > c$, where v_p is the phase velocity of the field and c is the speed of light in vacuum [45]. In order to have an accelerating field with a phase velocity $v_p < c$, accelerating structures with periodic geometries are effectively used. In this regard, a periodic slow-wave accelerating structure can be viewed as [17]:

1. a periodically loaded cylindrical waveguide in which the phase velocity of the propagating em field is reduced by the reflections from the periodic loading elements;

2. a periodic array of coupled resonators.

As an example, in Figure 1.1 a periodic disk-loaded cylindrical waveguide accelerating structure is shown. The disk-loaded structure in Figure 1.1 can be also viewed as a periodic array of pillbox cavities coupled through irises. This coupled-cavity picture allows to formulate an analytic description for the dispersion curve of the accelerating structure as well as analytical formulas for estimating the cavity coupling constants [46]–[48].

The monoperiodic disk-loaded waveguide in Figure 1.1 is effectively used as an accelerating structure for relativistic particles. Electron linacs are typically designed as disk-loaded waveguides, since electrons are so light that their velocity is already relativistic at injection from the electron gun. For accelerating heavier ions, such as protons, resonantly-coupled linear

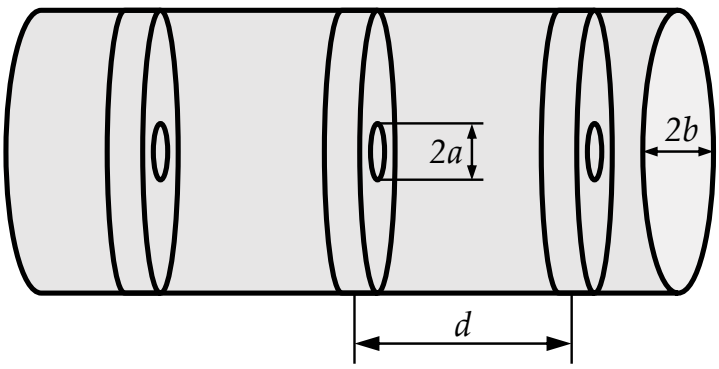

Figure 1.1: Periodic disk-loaded, or iris-loaded, cylindrical waveguide. The waveguide radius is b. The iris radius is a. The distance between two adjacent loading disks, i. e. the spatial period, is d.

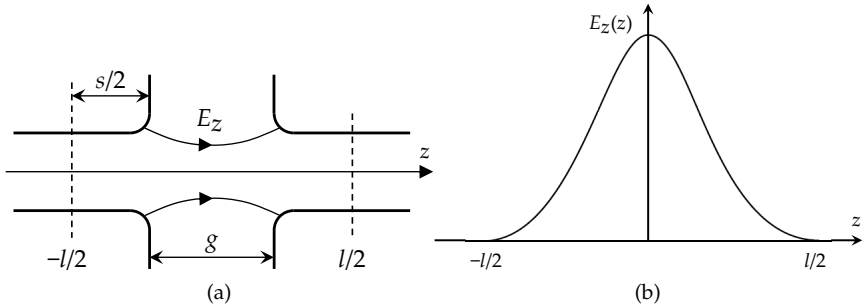

Figure 1.2: (a) RF accelerating gap geometry. A sketch of the on-axis electric field lines is also shown. The gap length, g, is within an axial distance, l, including the drift space, s. (b) RF electric field distribution on the beam propagation axis. (Adapted from [17])

accelerators (linacs) are instead used, including the biperiodic coupled-cavity linacs (CCLs) [17].

In this chapter, the general concepts pertaining to the energy gain of charged particles from a radio frequency (RF) electric field confined within an accelerating gap are first introduced. The typical design figures of merit used to assess the performance of linac cavities are also listed. Then, an equivalent circuit model to analytically described the CCLs will be illustrated. The remarkable properties of the accelerating $\pi/2$ mode of the CCLs will be described. Moreover, suitable boundary conditions will be considered for modelling finite-length biperiodic CCLs with preserved em field distribution and symmetry.

1.1 ON-AXIS ENERGY GAIN IN AN RF ACCELERATING GAP

In all RF accelerators, the energy gain is provided to the particle beam by an RF electric field, which must be synchronous with the beam for a efficient energy transfer. In particular, multicavity RF linacs are designed to produce a given energy/velocity gain per cavity. To do this, a reference particle, known as the synchronous particle, is considered. The synchronous particle is an ideal particle whose velocity at each instant of time equals the phase velocity of the accelerating field. That is, the synchronous particle enters each linac cavity with the same correct velocity (phase). Thus, the synchronous particle gains the same right amount of energy to maintain exact synchronism with the accelerating fields. As will be described in Section 1.6, the velocity of the synchronous particle is used to design the accelerating cavity lengths. The synchronous particle is also fundamental for providing longitudinal focusing and stable output beam intensity, as described in the following.

Energy is transferred to particles from a TM_{010}-like standing-wave em field having the electric component along the direction of the particle motion. An example of an RF accelerating gap is shown in Figure 1.2a. The gap, g, is centered on an axial distance, l, which includes the drift space, s. The drift space prevent particles from interacting with a reverse-phase field when particles transit from one gap to the next one. The on-axis electric field, $E_z(z)$, experienced by the synchronous particle moving along the z-axis with a velocity $v(z)$ is [17], [49]

$$E_z(r = 0, z, t) = E(0, z)\cos[\omega t(z) + \phi_s], \tag{1.1}$$

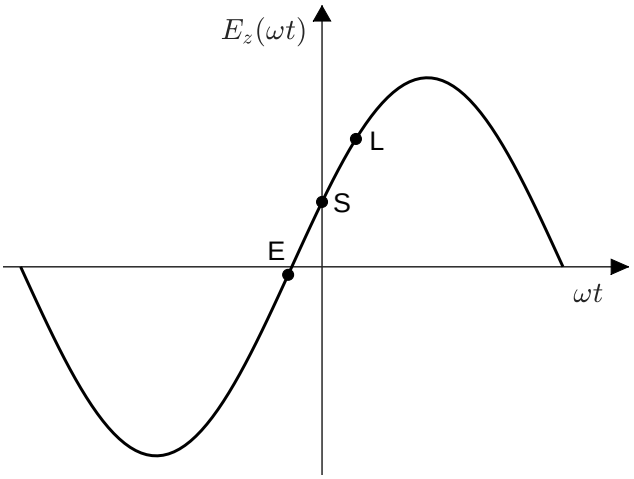

Figure 1.3: Time variation of the on-axis electric field within an accelerating gap. The three points are the stable (S), early (E), and late (L) phases pertaining to the particle beam longitudinal focusing.

where $t(z) = \int_0^z v(z)\,\mathrm{d}z$ is the time the particle is at position z; ω is the RF frequency; ϕ_s is the synchronous phase, i. e. the phase of the synchronous particle. The on-axis electric field confined within the axial distance l is shown in Figure 1.2b. At the time $t = 0$, the phase of the field relative to the crest is ϕ_s, as shown in Figure 1.3, where it can be seen that $\phi_s < 0$. At first glance, a negative synchronous phase might seem unreasonable since a synchronous particle with $\phi_s = 0$ would experience the maximum electric field strength, so the maximum energy gain. Actually, the crest of the field is not a stable point for particle acceleration [17], [49]. In fact, all particles entering a cavity with a phase $\phi \neq \phi_s$ would experience a lower electric field, a lower energy gain and a lower acceleration. In the next cavity, such particles would experience an even lower electric field and acceleration, and so on. The final effect is a strong longitudinal defocusing, since particles slip behind in phase and do not experience any net acceleration, leading to a very unstable output beam. In contrast, longitudinal restoring forces exist when the beam is accelerated by an electric field that is rising in time [17], [49]. That is, the synchronous phase, ϕ_s, is chosen corresponding to the stable point S shown in Figure 1.3. It is a stable point because nearby particles arriving earlier than the synchronous particle (labeled E in Figure 1.3) experience a smaller electric field, and particles arriving later (labeled L in Figure 1.3) will experience a larger electric field. In the next accelerating gap, the previous early particles are now late particles and the previous late particles are now early particles. By going on, the nearby particles will oscillate about the stable phase, with an oscillation amplitude that decreases as the beam energy increases, i. e. when particles approach relativistic velocities [17], [49]. In summary, choosing $\phi_s < 0$, with the accelerating field rising in time, provides longitudinal phase stability.

A general equation for energy gain can be derived from the electric field expression in (1.1). The energy gain of an arbitrary particle with charge q and phase ϕ traveling through the accelerating gap shown in Figure 1.2a is [17], [49]

$$\Delta W = qV_0T\cos\phi, \tag{1.2}$$

where

$$V_0 = \int_{-l/2}^{l/2} E(0,z)\,\mathrm{d}z \tag{1.3}$$

is the on-axis RF voltage, and

$$T = \frac{\int_{-l/2}^{l/2} E(0,z)\cos[\omega t(z)]\,\mathrm{d}z}{\int_{-l/2}^{l/2} E(0,z)\,\mathrm{d}z} - \tan\phi \frac{\int_{-l/2}^{l/2} E(0,z)\sin[\omega t(z)]\,\mathrm{d}z}{\int_{-l/2}^{l/2} E(0,z)\,\mathrm{d}z}, \tag{1.4}$$

is the so-called transit-time factor. The axial RF voltage in (1.3) can be written as $V_0 = E_0 l$, where E_0 is the average electric field over the axial distance, l, traversed by the particle beam. The product $E_0 T$ is known as the accelerating gradient [17]. E_0 is a fundamental quantity to take into account in a linac design, because it directly determines the energy performance of a linac. The higher the accelerating gradient the higher the energy gain. But, the value of E_0 is mainly limited by power consumption constraints and the RF electric breakdown.

To better understand the physical meaning of the transit-time factor, T, the expression in (1.4) is simplified by removing its dependence on the phase ϕ. To do this, the following considerations can be done:

1. both the phase and the transit-time factor depend on the origin, which can be arbitrarily chosen within the gap. It is convenient to choose the origin at the electrical center of the gap, such that

$$\int_{-l/2}^{l/2} E(0,z)\sin[\omega t(z)]\,\mathrm{d}z = 0;$$

2. $E_z(z)$ is usually at least approximately an even function about the geometric center of the gap. That is, the electrical center and the geometric center are at least approximately the same.

In view of the two aforesaid considerations, the transit-time factor, T, can be reformulated as

$$T = \frac{\int_{-l/2}^{l/2} E(0,z)\cos[\omega t(z)]\,\mathrm{d}z}{\int_{-l/2}^{l/2} E(0,z)\,\mathrm{d}z} = V_0^{-1}\int_{-l/2}^{l/2} E(0,z)\cos[\omega t(z)]\,\mathrm{d}z. \tag{1.5}$$

Thus, the transit-time factor, T, is the ratio of the energy gain in a harmonically time-varying RF electric field to the energy gain in a constant DC electric field equal to E_0, which is the field seen by the particle at the center of the gap. The transit-time factor, T, is effectively an acceleration efficiency, since it expresses the reduction in the energy gain caused by the sinusoidal time variation of the accelerating field in the gap.

Generally, the particle acceleration in a single gap is small. By neglecting the velocity change, $\omega t \approx \omega z/v = 2\pi z/\beta\lambda$, where $\beta = v/c$ is the fractional particle velocity, λ is the RF wavelength in vacuum, and $\beta\lambda$ is the distance the particle travels in an RF period. Then, the transit-time factor, T, is

$$T = \frac{\int_{-l/2}^{l/2} E(0,z)\cos(2\pi z/\beta\lambda)\,\mathrm{d}z}{\int_{-l/2}^{l/2} E(0,z)\,\mathrm{d}z} = V_0^{-1}\int_{-l/2}^{l/2} E(0,z)\cos\left(\frac{2\pi z}{\beta\lambda}\right)\mathrm{d}z. \tag{1.6}$$

The transit-time factor increases when the field is more concentrated longitudinally near the origin, due to the presence of the cosine factor. We

will see later that a common practice to increase the transit-time factor is to use protrusions, called nose cones, on the beam line that extend into the gap in order to reduce the effective gap length and increase the electric field concentration near the center of the gap.

1.2 LINAC FIGURES OF MERIT

Before getting in greater details on the CCL theory, the figures of merit that are commonly used to assess the accelerating performance of any linac cavity are described in this section. Most of them depend only on the power dissipated on the walls of the cavities. The well-known intrinsic quality factor, Q_0, is a typical figure of merit of any cavity resonator and it is defined as

$$Q_0 = \omega U/P, \tag{1.7}$$

where ω is the cavity resonant frequency, U is the stored energy and P is the power loss due to the non-zero electrical resistance of the cavity walls.

Another figure of merit is the shunt impedance, r_s, desfined as

$$r_s = V_0^2/P. \tag{1.8}$$

The shunt impedance is the effectiveness of producing an axial voltage V_0 for a given power loss P and it is usually expressed in MΩ. To take into account the reduction in the energy gain caused by the sinusoidal time variation of the accelerating field, the effective shunt impedance is defined as

$$r = (V_0T)^2/P = r_sT^2. \tag{1.9}$$

The effective shunt impedance is the effectiveness of delivering energy to a particle per unit power loss. Effective shunt impedance is also expressed in MΩ. In a linac design, both r_s and r can be maximized to increase the (effective) voltage gain for a given power loss.

Since $V_0 = E_0l$ and P increase linearly with the length l, it is also convenient to introduce shunt impedances per unit length. The shunt impedance per unit length, Z, is

$$Z = r_s/l = E_0^2/(P/l). \tag{1.10}$$

Similarly, the effective shunt impedance per unit length, ZT^2, is

$$ZT^2 = r/l = (E_0T)^2/(P/l). \tag{1.11}$$

The units of Z and ZT^2 are usually MΩ/m. Especially for normal-conducting cavity design, the energy gain in a given length for a given power loss can be maximized through ZT^2 or Z. Another useful design parameter is the ratio of the effective shunt impedance to the quality factor, the so-called "r over Q" [17], defined as

$$r/Q = (V_0T)^2/\omega U. \tag{1.12}$$

The parameter r/Q is usually expressed in Ω and it represents the efficiency of acceleration per unit stored energy at a given frequency. In a similar way, the ratio ZT^2/Q can be defined. Both these ratios are a function only of the cavity geometry, and does not depend on the surface properties that determine the power losses.

The peak surface electric field, E_s, is also a fundamental constraint in linac cavities design. In fact, especially for normal-conducting cavities, if E_s is too large, RF electric breakdown phenomena may arise causing physical damage

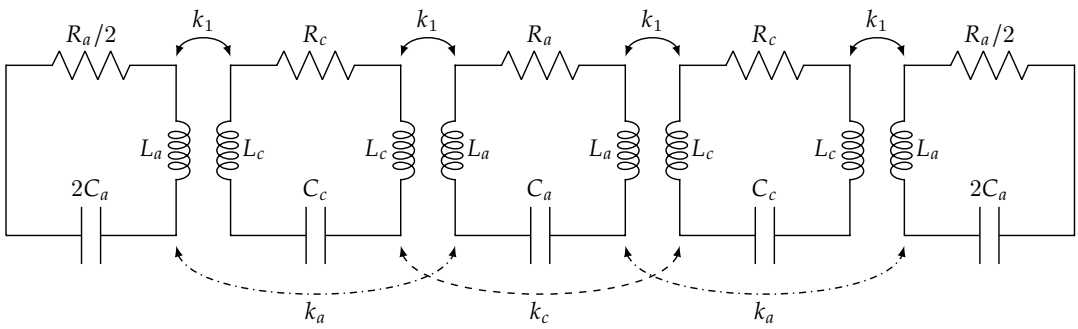

Figure 1.4: Equivalent coupled-oscillators circuit model of a biperiodic CCL. The subscript "a" refers to the ACs, while the subscript "c" refers to the CCs.

to the cavities. To avoid this, the Kilpatrick's criterion [50] can be used to limit the peak surface electric field to a maximum value defined as [17]

$$E_s = bE_k, \tag{1.13}$$

where b is called bravery factor and E_k, which is known as the Kilpatrick limit, is calculated via the following formula

$$f = 1.64E_k^2 \mathrm{e}^{-8.5/E_k}, \tag{1.14}$$

where f is the cavity frequency in MHz, and E_k is expressed in MV/m. Typical values chosen for b are in the range from 1 to 2. It is worth noting that, for higher frequencies, larger values of E_s are allowed, making possible the use of higher design accelerating gradients.

1.3 COUPLED OSCILLATORS CIRCUIT MODEL

A microwave cavity resonator can be viewed as an equivalent RLC circuit oscillator [45]. Therefore, a biperiodic chain of coupled cavities, such as a CCL, can be effectively analyzed in terms of coupled RLC oscillators [51]. "Biperiodic" means that the spatial period of the linac consists of two different cavity resonators, i. e. having different geometries and resonant frequencies. One cavity is devoted to the beam acceleration, so it is referred to as accelerating cavity (AC). The other cavity is mainly used for coupling two adjacent ACs and it is known as coupling cavity (CC). In Figure 1.4 the equivalent circuit of a CCL consisting of five cavitie, or cells, is shown. Each oscillator is coupled to the adjacent ones via the nearest-neighbor coupling constant, k_1. The oscillators of the same type (i. e., having the same electrical characteristics) are coupled to each other via the next-nearest-neighbor coupling constants, k_a and k_c [51], [19]. The end oscillators have half the inductance and twice the capacitance of the middle oscillator, in order to have the same unloaded resonant frequency, i. e. when no coupling is considered. Such end oscillators represent half-length cavities, that is cavities with a conducting plane in the center to provide perfect reflecting symmetry. This is a convenient way to model the end cavities, making the finite-length coupled resonator chain in Figure 1.4 look like an infinite periodic structure (image theory [52]). More details on the most appropriate boundary conditions for designing finite-length CCLs will be given in Section 1.7 and Section 1.8.

By numbering from 0 to 4 the RLC loops in Figure 1.4 and by applying the Kirchhoff's voltage law around any loop, the following circuit equations are obtained:[1]

$$\left(\jmath\omega_q L_a + \frac{R_a}{2} + \frac{1}{\jmath 2C_a}\frac{1}{\omega_q}\right) i_0 + \jmath\omega_q M_1 i_1 + \jmath\omega_q M_a i_2 = 0, \tag{1.15a}$$

$$\left(\jmath\omega_q 2L_c + R_c + \frac{1}{\jmath C_c}\frac{1}{\omega_q}\right) i_1 + \jmath\omega_q M_1(i_0 + i_2) + \jmath\omega_q M_c i_3 = 0, \tag{1.15b}$$

$$\left(\jmath\omega_q 2L_a + R_a + \frac{1}{\jmath C_a}\frac{1}{\omega_q}\right) i_2 + \jmath\omega_q M_1(i_1 + i_3) + \jmath\omega_q M_a(i_0 + i_4) = 0, \tag{1.15c}$$

$$\left(\jmath\omega_q 2L_c + R_c + \frac{1}{\jmath C_c}\frac{1}{\omega_q}\right) i_3 + \jmath\omega_q M_1(i_2 + i_4) + \jmath\omega_q M_c i_1 = 0, \tag{1.15d}$$

$$\left(\jmath\omega_q L_a + \frac{R_a}{2} + \frac{1}{\jmath 2C_a}\frac{1}{\omega_q}\right) i_4 + \jmath\omega_q M_1 i_3 + \jmath\omega_q M_a i_2 = 0, \tag{1.15e}$$

where ω_q, $q = 0, \ldots, 4$, is the resonant frequency of the oscillating mode q of the entire chain; $M_1 = k_1\sqrt{L_a L_c}$, $M_a = k_a L_a$ and $M_c = k_c L_c$ are the mutual inductances for coupling between the oscillators, k_1, k_a and k_c being the coupling constants. Then, by dividing

1. (1.15a) and (1.15e) by $\jmath\omega_q\sqrt{L_a}$,
2. (1.15c) by $\jmath\omega_q 2\sqrt{L_a}$,
3. (1.15b) and (1.15d) by $\jmath\omega_q 2\sqrt{L_c}$,

the circuit equations can be written in the following form:

$$\left(1 - \frac{\omega_a^2}{\omega_q^2} + \frac{1}{\jmath 2Q_a}\frac{\omega_a}{\omega_q}\right) x_0 + k_1 x_1 + k_a x_2 = 0, \tag{1.16a}$$

$$\left(1 - \frac{\omega_c^2}{\omega_q^2} + \frac{1}{\jmath 2Q_c}\frac{\omega_c}{\omega_q}\right) x_1 + \frac{k_1}{2}(x_0 + x_2) + \frac{k_c}{2}x_3 = 0, \tag{1.16b}$$

$$\left(1 - \frac{\omega_a^2}{\omega_q^2} + \frac{1}{\jmath 2Q_a}\frac{\omega_a}{\omega_q}\right) x_2 + \frac{k_1}{2}(x_1 + x_3) + \frac{k_a}{2}(x_0 + x_4) = 0, \tag{1.16c}$$

$$\left(1 - \frac{\omega_c^2}{\omega_q^2} + \frac{1}{\jmath 2Q_c}\frac{\omega_c}{\omega_q}\right) x_3 + \frac{k_1}{2}(x_2 + x_4) + \frac{k_c}{2}x_1 = 0, \tag{1.16d}$$

$$\left(1 - \frac{\omega_a^2}{\omega_q^2} + \frac{1}{\jmath 2Q_a}\frac{\omega_a}{\omega_q}\right) x_4 + k_1 x_3 + k_a x_2 = 0, \tag{1.16e}$$

where

- $\omega_a = 1/\sqrt{2L_a C_a}$, Q_a and $x_{2n} = i_{2n}\sqrt{L_a}$ are the unloaded resonant frequency, intrinsic quality factor and normalized currents of the even oscillators (ACs), respectively;
- $\omega_c = 1/\sqrt{2L_c C_c}$, Q_c and $x_{2n+1} = i_{2n+1}\sqrt{L_c}$ are the unloaded resonant frequency, intrinsic quality factor and normalized currents of the odd oscillators (CCs), respectively.

1 A clockwise direction for the electric current in any loop is considered.

The circuit equations from (1.16a) to (1.16e) can be easily generalized for an arbitrary number of coupled oscillators as

$$\left(1-\frac{\omega_a^2}{\omega_q^2}+\frac{1}{j2Q_a}\frac{\omega_a}{\omega_q}\right)x_{2n}+\frac{k_1}{2}(x_{2n-1}+x_{2n+1})+\frac{k_a}{2}(x_{2n-2}+x_{2n+2})=0, \tag{1.17a}$$

$$\left(1-\frac{\omega_c^2}{\omega_q^2}+\frac{1}{j2Q_c}\frac{\omega_c}{\omega_q}\right)x_{2n+1}+\frac{k_1}{2}(x_{2n}+x_{2n+2})+\frac{k_c}{2}(x_{2n-1}+x_{2n+3})=0, \tag{1.17b}$$

where the subscripts $2n$ and $2n\pm 2$, $n=0,1,2,\dots$, refer to the even-numbered oscillators (ACs), while the subscripts $2n\pm 1$ and $2n+3$, $n=0,1,2,\dots$, refer to the odd-numbered oscillators (CCs). The coupled equations (1.17a) and (1.17b) can be expressed in terms of an eigenvalue problem as

$$L\boldsymbol{X}_q=\frac{1}{\omega_q^2}\Omega\boldsymbol{X}_q, \tag{1.18}$$

where, by neglecting losses,

$$L=\begin{bmatrix} 1 & k_1 & k_a & 0 & 0 & 0 & 0 & 0 & \dots & 0\\ \frac{k_1}{2} & 1 & \frac{k_1}{2} & \frac{k_c}{2} & 0 & 0 & 0 & 0 & \dots & 0\\ \frac{k_a}{2} & \frac{k_1}{2} & 1 & \frac{k_1}{2} & \frac{k_a}{2} & 0 & 0 & 0 & \dots & 0\\ 0 & \frac{k_c}{2} & \frac{k_1}{2} & 1 & \frac{k_1}{2} & \frac{k_c}{2} & 0 & 0 & \dots & 0\\ 0 & 0 & \frac{k_a}{2} & \frac{k_1}{2} & 1 & \frac{k_1}{2} & \frac{k_a}{2} & 0 & \dots & 0\\ \dots & \dots & \dots & \dots & \dots & \dots & \dots & \dots & \dots & \dots \end{bmatrix}, \tag{1.19}$$

$$\Omega=\mathrm{diag}(\omega_a^2,\omega_c^2,\omega_a^2,\omega_c^2,\omega_a^2,\dots) \tag{1.20}$$

are matrix operators, which are function of the cavity frequencies and the coupling constants.[2] For a finite resonator chain, the system in (1.18) can be solved analytically by finding the eigenfrequencies ω_q of the cavity chain eigenmodes. Each eigenfrequency is associated with the eigenvector $\boldsymbol{X}_q=[x_0,x_1,x_2,x_3,x_4,\dots]^\intercal$ whose elements are the normalized currents x_{2n} and x_{2n+1}. Such currents represent the normalized amplitudes of the electric fields in each cavity resonator. Thus, $\boldsymbol{X}_q$ is effectively the electric field pattern of the resonator chain operating in the (eigen)mode q.

By assuming a cosine-like behaviour of the standing-wave cavity fields, the solutions of the coupled equations (1.17a) and (1.17b) are [17], [51], [19]

$$x_{2n}=A\cos 2n\phi,$$
$$x_{2n+1}=B\cos(2n+1)\phi,$$

where $\phi=\pi q/2N$, $q=0,1,\dots,2N$, is the phase advance per cavity of the mode q propagating at the frequency ω_q; A and B are arbitrary amplitude constants. By substituting the above expressions of x_{2n} and x_{2n+1} in (1.17a) and (1.17b), one finds that

$$\frac{k_1\cos\phi}{\omega_a^2/\omega_q^2-k_a\cos 2\phi-1}=\frac{\omega_c^2/\omega_q^2-k_c\cos 2\phi-1}{k_1\cos\phi} \tag{1.21}$$

2 In the first row of the matrix L, the boundary conditions $x_{-1}=x_1$ and $x_{-2}=x_2$ must be considered [53].

and the dispersion relation of the biperiodic chain of an arbitrary number of coupled oscillators is

$$k_1^2 \cos^2 \phi = \left(1 - \frac{\omega_a^2}{\omega_q^2} + k_a \cos 2\phi\right)\left(1 - \frac{\omega_c^2}{\omega_q^2} + k_c \cos 2\phi\right) \tag{1.22}$$

The dispersion relation in (1.22) states that the resonant frequencies, ω_q, of a CCL have a periodic dependence on the longitudinal wavenumber $k_z = \phi/L$, where L is the spatial period of the CCL. For finite-length CCLs, the solutions ω_q of (1.22) takes on a finite discrete set of values, the number of solutions being equal to the number of cavities. In the limit of an infinite CCL, ϕ is a continuos variable and the dispersion relation in (1.22) can be graphically represented by a continuos curve.

1.4 DISPERSION CURVE OF BIPERIODIC STRUCTURES

The dispersion relation (1.22) is described by two different frequency intervals, known as lower passband and upper passband (see Figure 1.5a). The solutions of (1.22), i. e. the eigenfrequencies ω_q, are found in the two passbands. Each passband represents the dispersion curve of either the monoperiodic chain of coupled ACs or the monoperiodic chain of coupled CCs in itself. The two passbands are separated by a stopband, in which no solutions to the (1.22) exist. As depicted in Figure 1.5a, the stopband SB is practically the difference between the frequency solutions of (1.22) when $\phi = \pi/2$, i. e.

$$SB = |\omega_{\pi/2}^{ac} - \omega_{\pi/2}^{cc}|, \quad \omega_{\pi/2}^{ac} = \frac{\omega_a}{\sqrt{1-k_a}}, \quad \omega_{\pi/2}^{cc} = \frac{\omega_c}{\sqrt{1-k_c}}. \tag{1.23}$$

The stopband is removed when $\omega_{\pi/2}^{ac} = \omega_{\pi/2}^{cc}$.[3] In such case, the frequency of the highest mode of the lower passband (ω_1 in Figure 1.5a) coincides with the frequency of the lowest mode of the upper passband (ω_2 in Figure 1.5a). The joining of the two passbands is called confluence and the accelerating structure is said to be compensated [17], [49]. In fact, at confluence of the passbands, the slopes of the dispersion curves increase from zero to a maximum value (see Figure 1.5b). As a consequence, the group velocity also increases to a maximum value thereby improving the power flow along the tuned structure and the mode spacing on its dispersion curve.

1.5 PROPERTIES OF THE $\pi/2$ MODE

The oscillating mode of the entire coupled resonator chain in Figure 1.4 depends on the cavity-to-cavity phase shift, ϕ. Therefore, the value of ϕ is among the first design specifications a linac designer have to choose, along with the linac operating frequency. Typical ϕ values considered for designing a linac are

- $\phi = 0$ (0 mode): the instantaneous electric field in one cavity is in phase with the instantaneous electric fields in the adjacent cavities (Figure 1.6a). The normalized electric field pattern of the 0 mode is $\boldsymbol{X}_0 = [1, 1, 1, 1, 1, \dots]^\intercal$;
- $\phi = \pi/2$ ($\pi/2$ mode): a 90° phase shift arises between the instantaneous electric fields in adjacent cavities (Figure 1.6b). The normalized electric field pattern of the $\pi/2$ mode is $\boldsymbol{X}_{\pi/2} = [1, 0, -1, 0, 1, \dots]^\intercal$;

3 In real scenarios, ACs and CCs are never perfectly tuned. Nevertheless, if $\omega_{\pi/2}^{ac} \cong \omega_{\pi/2}^{cc}$, the stopband is negligible.

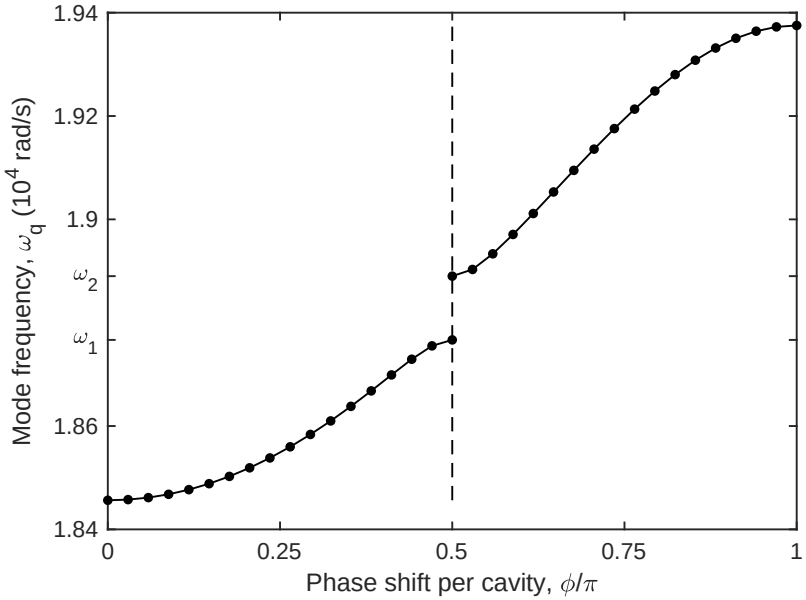

(a)

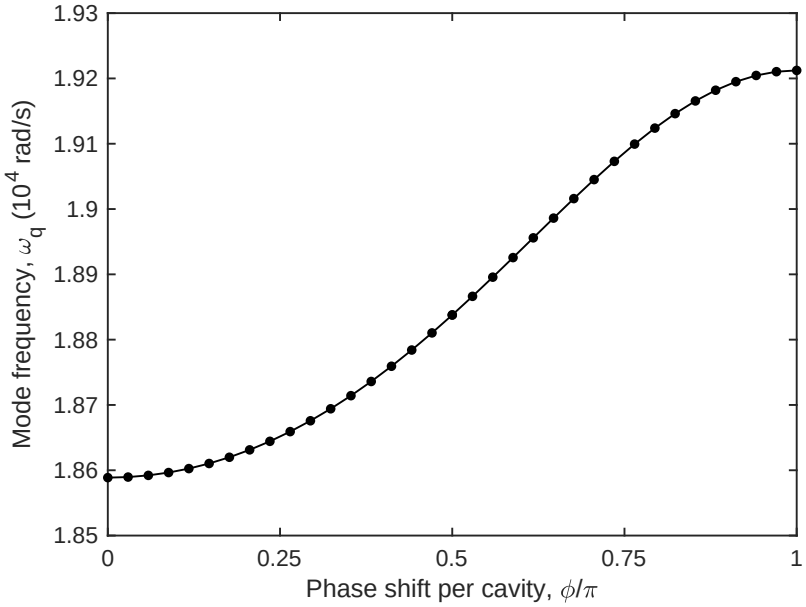

(b)

Figure 1.5: Dispersion curve of a biperiodic chain (CCL) of 35 cavities. The black dots are the chain eigenfrequencies, ω_q. (a) Open stopband (passbands not at confluence). (b) Closed stopband (passbands at confluence).

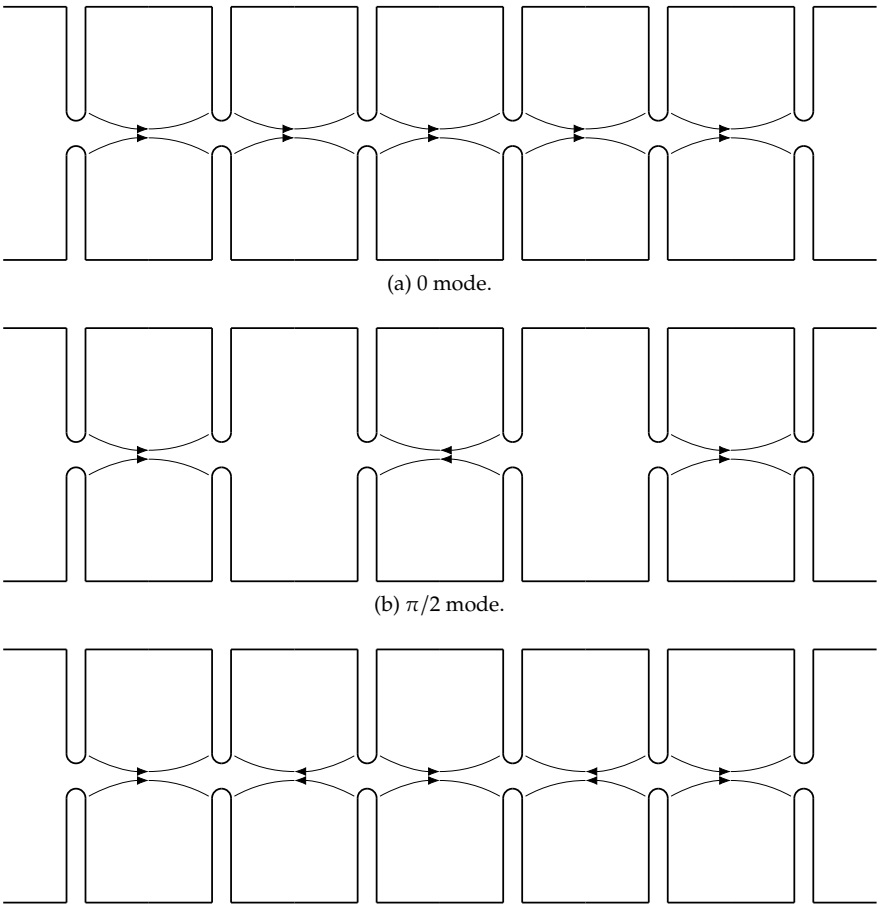

(a) 0 mode.

(b) $\pi/2$ mode.

(c) π mode.

Figure 1.6: Sketches of the instantaneous electric field distribution for (a) 0, (b) $\pi/2$ and (c) π phase shift per cavity. The electric field direction rotates to be in phase with the motion of the beam particles as they move from one cavity to the other after a time $\Delta t = \phi/\omega_q$, where ω_q is the resonant frequency of the coupled-cavity chain.

- $\phi = \pi$ (π mode): a 180° phase shift arises between the instantaneous electric fields in adjacent cavities (Figure 1.6c). The normalized electric field pattern of the π mode is $\boldsymbol{X}_\pi = [1, -1, 1, -1, 1, \dots]^\intercal$;

The $\pi/2$ mode has remarkable properties that make it more attractive than the 0 and π modes for particle acceleration, especially in CCL structures.

The $\pi/2$ mode is substantially independent of frequency errors in the individual cavities. It has been demonstrated via perturbation theory how frequency errors of the individual cavities affect the field amplitudes in terms of perturbed eigenvectors [17], [51], [19]. This means that the components of the perturbed eigenvectors are no longer unity, even though they are still real (i. e., frequency errors does not affect the phase of the cavity fields). In particular, fractional frequency errors of the form $\delta\omega/\omega$ appear as first-order corrections to the elements of $\boldsymbol{X}_\pi$ and $\boldsymbol{X}_0$, resulting in nonuniform field distributions which can be very sensitive to frequency errors of single cavities. By contrast, for the $\pi/2$ mode, fractional frequency errors of the form $\delta\omega/\omega$ appear as first-order corrections only to the fields of the odd-numbered oscillators (CCs), which are nominally unexcited in a perfectly tuned lossless case. The fields of the excited even-numbered oscillators (ACs) are affected only by second-order

corrections [17], thus being very insensitive to any small frequency errors. This remarkable advantage of the $\pi/2$ mode is very important for achieving field stability and relaxing the manufacturing tolerances.

The $\pi/2$ mode is also substantially independent of the resistive power losses due to cavity walls and beam loading. It has been demonstrated that, when losses are considered in the coupled-resonator circuit model, the amplitudes in the eigenvectors $\boldsymbol{X}_q$ become complex. In particular, losses produce an additional phase shift between adjacent oscillators in both the 0 and π modes, which decreases for increasing cavity coupling constant and Q factors [17], [51], [19]. Such additional phase shift, known as power-flow phase shift, can greatly alter the phase velocity of the accelerating field. By contrast, no power-flow phase shift exists for the $\pi/2$ mode. In the $\pi/2$ mode, losses only produce an excitation of the nominally unexcited odd-numbered oscillators which is in quadrature to the fields in the excited even-numbered oscillators. Moreover, small loss-dependent amplitude variations may occur in excited oscillators away from the RF drive point (an effect known as power-flow droop). However, for most cases of interest involving high Q factors, this two effects are negligible.

The $\pi/2$ mode has the greatest distance from the adjacent modes. As discussed in the Section 1.4, when the stopband is closed and the two passbands join at confluence, the dispersion curve in Figure 1.5b is obtained. It can be clearly seen that the 0 and π modes, i. e. the first and last points, respectively, on the dispersion curve, have poor mode spacing compared with the $\pi/2$ mode (the central point), due to the zero slope of the curve at the end points. This effect is more deleterious as the number of cavities (modes) increases. Since variations of the mode frequencies may occur due to losses, temperature fluctuations, manufacturing errors and so on, the major risk is to excite unwanted modes due to overlap with the desired mode. For weak coupling, $k_1 \ll 1$, in a chain of $N+1$ cavities the relative frequency spacing between the π mode and the closest mode is approximately

$$\frac{\delta\omega}{\omega} = k_1 \left(\frac{\pi}{2N}\right)^2 \tag{1.24}$$

For the $\pi/2$ mode, assuming again $k_1 \ll 1$, the distance from the nearest mode is given by

$$\frac{\delta\omega}{\omega} = k_1 \left(\frac{\pi}{2N}\right) \tag{1.25}$$

Hence, for equal coupling and for equal number of cavities (at least $N > 2$), the $\pi/2$ mode has a closest-mode frequency spacing which is greater than that pertaining to the π mode.

1.6 BIPERIODIC LINEAR ACCELERATING STRUCTURES

A CCL consists of a sequence of multicavity tanks. Each tank in turn consists of a biperiodic array of magnetically-coupled ACs and CCs. Each tank can be theoretically described in terms of coupled circuit oscillators (Section 1.3), where identical accelerating cells alternate with identical coupling cells. This means considering the approximation of equal-length ACs in a given tank, since the velocity change of the beam particles in a CCL tank is typically small [17]. As already said at the beginning of this chapter, the synchronism between the accelerating fields and the particle beam is fundamental in order to have a properly operating linac. This also depends on the cavity lengths. For the $\pi/2$ mode to accelerate a particle beam in a given CCL tank, the center-to-center

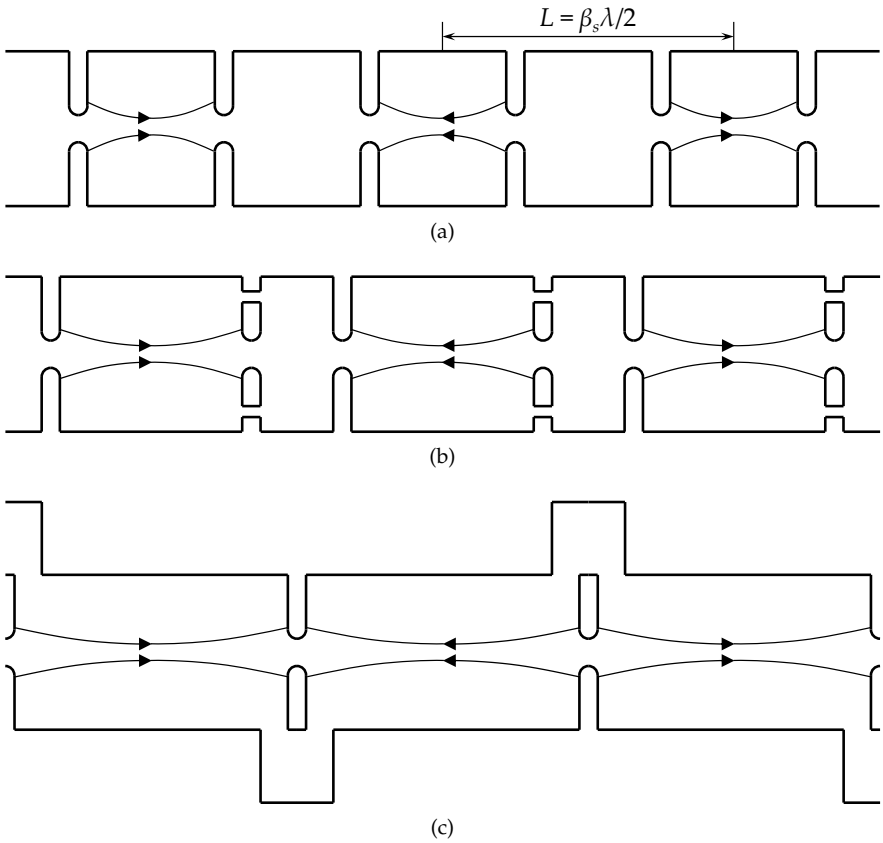

Figure 1.7: Linac configurations for $\pi/2$ mode operation. (a) conventional periodic cavity chain. (b) biperiodic on-axis-coupled cavity chain. (c) biperiodic side-coupled cavity chain. In (b) and (c), the magnetic coupling field lines are not shown.

distance between two consecutive excited cavities must be $L = \beta_s \lambda/2$, where β_s is the fractional velocity of the synchronous particle in that tank, and λ is the wavelength of the $\pi/2$ mode. The distance L is traversed by the beam particles in half an RF period, after this time the electric field is again in phase with the moving particles. This synchronism condition leads to the configuration shown in Figure 1.7a, where equal-length cavities are on the beam line and the excited ACs alternate with the unexcited CCs. This configuration have a lower shunt impedance compared with the π mode. In fact, only half of the available cavities contribute to acceleration, while, for the π mode, all cavities contribute to acceleration (see Figure 1.6b). This leads to larger power losses to produce the same energy gain, since the accelerating fields are concentrated in half of the available space.

A solution for retaining the unique properties of the $\pi/2$ mode described in the Section 1.5, and simultaneously achieving an higher shunt impedance, is to limit the space occupied by the unexcited CCs on the beam line, while optimizing the geometry of the excited ACs for high shunt impedance. The two most popular biperiodic linac structures for optimal $\pi/2$ mode operation are the on-axis-coupled structure and the side-coupled structure, which are shown in Figure 1.7b and Figure 1.7c, respectively [17], [19], [49]. In on-axis-coupled linacs (OACLs), the CCs are still on the beam line , but have a smaller length than the ACs. In side-coupled linacs (SCLs), the CCs are completely removed from the beam line, leaving it available only to the ACs. For both

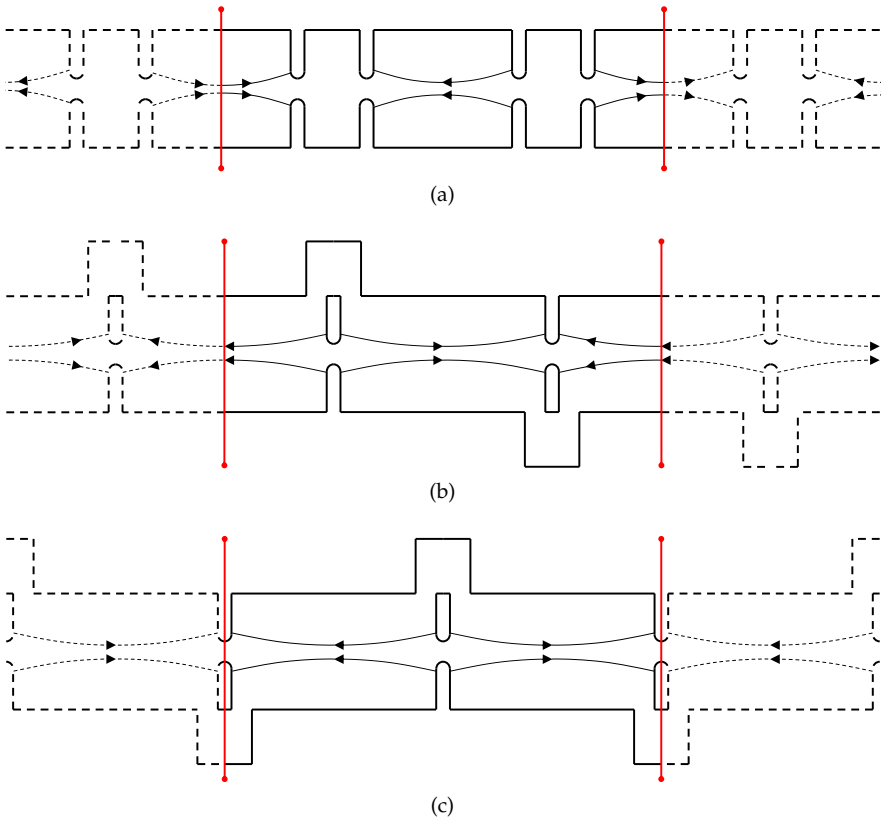

Figure 1.8: Half-cells termination of biperiodic CCL tanks of five cavities. The red lines are conducting metal plates used to build the half-cells. (a) OACL tank with half ACs termination (the magnetic coupling slots are not shown). (b) SCL tank with half ACs termination (broken symmetry). (c) SCL tank with half CCs termination (preserved symmetry).

linac structures in Figures 1.7b–1.7c, the magnetic coupling between ACs and CCs is exploited through slots cut in the outer inductive region of each cavity, where the RF magnetic field of the TM_{010}-like mode is dominant (the magnetic field lines are not shown in Figures 1.7b–1.7c). In particular, in on-axis-coupled configurations where the CCs are shorter than the ACs, the magnetic coupling apertures on one cavity end wall are rotated by a certain angle from the apertures on the opposite end wall, to avoid direct magnetic coupling between the ACs. For example, in Figure 1.7b, two magnetic coupling slots per wall are shown, the slots on the opposite walls are rotated by 90°.

1.7 FINITE-LENGTH CCL TANKS: HALF-CELLS TERMINATION

The dispersion curve and the cavity fields distribution of an actual finite-length CCL tank can be different from the theoretical ones pertaining to an infinite perfectly periodic structure. This also depends on the tank termination. In Figure 1.4, half ACs are used to provide a proper termination to make the finite-length oscillators chain look like an infinite one, according to the image theory [52]. To better illustrate this concept, in Figure 1.8a an OACL tank of five cavities (quintuplet) closed with half ACs is shown. By reflecting the quintuplet around the conducting symmetry planes (the red lines), an ideal infinitely-long tank is obtained. Thus, a finite number of cavities (eigenmodes)

is sufficient to obtain the same em field distribution of an infinite periodic structure.

The half ACs termination of an SCL quintuplet is shown in Figure 1.8b. In this case, the symmetry of an infinite SCL structure is broken, since the reflected CC coupled to each half AC are in the same semispace of the real CC. The broken symmetry alters the frequency and coupling constant of the half ACs from those of the interior ACs. The major negative effect is a dependence of $\omega_{\pi/2}$ from the number of ACs, n_{ACs} [22], [54], [55]. In particular, $\omega_{\pi/2}$ lowers with increasing n_{ACs}. In the limit of $n_{\text{ACs}} \to \infty$, the effect of the broken symmetry is negligible and $\omega_{\pi/2} \to \omega_{\pi/2}^{AC}$, as given in (1.23). A minor effect of the broken symmetry is the larger coupling constant of the real CCs, due to the reduced distance from the reflected CCs [56]. A correct SCL quintuplet termination is shown in Figure 1.8c, where half CCs are used as end cavities. In this case the symmetry of an infinte SCL chain is preserved, as do the cavity stored energies and coupling constants [22].

In an actual linac design, one of the first steps is choosing the phase shift per cavity, ϕ, and the operating frequency, ω_q, of the linac oscillating mode. It is not possible, or at least very difficult, to predict the final values that the single cavity frequencies and coupling constants will assume. The only quantities that can be found by direct measurements or 3D simulations are the eigenfrequencies, ω_q, of the resonant linac modes. Thus, a reverse eigenvalue problem in (1.18) arises: the frequencies ω_a and ω_c, and the coupling constants k_1, k_a and k_c, contained in the matrix operators L and Ω have to be found starting from the eigenvalues ω_q^{-2} of the cavity chain. Since there are five unknown parameters, a set of five eigenfrequencies, ω_q, $q = 0, \ldots, 4$, is needed. This means that the resonant modes of a five-cavities tank have to be measured or simulated. The OACL quintuplet shown in Figure 1.8a and the SCL quintuplet shown in Figure 1.8c are correctly described by the dispersion relation in (1.22). Since $\phi = \pi q/2N$, for $2N + 1$ cavities, each value of ϕ gives an equation. Thus, the following system of five polynomial equations can be written [22]:

$$\begin{cases} \left(1 - \dfrac{\omega_a^2}{\omega_0^2} + k_a\right)\left(1 - \dfrac{\omega_c^2}{\omega_0^2} + k_c\right) = k_1^2, & q = 0, \\ \left(1 - \dfrac{\omega_a^2}{\omega_1^2}\right)\left(1 - \dfrac{\omega_c^2}{\omega_1^2}\right) = \dfrac{k_1^2}{2}, & q = 1, \\ \left(1 - \dfrac{\omega_a^2}{\omega_2^2} - k_a\right)\left(1 - \dfrac{\omega_c^2}{\omega_2^2} - k_c\right) = 0, & q = 2, \\ \left(1 - \dfrac{\omega_a^2}{\omega_3^2}\right)\left(1 - \dfrac{\omega_c^2}{\omega_3^2}\right) = \dfrac{k_1^2}{2}, & q = 3, \\ \left(1 - \dfrac{\omega_a^2}{\omega_4^2} + k_a\right)\left(1 - \dfrac{\omega_c^2}{\omega_4^2} + k_c\right) = k_1^2, & q = 4. \end{cases} \tag{1.26}$$

The system can be easily solved to obtain the five unknowns $[f_a, f_c, k_1, k_a, k_c]^\intercal$. It should be noted that in Figure 1.8c, the excited cavities are now the even-numbered CCs, while the odd-numbered ACs are unexcited. This may seem inconsistent with the previous sections, but the half CCs termination in Figure 1.8c have to be used only to solve the polynomial system in (1.26). In general, $\omega_{\pi/2}$ is calculated through the resonant frequency of the excited cavities. That is, by solving the polynomial system in (1.26), the solution $\omega_{\pi/2} = \omega_2 = \omega_a/\sqrt{1 - k_a}$ is chosen for an OACL quintuplet, while the solution $\omega_{\pi/2} = \omega_2 = \omega_c/\sqrt{1 - k_c}$ is chosen for an SCL quintuplet.

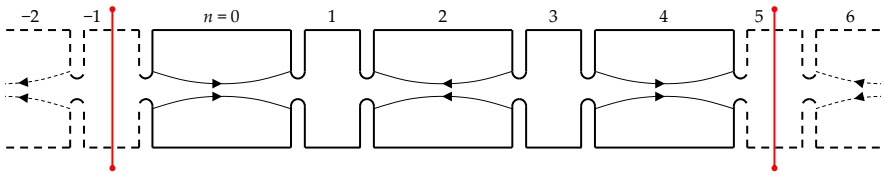

Figure 1.9: Sketch of an OACL quintuplet closed with full end cells (the magnetic coupling slots are not shown.). The red lines are conducting metal plates used to reflect the quintuplet around phantom unexcited half CCs. The dashed-line cavities result from the mirroring.

1.8 FINITE-LENGTH CCL TANKS: FULL-CELLS TERMINATION

In Section 1.7, the boundary conditions for a proper termination of finite-length biperiodic accelerating structures have been given in terms of half-cells. Such boundary conditions allow to correctly calculate the cavity loaded frequencies and coupling constants through the measured or simulated resonant modes of the biperiodic structures. But, to build a cavity as a half-cell, a conducting metal plane must be placed on the beam axis at the center of the cavity. Thus, the half-cells are useful for modeling and measurements, but can not be used in practice for acceleration since the conducting planes would prevent the propagation of the particle beam. In practice, full ACs, also referred to as end cells (ECs), are used for tank termination on both ends. The ECs are different than the other ACs in the tank because each EC is coupled with only one CC. Thus, the ECs termination can break the periodicity of the tank. However, for the $\pi/2$ mode, the symmetry of the em field distribution is preserved if the ECs are tuned to a slightly different resonant frequencies from that of the other ACs. In Figure 1.9 a sketch of an OACL quintuplet closed with the ECs is shown. Each end cavity is coupled to a CC on one side and has the beam pipe on the other side. Now, let's suppose to add a phantom CC next to each EC, by imposing the requirement that the phantom CC has no field excitation. By placing a conducting plane in the middle of the phantom CC, the quintuplet structure can be reflected around the conducting plane. An antisymmetric boundary condition must be imposed on the reflected cavities, in order to have the correct field pattern of the $\pi/2$ mode [53], [57].[4] To better explain the full ECs termination, the coupled resonators circuit model can be again invoked to describe the cavity chain shown in Figure 1.9. We will focus on the first two cavities of the quintuplet, but the following also applies to the last two cavities. The circuit equations pertaining to the first two cavities, in the lossless case, are

$$\left(1 - \frac{\omega_a^2}{\omega_q^2}\right) x_0 + \frac{k_1}{2}(x_1 + x_{-1}) + \frac{k_a}{2}(x_2 + x_{-2}) = 0, \tag{1.27a}$$

$$\left(1 - \frac{\omega_c^2}{\omega_q^2}\right) x_1 + \frac{k_1}{2}(x_0 + x_2) + \frac{k_c}{2}(x_3 + x_{-1}) = 0. \tag{1.27b}$$

By imposing the aforesaid antisymmetric boundary conditions, $x_{-1} = 0$ and $x_{-2} = -x_0$, the (1.27b) reduces to the (1.16b) and the equation pertaining to the end cell become

$$\left(1 - \frac{\omega_a^2}{\omega_q^2} - \frac{k_a}{2}\right) x_0 + \frac{k_1}{2} x_1 + \frac{k_a}{2} x_2 = 0. \tag{1.28}$$

4 These considerations apply to any CCL structure, including the side-coupled one.

By comparing the (1.28) with the (1.16a), an extra term occurs only in the coefficient of x_0. To have the same circuit equations and same solutions, the resonant frequency of the ECs, ω_e, must satisfy the relation

$$1 - \frac{\omega_e^2}{\omega_q^2} = 1 - \frac{\omega_a^2}{\omega_q^2} - \frac{k_a}{2},$$

which, for the $\pi/2$ mode, gives the correct detuning for matched ECs

$$\omega_e^2 = \omega_a^2 \frac{1 - k_a/2}{1 - k_a} = \omega_{\pi/2}^2 \left(1 - \frac{k_a}{2}\right). \tag{1.29}$$

By tuning the ECs to the frequency ω_e, the eigenvector of the $\pi/2$ mode will give the desired field pattern, i. e. ACs with same electric fields and stored energies and CCs with no excitations.

2 ELECTROMAGNETIC DESIGN OF MICROWAVE CAVITIES FOR SIDE-COUPLED LINEAR ACCELERATORS: A HYBRID NUMERICAL/ANALYTICAL APPROACH

In this chapter, a homemade computer code for designing the coupled microwave cavities of a proton linac is detailed [1], [2]. To this aim, a hybrid approach, based on both analytical and numerical investigations, is exploited. A finite element method (FEM) based on 2D/3D electromagnetic simulation software is used to find the eigenmodes and eigenfrequencies of the accelerator cavities as well as the typical figures of merit pertaining to the accelerating cavities. The design hybrid approach also includes a multi-objective particle swarm optimization (PSO) technique in order to automatically optimize the geometry of the accelerating tanks. The hybrid design strategy described in the following is general, allowing the optimization of a wide class of coupled-cavity resonant structures. The computer code is validated via measurements on a 3-GHz standing-wave side-coupled linac tank of five cavities closed with suitable end cells. The proton beam input energy is 27-MeV. An excellent agreement between simulation and experiment is found.

2.1 INTRODUCTION

Multicavity structures are effectively used for both electromagnetic field coupling and particle beam acceleration or spatial/velocity beam modulation in a number of applications, including high-power microwave sources, relativistic klystron amplifiers, microwave rebuncher cavities, microwave plasma sources, novel sheet-beam klystrons, magnetron combining, and linear particle accelerators [15], [18], [58]–[68]. In such applications, the number of geometrical parameters to be optimized is very high [17]. Moreover, in the design of SCLs, accurate electromagnetic simulations must be performed to obtain the eigenfrequencies and eigenmodes of i) the linac tanks), ii) the ACs and iii) the CCs. In ii) and iii), the loading effect due to the mutual coupling of ACs and CCs must be taken into account to minimize the SCL stopband (see Section 1.4). Another important design goal is iv) the uniformity of the longitudinal electric field intensity along the linac tank cavities. As a consequence, an optimal design of SCL tanks requires many parametric simulations or, as an alternative, a global optimum search approach. Global search techniques, such as the artificial neural networks, the genetic algorithms, and the PSO, have been successfully exploited in em and optical optimization problems [37], [69]–[72].

Some commercial codes provide internal optimization tools to minimize/maximize particular figures of merit via global methods. Despite this, the objectives i)–iv) cannot be simultaneously taken into account and optimized by using the internal routines of the commercial codes. In such cases, a number of simulations are needed via trial and error approach. It is worth pointing out that the approach described in the following sections allows an extremely efficient and fully automated design procedure. It has been observed that, with commercial codes, the complex design procedure causes downtime between consecutive simulations due to the need for defining the new optimization trials.

In the following sections, a novel hybrid approach (HA), implemented via a homemade computer code, for the global search design and optimization of SCL tanks is described. The HA code integrates a full 3D FEM numerical investigation with an analytical model which accurately takes into account the periodic structure of the SCL tanks. A multi-objective PSO technique [73] is also exploited to find the optimal geometry of the SCL cavities with respect to the design specifications. The HA code has been used for designing a 27-MeV 3-GHz standing-wave SCL tank of 35 cavities for hadrontherapy applications [15]. To investigate the feasibility of the hybrid approach, a shorter SCL tank consisting of five cavities closed with suitable ECs has been fabricated and characterized. The spatial period of the manufactured tank is the same as that considered for the tank of 35 cavities. Furthermore, the characterization of the five-cavities SCL tank allowed validating the proposed HA. An excellent agreement between simulation and experiment has been found. The HA code is general and it can be effectively used for designing a wide class of resonant structures.

2.2 DESIGN OVERVIEW

The hybrid analytical/numerical approach used to design the SCL cavities is based on the analytic theory described in Section 1.7. For each tentative set of geometrical parameters (tentative solution), the HA code follows these main steps:

1. an SCL quintuplet with half CCs termination is considered;
2. the 3D numerical investigation, performed via a FEM commercial software driven by the HA code, is used to find the eigenmodes of the SCL quintuplet;
3. with the simulated eigenfrequencies, the polynomial equation system in (1.26) is solved to find the coupling constants and the loaded frequencies of the tentative ACs and CCs;
4. a constrained multi-objective function is then evaluated with respect to the design objectives. To this aim, a multi-objective PSO routine is exploited [73].

A more detailed explanation and the flowchart of the HA code are provided in the Section 2.2.1. It is worth noting that the hybrid approach, as described above, can be easily adapted to any design of coupled-cavity resonant structures.

The HA code allows the full automation of the em design of an SCL tank. As a consequence, compared to non-automated conventional design procedures, a significantly (up to about two/three times) lower time is needed to design the complex microwave SCL cavities. In fact, the downtime due to the decision making needed to define the new optimization simulations is avoided. Moreover, it has been observed it is not possible to implement the foregoing automated design procedure by exploiting the internal tools of the commercial codes.

A sketch of the resonant SCL cavities being optimized is shown in Figure 2.1. A number of fillets and protrusions (nose cones) are included to improve the transit-time factor, increase the quality factor, and modulate the resonant frequency. The cavity geometries shown in Figure 2.1 are largely employed in actual linac plants [15], [22], [74]. The description of the geometrical

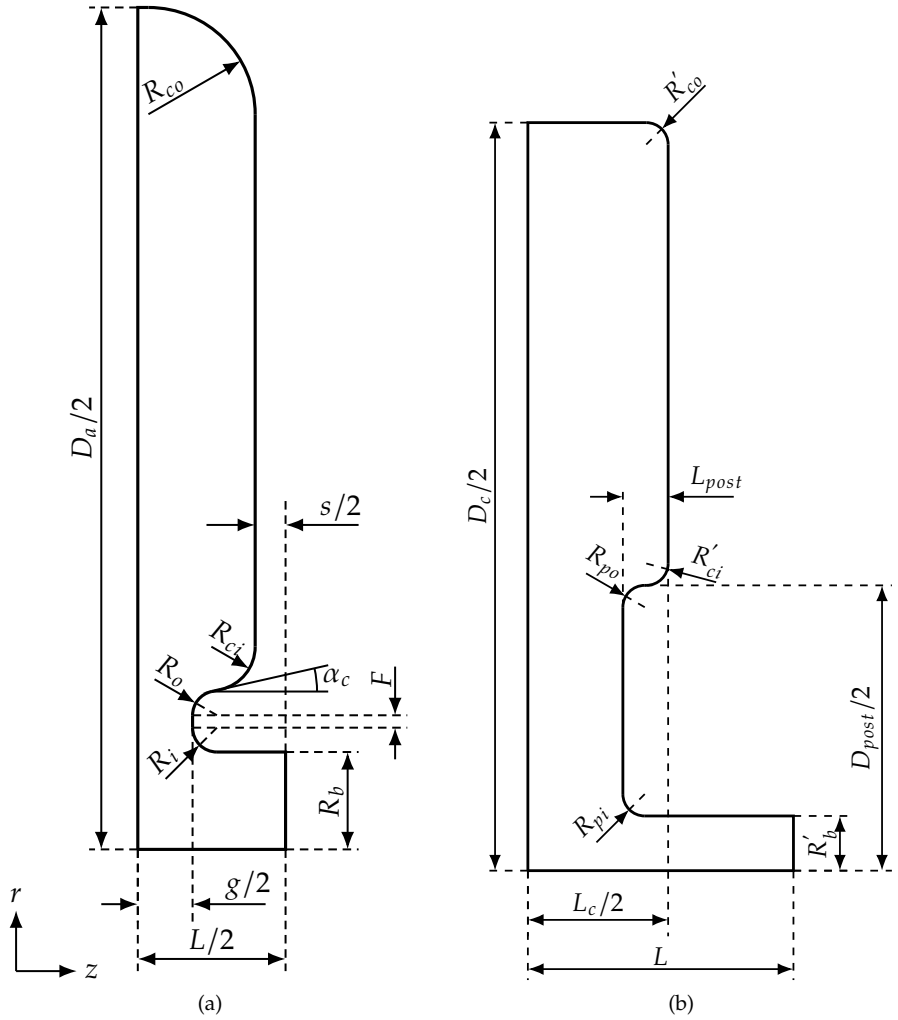

Figure 2.1: Sketches of the (a) AC and (b) CC geometries. A description of the parameters is given in Tables 2.2 and 2.3. Both the cavities are axisymmetric around the z-axis. The radial axis behaves as an ideal PEC plane (TM_{010}-like mode).

parameters is detailed in Tables 2.2 and 2.3. To reduce the computational effort of simulations, the electromagnetic simmetry of the TM_{010}-like modes propagating in the ACs and CCs is exploited. In particular, a perfect electric conductor (PEC) plane along the radial direction is considered, and the rotational symmetry around the z-axis allows for 2D simulations of the single cavities. For 3D simulations of quintuplets, PEC boundary conditions are imposed on the xy-plane, while perfect magnetic conductor (PMC) boundary conditions are imposed on the yz-plane (see Figure 2.2).

2.2.1 *HA code details*

The hybrid analytical/numerical approach used to design the SCL cavities is implemented via the HA code, whose flowchart is depicted in Figure 2.3. A multi-objective PSO technique is used to find the optimal geometry of the SCL cavities by exploiting the Pareto optimality condition [75]. To this aim, the

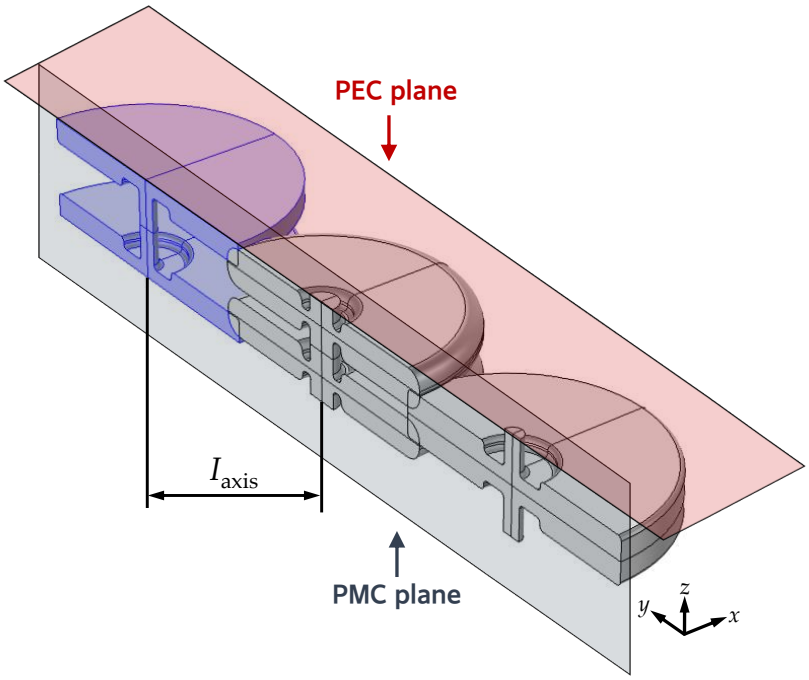

Figure 2.2: 3D view of an SCL tank of five cavities (two ACs and three CC) closed with half CCs (highlighted in blue). The boundary conditions used in simulations are also provided (the bottom PEC plane is not shown).

following components of the multi-objective function $\boldsymbol{O}(\boldsymbol{x}) = [o_1(\boldsymbol{x}), o_2(\boldsymbol{x})]$ are simultaneously minimized:

$$\begin{aligned} o_1(\boldsymbol{x}) &= |f^{ac}_{\pi/2}(\boldsymbol{x}) - f_{\pi/2,\text{ref}}|, \\ o_2(\boldsymbol{x}) &= |f^{cc}_{\pi/2}(\boldsymbol{x}) - f_{\pi/2,\text{ref}}|, \end{aligned} \tag{2.1}$$

where $\boldsymbol{x}$ is the vector of the geometrical parameters to be optimized, listed in Table 2.2; $f_{\pi/2,\text{ref}}$ is the reference value of the $\pi/2$ mode frequency, as given by the design specifications (Section 2.2.2). It is worth noting that the simultaneous minimization of the two objective components, $o_1(\boldsymbol{x})$ and $o_2(\boldsymbol{x})$, allows the two $\pi/2$ mode frequencies, $f^{ac}_{\pi/2}(\boldsymbol{x})$ and $f^{cc}_{\pi/2}(\boldsymbol{x})$, to tend to $f_{\pi/2,\text{ref}}$. As a consequence, the difference between $o_1(\boldsymbol{x})$ and $o_2(\boldsymbol{x})$, i. e., the stopband, tends to zero (see also Section 1.4). Moreover, a suitable constraint $k_{1,\min} \leq k_1 \leq k_{1,\max}$ is imposed on the optimization problem to increase the frequency separation between the $\pi/2$ mode and the adjacent modes (see also Section 1.5). Finally, in the last part of the design (Section 2.3.1), the uniformity of the accelerating electric field is taken into account. In particular, to ensure that protons gain about the same amount of energy in each accelerating cavity, the relative standard deviation, σ_R, of the longitudinal electric field peaks is kept below a fixed threshold $\sigma_{R,\max}$. The details on all the design criteria are illustrated in Section 2.2.2.

The HA code is organized as follows. After reading the input settings and the design specifications, the positions and velocities of the swarm particles are initialized. The Pareto-optimal solutions, found during the search process, are stored in a repository and updated at each iteration. At the end of the procedure, this repository will contain the solutions representing the best tradeoffs between the design goals. By exploiting the fitness sharing technique and the mutation operator [73], the HA code promotes the exploration of the

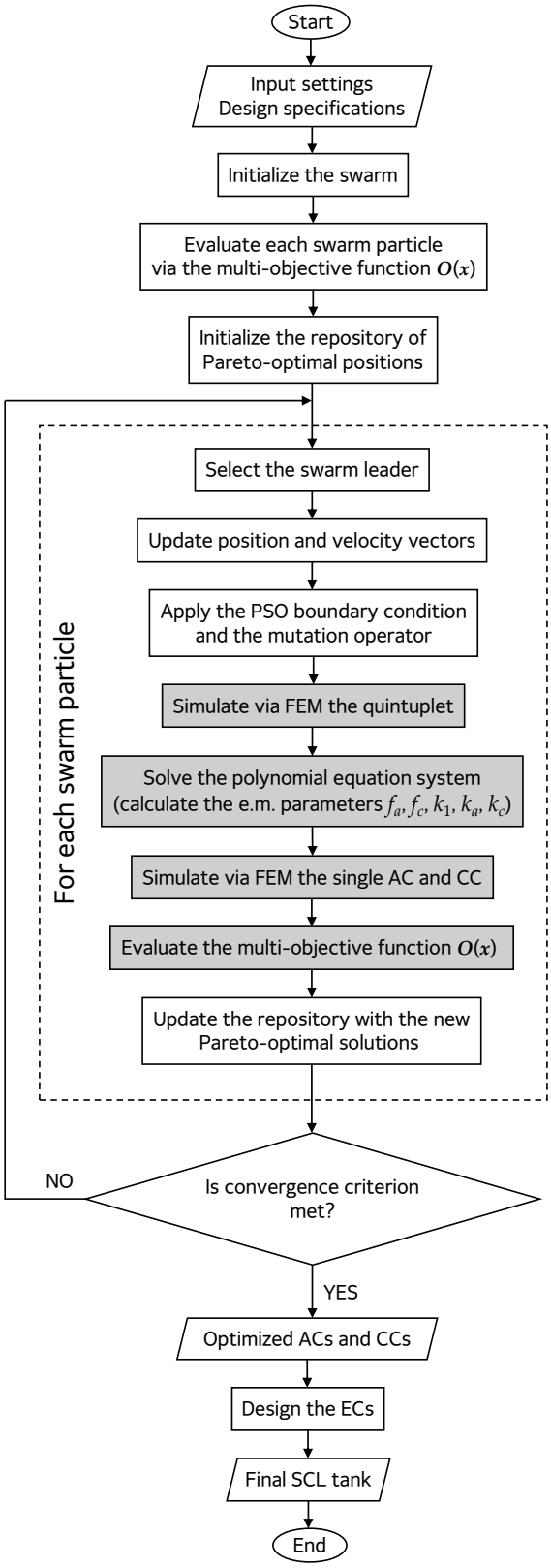

Figure 2.3: Flowchart of the homemade HA code. The operations highlighted in gray are those involved in evaluating the position of a swarm particle.

search space and preserves the population diversity, avoiding the concentration of the tentative solutions in a narrow portion of the objective space. The HA code iterates over the following steps until the convergence criterion is met:

1. select the global best position, i. e., the swarm leader;
2. update the position, $\boldsymbol{x}_i$, and the velocity, $\boldsymbol{v}_i$, of the ith particle moving in the search space, according the following equations:

$$\begin{aligned} \boldsymbol{v}_i(t+1) &= w\boldsymbol{v}_i(t) + c_1 r_1[\boldsymbol{p}_i(t) - \boldsymbol{x}_i(t)] + c_2 r_2[\boldsymbol{g}(t) - \boldsymbol{x}_i(t)], \\ \boldsymbol{x}_i(t+1) &= \boldsymbol{x}_i(t) + \boldsymbol{v}_i(t+1), \end{aligned} \tag{2.2}$$

   where t is the previous iteration; $\boldsymbol{p}_i(t)$ is the best previous position of the ith particle; $\boldsymbol{g}(t)$ is the best previous position in the entire swarm; w is the inertia weight; c_1 and c_2 are two positive constants known as cognitive and social parameter, respectively; r_1 and r_2 are two uniform stochastic weights taken in the range $[0, 1]$ to model the slight unpredictable component of the natural swarm behaviour [73].
3. apply the mutation operator to the particles;
4. by exploiting $\boldsymbol{x}_i$, simulate via FEM the quintuplet with half CCs termination (Section 1.7);
5. analytically calculate the loaded frequencies of ACs and CCs, f_a and f_c, and the coupling constants k_1, k_a, and k_c, by solving the polynomial equation system in (1.26);
6. by exploiting $\boldsymbol{x}_i$, simulate via FEM the single AC and CC to obtain their the unloaded frequencies, i. e., the frequencies with no couplings. Moreover, a number of figures of merit pertaining to the ACs are also calculated, including Q factor, power losses, transit-time factor, (effective) shunt impedance and peak surface electric field (see also Section 1.2);
7. evaluate the multiobjective function $\boldsymbol{O}(\boldsymbol{x}_i)$ according to (2.1);
8. update the repository with the new Pareto-optimal solutions.

The code stops when the convergence criterion is met; then, it returns the optimized tank geometry.

2.2.2 *Design specifications*

The electromagnetic design of an SCL tank consisting of 35 cavities (18 ACs and 17 CCs) is performed via the HA computer code. The accelerating tank period, L, is calculated by taking into account the design parameters listed in Table 2.1 [15], [22], [74]. The calculated accelerating period is $L = 12.140\,\text{mm}$ and it is listed in Table 2.3. Moreover, the values $k_{1,\min} = 3\,\%$ and $k_{1,\max} = 4\,\%$ are considered for the constraint imposed on $\boldsymbol{O}(\boldsymbol{x})$, according to [15], [22], [74]. Finally, in order to have a more uniform energy gain along the beam line, the relative standard deviation of the longitudinal electric field peaks is kept below $\sigma_{R,\max} = 3\,\%$. All the parameters described so far, in addition to the objectives in (2.1), represent the design specifications.

Table 2.1: HA tank period calculation settings.

PARAMETER	DESCRIPTION	VALUE
$f_{\pi/2,\mathrm{ref}}$	Design $\pi/2$ mode frequency (GHz)	2.99792
β	Proton relative velocity	0.24
E_{in}	Proton beam input energy (MeV)	27
E_0	Average electric field on beam line (MV/m)	15
T	Nominal transit-time factor	0.80
ϕ_s	Synchronous phase (°)	-20
n_{ACs}	Total number of ACs in tank	18

2.3 SIMULATION RESULTS

Table 2.2 lists the global optimized geometrical parameters of the SCL accelerating and coupling cavities along with their search ranges. The search ranges are wide enough to provide a large set of feasible solutions, i. e., to provide swarm with very good exploratory capabilities. Table 2.3 lists the geometrical parameters kept constant during the optimization process. They are consistent with the literature [15], [22], [74]. In particular, the beam hole radius, R_b, is set to a value providing high transmittance of the particle beam. The settings of the multi-objective PSO routine are listed in Table 2.4. The values of w, c_1, c_2, N_{grid}, and M are the same suggested in [73]. The values of N_{pop}, N_{iter}, and N_{rep} are chosen in order to reduce the computational cost of the approach, while keeping a good population diversity and ensuring accurate results. Moreover, the invisible boundary condition is imposed on the search space [70]. However, the computation time needed to obtain the optimized geometrical parameters listed in Table 2.2 mainly depends on the mesh settings defined for 3D simulations. By using a smallest mesh size of 1 mm and the settings listed in Table 2.4, the SCL tank design has required about a week on a PC with an Intel Core i7-4770 and 16 GB of RAM. Further reducing the computational effort is not trivial. A possible solution is to avoid 3D simulations by estimating the coupling constants through known analytical formulas [46]–[48]. Other solutions are:

- using coarser meshes;
- using smaller search ranges and lowering the number of swarm particles;
- lowering the number of iterations;
- simulating a triplet, rather than a quintuplet, at each iteration, by neglecting k_a and k_c (especially at higher energies);
- optimizing the code to exploit the modern multicore/multiprocessor computer architectures.

All these solutions, except for the last one, can affect the simulation accuracy, and a tradeoff is required.

Figure 2.4 shows the convergence of the particle swarm in the objective space at the 50th and 100th iterations. The red dots represent the Pareto-optimal solutions collected in the repository up to the considered iteration, while the blue dots represent the actual population. The coordinate axes are given by (2.1). The solutions tend to reside near the origin of the objective

Table 2.2: Optimized geometrical parameters of the SCL ACs and CCs.

PARAMETER	DESCRIPTION	SEARCH SPACE (mm)†	OPTIMIZED VALUE (mm)†
D_a	ACs: diameter	$[50.0, 75.0]$	67.125
g	ACs: gap length	$[1.0, 5.0]$	3.059
R_{co}	ACs: outer corner radius	$[3.4, 10.0]$	3.875
F	ACs: flat length	$[0.0, 2.0]$	0.718
α_c	ACs: cone angle	$[0.0, 20.0]°$	6.686°
s	ACs: septum thickness	$[1.2, 4.0]$	2.890
L_c	CCs: length	$[5.0, 15.0]$	11.550
D_c	CCs: diameter	$[50.0, 75.0]$	68.469
L_{post}	CCs: post length	$[2.0, 6.0]$	2.559
D_{post}	CCs: post diameter	$[10.0, 50.0]$	18.061
I_{axis}	Interaxis (see Figure 2.2)	$[62.0, 72.0]$	63.848

† Except for α_c.

Table 2.3: Constant geometrical parameters of the SCL ACs and CCs.

PARAMETER	DESCRIPTION	VALUE (mm)
L	Tank period	12.140
R_{ci}	ACs: inner corner radius	1.8
R_i	ACs: inner nose radius	1.0
R_o	ACs: outer nose radius	1.0
R_b	ACs: beam hole radius	4.0
R'_{co}	CCs: outer corner radius	1.0
R'_{ci}	CCs: inner corner radius	1.0
R_{pi}	CCs: inner post radius	1.0
R_{po}	CCs: outer post radius	1.0
R'_b	CCs: bore radius	2.5

Table 2.4: HA optimization settings.

PARAMETER	DESCRIPTION	VALUE
N_{pop}	Number of swarm particles	50
N_{iter}	Total number of iterations	100
w	Inertia weight	0.4
c_1	Cognitive constant	1
c_2	Social constant	1
N_{grid}	Adaptive grid divisions (in all dimensions)	30
N_{rep}	Swarm particles repository size	50
M	Mutation rate	0.5

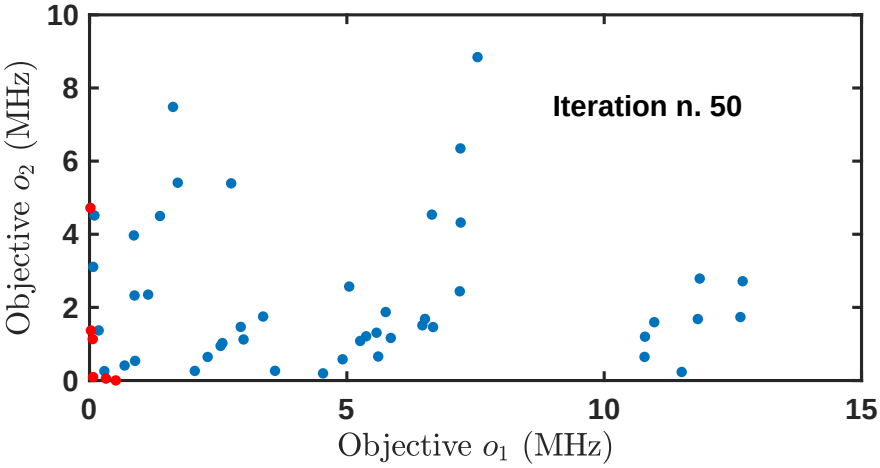

(a)

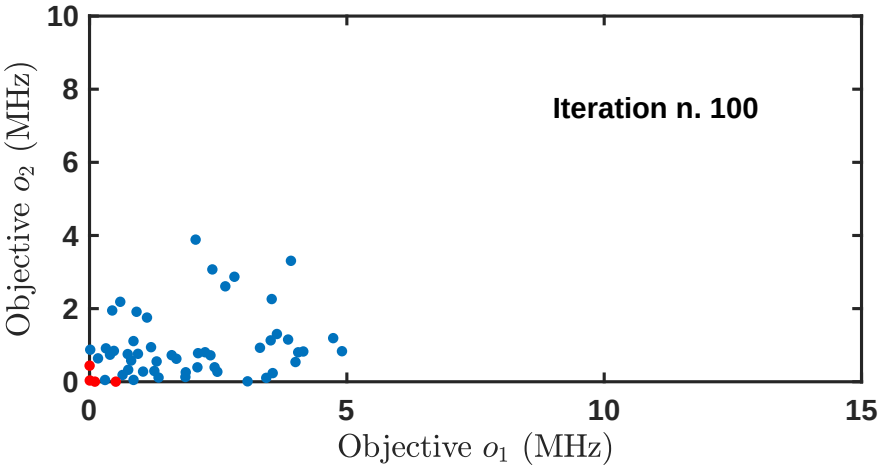

(b)

Figure 2.4: Convergence of the swarm particles in the objective space at different iteration numbers: (a) 50 and (b) 100. The objective components, o_1 and o_2, are given in (2.1). The red dots are the Pareto-optimal solutions collected in the repository; the blue dots represent the actual population.

Table 2.5: Frequencies and coupling constants of the optimized SCL cavities.

PARAMETER	DESCRIPTION	VALUE
f_a	Frequency of ACs (GHz)	3.007145
f_c	Frequency of CCs (GHz)	2.997866
k_1	Coupling constant between ACs and CCs	3.23×10^{-2}
k_a	Coupling constant between adjacent ACs	-6.03×10^{-3}
k_c	Coupling constant between adjacent CCs	1.80×10^{-4}

space. Since the coordinate axes are exactly o_1 and o_2, this means that the solutions are those for which $f^{AC}_{\pi/2} \cong f_{\pi/2,\mathrm{ref}}$ and $f^{CC}_{\pi/2} \cong f_{\pi/2,\mathrm{ref}}$, so the stopband approximately equals zero. Then, the best global solution selected from the repository is the particle with the smallest stopband (less than 1 MHz).

Table 2.5 lists the frequencies and coupling constants of the optimized cavities. The corresponding stopband is very small, being about 12.5 kHz. The simulated values of the ACs' unloaded Q factor, $Q_{0,\mathrm{AC}}$, and unloaded effective shunt impedance per unit length, $ZT^2_{0,\mathrm{AC}}$, are $Q_{0,\mathrm{AC}} = 6180$ and $ZT^2_{0,\mathrm{AC}} = 31\,\mathrm{MV/m}$, respectively.

2.3.1 *End Cells*

The results illustrated so far are used for the design of the ECs, since in actual linac plants the tanks are closed with full ACs (see also Section 1.8).

To validate the HA computer code, a shorter tank of five optimized cavities has been considered for fabrication and characterization (Section 2.4). In view of this, the SCL quintuplet closed with ECs shown in Figure 2.5a has been first simulated. It consists of two ECs, one central AC and two side CCs. In the design, starting from the optimized ACs (Table 2.2), the two ECs are then finely tuned so that: 1) the relative standard deviation of the peak values of the on-axis longitudinal electric field intensity, $|E_z|$, is less than $\sigma_{R,\max} = 3\,\%$ and 2) the frequency of the $\pi/2$ mode is equal $f_{\pi/2,\mathrm{ref}}$. To this aim, the gap, g, and the nose flat length, F, of just the outer halves of the ECs are varied (see Figure 2.5a). Following this tuning step, the small value $\sigma_{R,\mathrm{sim}} = 1.806\,\%$ is obtained and the frequency of the $\pi/2$ mode is $f_{\pi/2,\mathrm{sim}} = 2.997\,916\,\mathrm{GHz}$, practically coincident with $f_{\pi/2,\mathrm{ref}}$.

In Figure 2.5b, the electric field distribution of the resonating $\pi/2$ mode is depicted. As expected, the field is mainly confined in the ACs, near the beam axis, and it is negligible in the CCs.

2.4 MEASUREMENTS

The five-cavity tank closed with the ECs shown in Figure 2.5 has been fabricated and characterized. The high purity oxygen-free electronic grade copper is used to fabricate the cavities. The plates used to assemble the cavities are held together by means of clamps. No brazing process is adopted, and the quality factor is not measured. The five eigenfrequencies, f_q, $q = 0, \ldots, 4$, of the fabricated tank are measured by means of a vector network analyzer (VNA Anritsu MS4644B): $f_0 = 2.959\,719\,\mathrm{GHz}$, $f_1 = 2.972\,545\,\mathrm{GHz}$, $f_2 = f_{\pi/2,\mathrm{meas}} = 2.997\,796\,\mathrm{GHz}$, $f_3 = 3.025\,050\,\mathrm{GHz}$, and $f_4 = 3.049\,900\,\mathrm{GHz}$. The longitudinal electric field amplitude is measured by means of the same

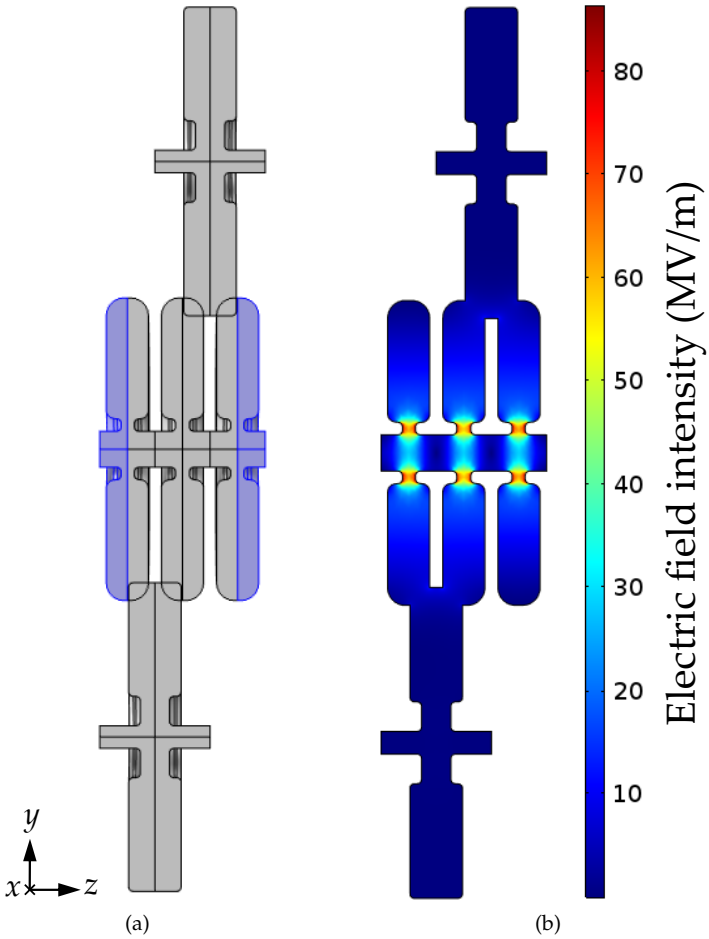

Figure 2.5: Fabricated five-cavity SCL tank with EC terminations. (a) Geometry optimized with the HA computer code; the outer halves of the two ECs are highlighted in blue. (b) Simulated electric field norm of the $\pi/2$ mode.

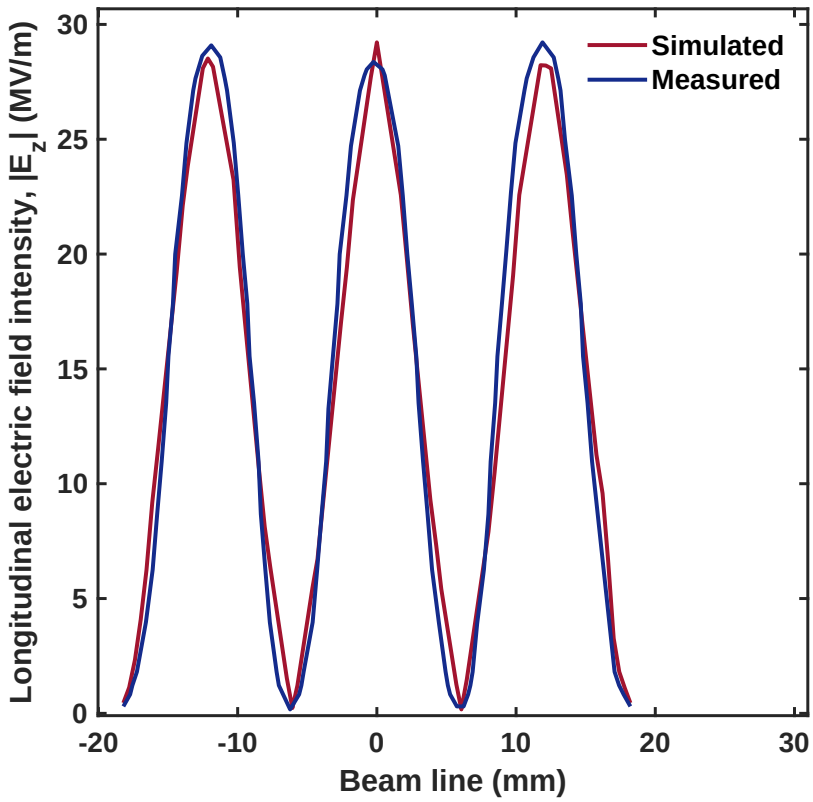

Figure 2.6: Comparison between the simulated and measured longitudinal electric field intensity, $|E_z|$, on the beam line.

VNA. According to the standard bead-perturbation measurement technique [76], a small cylindrical bead is moved through the cavities by a thin nylon line attached to a stepper motor. The motor, in turn, is connected to a digital-analog converter for PC control. The RF excitation is provided to the cavities by two magnetic probes (loop antennas), located into the first and last ACs. The S_{12} scattering parameter is measured through the VNA. In particular, a reference attenuation level of -45 dB is chosen. The estimated frequency shift due to the field probes is negligible (about 100 kHz). The driving frequency of the VNA is locked to the resonant frequency of the $\pi/2$ mode. The measured frequency is $f_{\pi/2,\mathrm{meas}} = 2.997\,796$ GHz, in excellent agreement with the simulated one.

According to the Slater theorem [17], the bead-induced cavity frequency shift is proportional to the square of the local field. In this way, the electric field amplitude is measured in each accelerating gap. The beam pipe-like structure in the CCs is used for the bead-perturbation measurement of the electric field in the CCs. As expected from the simulation (see Figure 2.5b), negligible values of the electric field in the CCs have been measured. The beam pipe-like structure in the CCs can be removed from the final design.

The manufactured cavities are tuned via metallic rods to maximize the field uniformity. The rods are located at the center of the cylindrical wall of each cavity. The rods slightly affect the resonant frequency of the $\pi/2$ mode by inducing a shift of about ± 150 kHz. This shift can be compensated through an operating temperature variation of about $\pm 3\,^{\circ}$C. In Figure 2.6, the simulated and measured longitudinal electric field intensity, $|E_z|$, are shown for comparison. The two curves are normalized to have the mean accelerating field $E_0 = 15$ MV/m along the beam line, which is equivalent to

a simulated peak input power of about $P_{\text{in}} = 200\,\text{kW}$. Figure 2.6 shows an excellent agreement; the difference between the peak values of the simulated and measured longitudinal electric field is close to 0.2 %. In fact, the measured field nonuniformity is $\sigma_{R,\text{meas}} = 1.585\,\%$, practically coincident with the simulated one. The differences between the simulated and measured values of $|E_z|$ may be due to the fabrication tolerances and/or to the small differences between the E_z measurement points and the simulation nodes.

It is worth pointing out that the foregoing approach can be efficiently applied to the design of longer tanks, typically employed in actual linac plants, allowing larger reduction of computation cost and strongly helping the design work. Moreover, the foregoing approach is very versatile and can be used for the design of other complex resonating structures.

2.5 CONCLUDING REMARKS

A powerful homemade computer code, based on a hybrid analytical/numerical approach (HA), has been developed in order to design the complex resonant cavities of an SCL. The HA code integrates a 3D FEM modeling with a multi-objective PSO technique and an analytical model taking into account the periodic structure of the SCL. This hybrid strategy allows performing a fully automated design of the SCL. The design has been validated via measurements on a five-cavities SCL tank prototype. The simulated and measured frequency of the $\pi/2$ mode resonating in the tank are $f_{\pi/2,\text{sim}} = 2.997\,916\,\text{GHz}$ and $f_{\pi/2,\text{meas}} = 2.997\,796\,\text{GHz}$, respectively. Moreover, the measured field nonuniformity is $\sigma_{R,\text{meas}} = 1.585\,\%$, only 0.2 % smaller than the simulated one. The hybrid approach is very promising and general; it can be used for the simultaneous optimization of a larger number of figures of merit concerning the linac cavities, such as the quality factor, the shunt impedance, and the ratio E_s/E_0. Moreover, the hybrid approach can be applied to the design of a wide class of resonating multicavity structures for different applications.

3

DESIGN OF ELECTROMAGNETIC BAND-GAP CAVITIES FOR HIGH-GRADIENT ON-AXIS COUPLED-CAVITY LINEAR ACCELERATORS

In this chapter, the design and optimization of a novel accelerating structure for proton linacs based on suitable electromagnetic band-gap (EBG) coupled cavities are illustrated. In particular, a 27-MeV 3-GHz proton linac tank with on-axis coupled EBG cavities closed with full ECs has been optimized by means of the same hybrid numerical/analytical approach described in Chapter 2. The performances of the EBG accelerating cavities has been compared with the performances of the 27-MeV 3-GHz SCL accelerating cavities in terms of the typical linac figures of merit. By using the EBG cavities, an about 8 % higher transit-time factor has been obtained. Moreover, the peak surface electric field has been strongly reduced, by about 65 %. In view of this, EBG cavities are very promising for the design of very high accelerating gradient microwave proton linacs. Furthermore, the wakefields of the EBG structure have been compared to the wakefields of the SCL structure, showing that the EBG structure provides an effective damping of the transverse wakefields.

3.1 INTRODUCTION

EBG structures consist of periodic arrays (lattices) of metallic and/or dielectric elements which prevent the electromagnetic propagation in a particular frequency band, known as band-gap. The EBG structures can be engineered to design devices with unique properties, not achievable by using conventional geometries. EBG structures are typically used as frequency-selective resonating devices in a wide range of both low power and high power microwave applications, including electromagnetic noise suppression, millimeter-range waveguides, bandpass filters, antennas, liquid sensor, and particle linear accelerators [77]–[94].

Regarding linac applications, EBG cavities were used to design and fabricate metallic [87]–[90] and hybrid (dielectric-metallic) [91]–[94] travelling-wave disk-loaded linear accelerators. EBG linac cavities support single mode propagation allowing the fundamental TM_{010}-like accelerating mode to be confined in the lattice defect, while the high-order modes (HOMs) are unconfined. This allows to suppress the HOM wakefields, enhancing the particle beam stability [95], [96]. Moreover, high accelerating gradient can be achieved in EBG-based linacs. For instance, an accelerating gradient of 35 MV/m was measured in a 17-GHz six-cell EBG electron linac [88] and an accelerating gradient of 89 MV/m with low breakdown probability was measured in a similar EBG accelerating structure [90]. Nevertheless, no feasibility investigations have yet been done on the design of EBG-based standing-wave linacs for accelerating heavy ion beams, such as proton beams.

In the following sections, the design and optimization of a novel on-axis coupled EBG proton linac is reported. In particular, the design of a 3-GHz standing-wave EBG linac tank closed with full end cells has been performed via the same hybrid numerical/analytical approach (HA code) described in the previous chapter. A proton beam with an input energy of 27 MeV has been considered. The typical linac figures of merit pertaining to the EBG

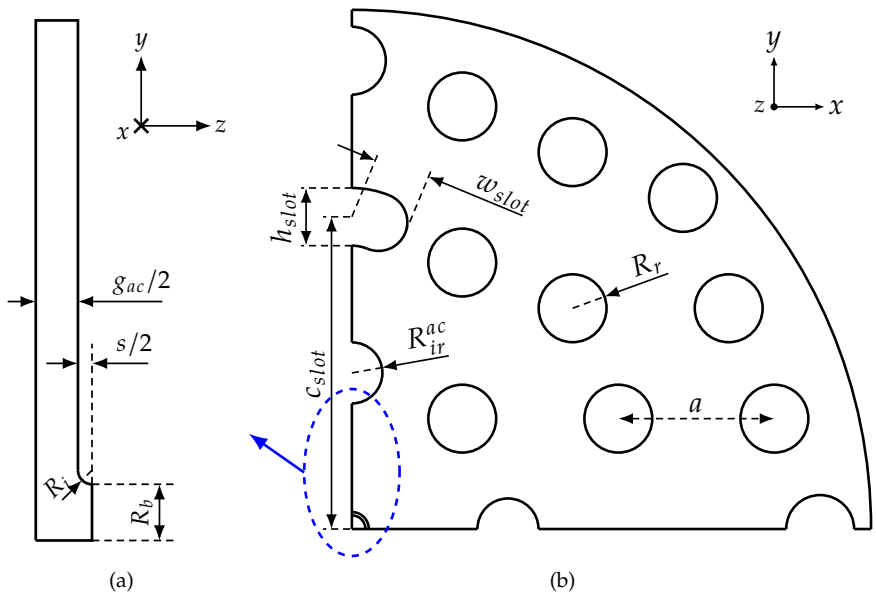

Figure 3.1: Sketches of the (a) transversal and (b) longitudinal cross-sections of an EBG accelerating cavity. The geometrical parameters are listed in Tables 3.1 and 3.2. The rods overlapping with the coupling slot area are removed from the cavity.

accelerating cavities have been compared with those pertaining to the SCL accelerating cavities optimized in Chapter 2. Interesting results have been obtained, which allow to predict the feasibility of high accelerating gradient EBG-based proton linacs with low RF breakdown probability and effective wakefields damping.

3.2 DESIGN OVERVIEW

A sketch of the EBG accelerating cavities considered in the HA code is shown in Figure 3.1. By substituting g_{ac} and R_{ir}^{ac} with g_{cc} and R_{ir}^{cc}, respectively, the EBG coupling cavities are obtained. Both the EBG accelerating and coupling cavities consist of an octagonal lattice of cylindrical copper rods, because of the 8-fold rotational symmetry of the octagonal lattice, which allows for 2-fold rotational symmetry when considering also the coupling slots. Removing one rod in the center of the 2D metal lattice allows the confinement of the accelerating mode. The oxygen-free electronic grade copper is considered as the material for rods and plates.

To reduce the computational effort of simulations, the electromagnetic symmetry of the TM_{010}-like modes propagating in the ACs and CC is exploited. In particular, the following boundary conditions are imposed in order to simulate one eighth of the total cavity volumes: 1) the $x = 0$ and $y = 0$ planes are considered as PMC planes, 2) the $z = 0$ plane is considered as a PEC plane. Moreover, 3) the perfect matched layers (PMLs) are used around the inner volumes of ACs and CCs, to absorb any em energy leaks from the open sides of ACs and CCs. Three octagonal rings of rods are used in the design of ACs and CCs, since the em power losses increase as the number of rings increases.

Due to the open sides of the EBG cavities, the on-axis coupling between ACs and CCs are considered instead of the side-coupling (see also Section 1.6). Two slots for magnetic coupling between ACs and CCs are placed on

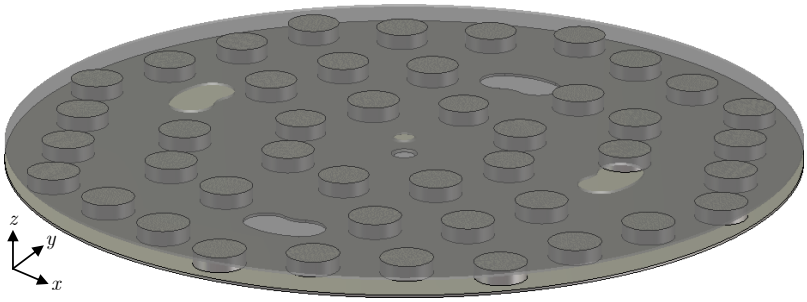

Figure 3.2: 3D sketch of a full EBG accelerating cavity. The outer (copper) volume is shown. The end wall with the 90°-rotated magnetic coupling slots is shown in transparency.

each cavity end wall. As an example, in Figure 3.2 the 3D view of an EBG accelerating cavity is shown. To avoid direct magnetic coupling between cavities of the same type, the coupling slots on one end wall are rotated by 90° from the coupling slots on the opposite end walls [17]. The copper rods overlapping with the coupling slots are removed from each cavity (see the dotted-line rods in Figure 3.1b). Since the em field of the accelerating mode is confined in the center volume of the EBG cavities, the radius of the rods on the innermost ring strongly influences the resonance frequency of the cavities. The innermost rods placed below the coupling slots have a different radius ($R_{ir}^{ac,cc}$, in Figure 3.1b) from that of the other rods (R_r, in Figure 3.1b). This also allows to achieve a finer tuning of the frequency of ACs and CCs, which is required for reducing the stopband.

3.2.1 *HA code details*

The HA code used to design the linac EBG cavities is effectively the same one described in Chapter 2 (see Figure 2.3) and successfully validated by measurements. Only the following minor changes have been taken into account due to the on-axis coupled-cavity configuration:

- the half ACs termination is considered instead of the half CCs termination (see also Section 1.7);
- the following multi-objective function $\boldsymbol{O}(\boldsymbol{x}) = [o_1(\boldsymbol{x}), o_2(\boldsymbol{x}), o_3(\boldsymbol{x})]$ is minimized:

$$\begin{aligned} o_1(\boldsymbol{x}) &= |f_{\pi/2}^{ac}(\boldsymbol{x}) - f_{\pi/2,\mathrm{ref}}|, \\ o_2(\boldsymbol{x}) &= |f_{\pi/2}^{cc}(\boldsymbol{x}) - f_{\pi/2,\mathrm{ref}}|, \\ o_3(\boldsymbol{x}) &= 1/ZT_{0,ac}^2(\boldsymbol{x}), \end{aligned} \tag{3.1}$$

  where the first two objective components, $o_1(\boldsymbol{x})$ and $o_2(\boldsymbol{x})$, are the same ones illustrated in the previous chapter. Through the third objective component, $o_3(\boldsymbol{x})$, the unloaded effective shunt impedance per unit length of the ACs, $ZT_{0,ac}^2$, is maximized. That is the energy gain in a given accelerating gap for a given power loss is maximized (see also Section 1.2). Compared to the multi-objective function in (2.1) used to optimize the SCL cavities, the third objective, $o_3(\boldsymbol{x})$, in (3.1) has been added in order to compensate for the lower effective shunt impedance which typically affect the on-axis coupled-cavity linac structures [17].

Furthermore, to reduce the computational cost of the numerical simulations and increase the efficiency of the design approach, a first optimization step

Table 3.1: Optimized geometrical parameters of the EBG ACs and CCs.

PARAMETER	DESCRIPTION	SEARCH SPACE (mm)	OPTIMIZED VALUE (mm)
a	Lattice constant	[40.0, 50.0]	45.515
R_r	Radius of rods	[2.0, 20.0]	9.889
g_{ac}	ACs: gap length	[1.0, 6.0]	5.807
R_{ir}^{ac}	ACs: inner rods' radius	[2.0, 20.0]	9.483
R_{ir}^{cc}	CCs: inner rods' radius	[2.0, 20.0]	9.188
w_{slot}	Half-width of coupling slots	[12.0, 35.0]	17.219
h_{slot}	Height of coupling slots	[2.0, 35.0]	17.444

is carried out by considering in the analytical model a three-cavities tank, or triplet, closed with half ACs. In this case, only the nearest neighbor coupling is taken into account (Section 1.3). That is, the polynomial equation system in (1.26) reduces to three equations with the unknowns $[f_a, f_c, k_1]^\intercal$ and $k_a = 0$, $k_c = 0$. Then, a second optimization step is carried out by considering quintuplets, i. e. the complete system in (1.26) is taken into account. The second optimization step is a refinement of the first optimization step, so a very small number of iterations are needed in the second optimization step. By using this double-step approach, the design of the linac cavities needs less than half the time that would be required if only quintuplets were simulated at each HA code iteration, for equal mesh size and HA code settings. By using triplet simulations, the approximations $k_a = 0$ and $k_c = 0$ must be considered. However, if the coupling constants k_a and k_c are small, the accuracy of the optimization results is slightly affected by the above approximation (just a little tuning of the loaded cavity frequencies is needed in the second optimization step).

3.2.2 *Design specifications*

In order to do a realistic comparison between the SCL and EBG accelerating cavities, the same design parameters listed in Table 2.1 and the calculated accelerating tank period $L = 12.140$ mm are considered for designing and optimizing the EBG proton linac tank too. The upper limit $\sigma_{R,\max} = 3\,\%$ for the relative standard deviation of the longitudinal electric field peaks is again considered. Finally, the design objectives in (3.1) contribute to determining the design specifications.

3.3 SIMULATION RESULTS

Table 3.1 lists the optimized geometrical parameters of the EBG accelerating and coupling cavities along with their search ranges. It is worth noting that the search ranges listed in Table 3.1 are wide enough to provide a large set of feasible solutions, i. e. to provide swarm with very good exploratory capabilities and population diversity. In particular, in Table 3.1:

- an initial guess of the lattice constant, a, is calculated by considering the central volume of the EBG cavities as it was a conventional TM_{010}

Table 3.2: Constant geometrical parameters of the EBG ACs and CCs.

PARAMETER	DESCRIPTION	VALUE (mm)
L	Accelerating tank period	12.14
R_b	Beam hole radius	4.00
R_i	Beam hole corner radius	1.00
s	Septum (wall) thickness	2.00
g_{cc}	CCs: gap length	$L - g_{ac} - 2s$
c_{slot}	Center of coupling slots	$2a$

cylindrical resonator. Then, a search range for the lattice constant is imposed around the initial guess;

- in the second optimization step based on quintuplet simulations (Section 3.2.1), only the values of R_{ir}^{ac} and R_{ir}^{cc} are refined in the range [8.5, 9.5] mm, around the values optimized in the first step (9.376 mm and 9.233 mm, respectively), by keeping the other geometrical parameters at the values obtained by the first optimization.

Table 3.2 lists the parameters not involved in the optimization process, i. e. no search ranges are defined for these parameters. In particular:

- the beam hole radius, R_b, is set to the same value used in the previous chapter to design the SCL cavities, since it provides high enough proton beam transmittance [15], [22], [74];
- the beam hole corner is rounded off by the radius R_i to reduce the field lines concentration, thus reducing thermal stresses;
- the gap length of the CCs, g_{cc}, is always calculated such that the center-to-center axial distance between two consecutive ACs is equal to the tank period L (see Figure 1.7b).

The optimization settings listed in Table 2.4 are also used for optimizing the EBG proton linac cavities. Thanks to the double-step method described in Section 3.2.1, fewer iterations are needed for optimizing the EBG cavities, specifically 50 iterations for the first optimization step, and 5 iterations for the second step (i. e., $N_{\text{iter}} = 50 + 5$). By considering also the em symmetries described in Section 3.2 and a maximum mesh size used for 3D FEM simulations equal to $(c/f_{\pi/2,\text{ref}})/10$, where c is the speed of light in vacuum, the EBG tank design has required about two days on a PC with an Intel Core i7-4770 and 16 GB of RAM. Compared to the computation time required by the SCL tank design (Section 2.3), it is worth to note the quite higher efficiency of the HA code version used in this work.

Several attempts were made to check the robustness of the HA code by using large search ranges and different population size and number of iterations, which are the most critical parameters for evolutionary optimization algorithms (due to fitness evaluations and overall computation time). The parameters listed in Table 2.4 (with $N_{\text{iter}} = 50 + 5$) and the search space in Table 3.1 are a good trade-off between computation time and convergence consistency. The uncertainties in the solutions of multiple runs range from 0.1 % to 1 %. Smaller uncertainties can be achieved by increasing N_{pop} and

Table 3.3: Frequencies and coupling constants of the optimized EBG cavities.

PARAMETER	DESCRIPTION	VALUE
f_a	Frequency of ACs (GHz)	2.998141
f_c	Frequency of CCs (GHz)	2.999258
k_1	Coupling constant between ACs and CCs	3.52×10^{-3}
k_a	Coupling constant between adjacent ACs	4.63×10^{-4}
k_c	Coupling constant between adjacent CCs	-8.69×10^{-5}

N_{iter} or by introducing a suitable convergence criterium taking into account at least the uncertainties of the most significant parameters.

Table 3.3 lists the loaded frequencies and coupling constants of the optimized EBG cavities. The stopband is very small, being about 292 kHz.

3.3.1 *End Cells*

The results illustrated in Section 3.3 are then used for the design of the ECs (see also Section 1.8). In particular, starting from the optimized ACs (Table 3.1), the two ECs are then finely tuned so that: i) the relative standard deviation, σ_R, of the peaks of the longitudinal electric field intensity, $|E_z|$, is less than $\sigma_{R,\max} = 3\,\%$; ii) the $\pi/2$ mode frequency is equal (or very close) to $f_{\pi/2,\text{ref}}$. To this aim, the gap length of the ECs, g_{ec}, is slightly lowered with respect to the gap length of the optimized ACs, g_{ac}, i. e. $g_{ec} = 0.91 g_{ac}$. Figure 3.3 shows the electric field distribution of the $\pi/2$ mode in a tank of five optimized EBG cavities closed with the ECs. The on-axis electric field intensity, $|E_z|$, in the same simulated tank is shown in Figure 3.4, where the three peaks correspond to acceleration in the two ECs and in the center AC. In Figure 3.3 and Figure 3.4 the electric field intensity is normalized in order to have the design average value $E_0 = 15\,\text{MV/m}$ along the beam line. After the tuning of the ECs, an accelerating field nonuniformity as small as $\sigma_R = 1.1\,\%$ is obtained and the simulated frequency of the $\pi/2$ mode is $f_{\pi/2,\text{sim}} = 2.998\,09\,\text{GHz}$, very close to $f_{\pi/2,\text{ref}}$ (see Table 2.1).

3.4 PERFORMANCE COMPARISON BETWEEN SCL AND EBG ACS

In Table 3.4 the performances of the optimized EBG accelerating cavities are compared with the performances of the accelerating cavities of the optimized SCL tank illustrated in Chapter 2. As already mentioned, the same design specifications on $f_{\pi/2,\text{ref}}$, E_{in}, E_0 and L listed in Table 2.1 are considered for both the EBG and SCL tanks. The power losses of the EBG cavities are higher than the power losses of the SCL cavities, due to the larger transversal dimension of the EBG cavities and to the on-axis coupling configuration. This in turn results in 30 % lower Q factor and effective shunt impedance. However, the transit-time factor of the EBG cavities is about 8 % higher than the transit-time factor of the SCL cavities, approaching values typically found in higher energy linac cavities [17], [20], [74]. Moreover, the peak surface electric field of the EBG cavities is strongly reduced, by about 65 %. This is due to the absence of nose cones which instead are needed in SCL cavities to increase the transit-time factor. Since EBG and SCL accelerating cavities have the same $\beta\lambda$ and E_0 and the electric field is predominant near the beam line, the higher transit-time

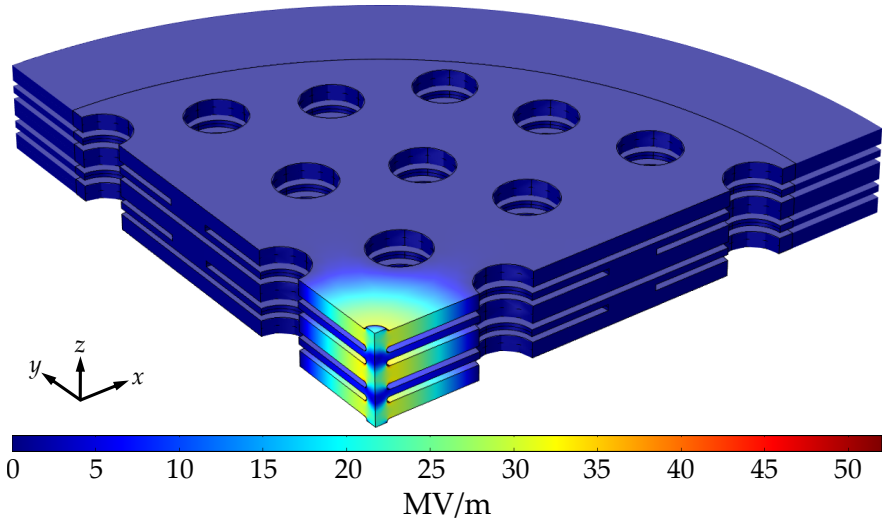

(a)

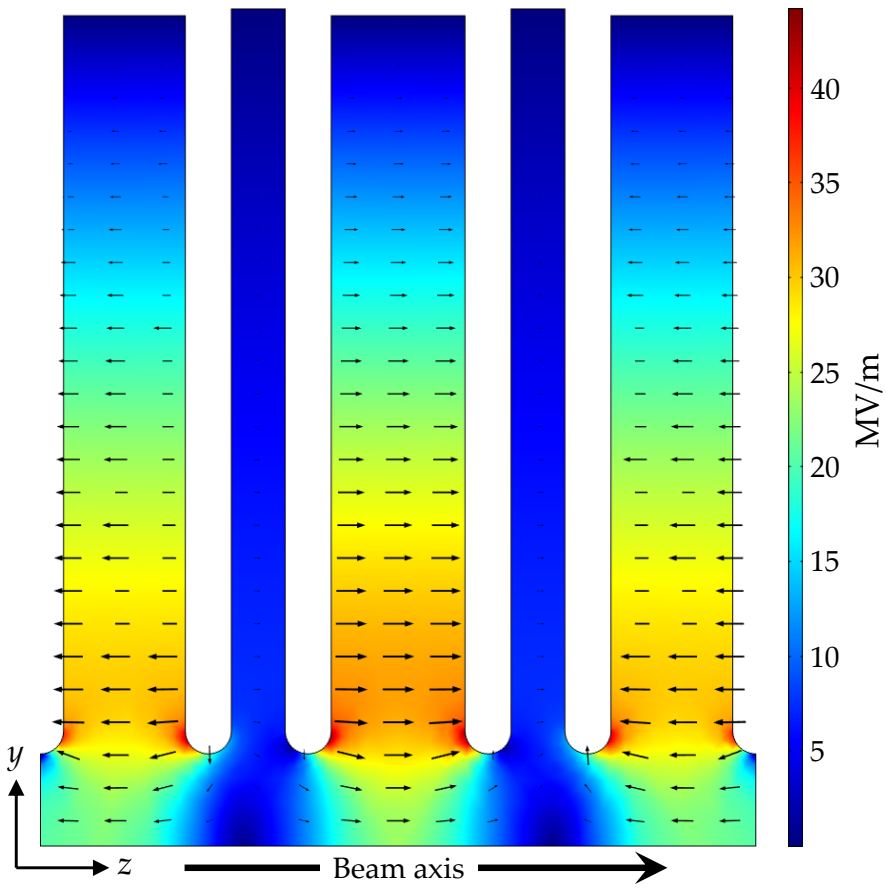

(b)

Figure 3.3: Distribution of the simulated electric field intensity of the $\pi/2$ mode in an EBG proton linac tank of five optimized cavities closed with full ECs. (a) 3D view (the PMLs around the inner volume of the cavities are also shown). (b) yz-plane (the central volume enclosed by the innermost rods is shown).

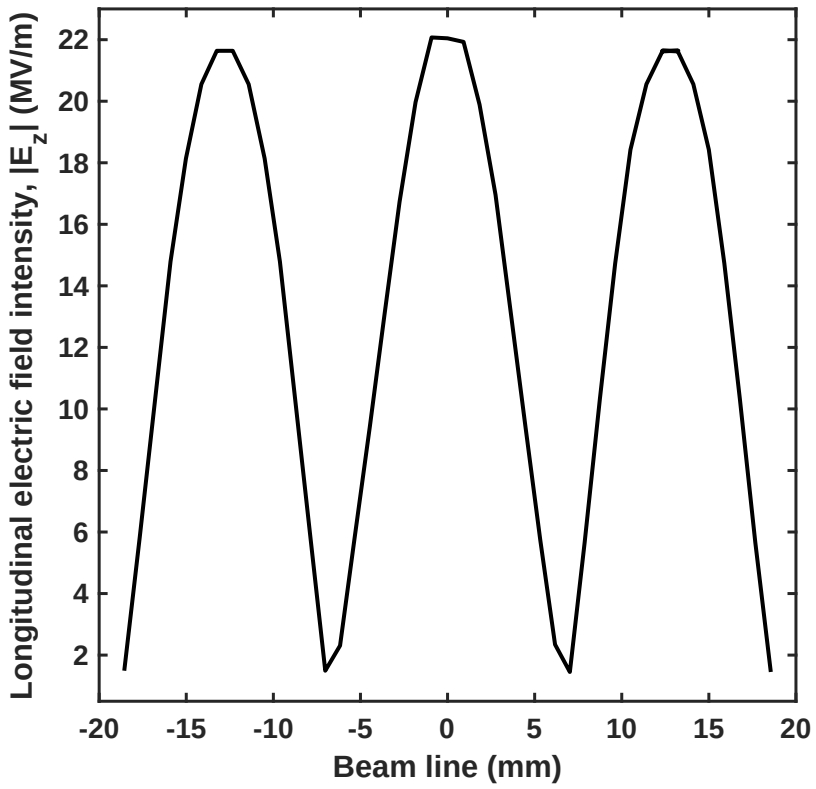

Figure 3.4: Simulated longitudinal electric field intensity, $|E_z|$, on the beam line of the optimized EBG proton linac tank shown in Figure 3.3.

Table 3.4: Performance comparison between the ACs of the SCL tank (Chapter 2) and the ACs of the EBG tank.

PARAMETER	SCL	EBG
Unloaded frequency (GHz)	3.06231	2.99364
Cavity radius (mm)	33.563	151.434
Cavity length (mm)	12.140	7.807
Accelerating gap length (mm)	3.059	5.807
Average axial electric field (MV/m)	15	15
Transit-time factor	0.78	0.84
Unloaded quality factor	6180	4032
Surface losses (kW)	53.3	61.9
Effective shunt impedance per unit length (MΩ/m)	31	20
Peak surface electric field (MV/m)	93.2	32.6
Peak surface current density (kA/m)	37.8	51.1

factor of the EBG accelerating cavities may be related to the lower peak surface electric field, which results in lower thermal losses and better exploitation of the on-axis electric field to provide energy gain to the proton beam.

The peak surface current density is about 35 % higher in the EBG cavities, due to the presence of the innermost rods which prevent the RF surface current from flowing over larger surfaces. The surface current density is higher at the rods boundaries, where the magnetic field is predominant. To mitigate the peak surface current density on the rods boundaries, two feasible solutions are:

- add an objective component in (3.1) to minimize also the peak magnetic flux;
- placing suitable cooling pipes within the innermost rods. It is worth noting that such cooling pipes can also be effective for managing high thermal stress points near the beam hole corner, where the peak surface electric field is predominant.

In Figure 3.5 the dispersion curve of the 35-cavities EBG tank is shown along with the dispersion curve of the 35-cavities SCL tank described in Section 2.3. Because of the lower coupling constant k_1, the frequency spacing between the $\pi/2$ mode and the adjacent modes in the EBG tank is very small, being about 0.5 MHz, while in the SCL tank it is equal to about 4.4 MHz. However, from an RF point of view, by increasing the accelerating gradient in the EBG accelerating cavities by a factor of three, one third of the total number of ACs is enough to achieve the same energy gain. In Figure 3.5 the dispersion curve of a shorter EBG tank with 11 cavities (4 ACs, 2 ECs and 5 CCs) is also shown. In such a case, the frequency spacing between the $\pi/2$ mode and the adjacent modes increases to about 1.5 MHz. By increasing the accelerating gradient, the surface losses increase as well, making it necessary considering higher $\pi/2$ mode frequencies. The maximization of the frequency difference between modes neighboring the $\pi/2$ mode can be included in the multi-objective function $\boldsymbol{O}(\boldsymbol{x})$ in order to further increase the field distribution stability. A different geometry for the coupling slots and the innermost rods can also be investigated to increase the value of k_1.

In order to evaluate the wakefield damping provided by the EBG cavities, the longitudinal and transverse wake potentials and impedances have been numerically simulated with single-bunch excitation. The EBG quintuplet closed with the ECs has been considered and compared with the SCL counterpart described in Section 2.3. A proton bunch with a gaussian line charge distribution, length of 1 mm and relative velocity $\beta = 0.24$ (Table 2.1), has been injected into the beam pipes of the linacs with a 2 mm displacement in the x direction. The longitudinal and transverse wake potentials are depicted in Figures 3.6–3.7 as a function of the wakelength, i. e. the distance behind the bunch. The longitudinal and transverse wake impedances, i. e. the frequency spectra of the wakefields, are also shown. The longitudinal wake potentials are affected only by the modes having longitudinal electric fields in the beam pipe. In particular, the beam loading due to the fundamental TM_{010}-like monopole mode largely contribute to the longitudinal wakes of both tanks. The longitudinal wake potential of the EBG tank decays slowly due to the high Q factor of the TM_{010}-like mode. Conversely, in the SCL tank, the longitudinal wake potential remains at a stable value even 10 m behind the exciting proton bunch (the small divergence in the tail may be due to the finite simulation length). The same also applies to the transverse wake potentials, where the contribution due to the dipole and quadrupole HOMs is larger. The high

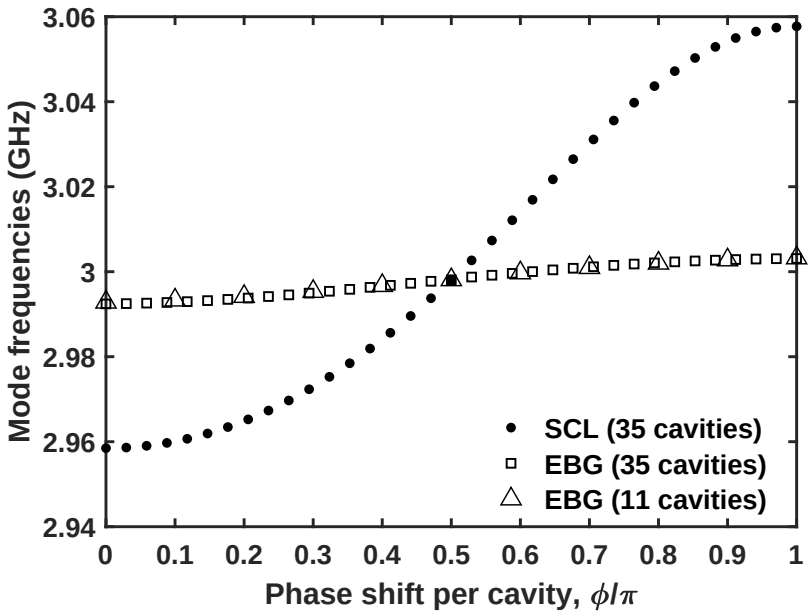

Figure 3.5: Dispersion curves of EBG tanks with 35 and 11 cavities (square and triangle markers, respectively). The dispersion curve of the SCL tank with 35 cavities described in Section 2.3 is also shown.

frequency components in the transverse wake spectra are due to the TM_{230}-like mode, for the EBG tank, and to the TM_{120}-like mode, for the SCL tank.

To evaluate the contribution to the transverse wake potentials from each mode, the transverse wake impedances have been filtered to isolate the peaks pertaining to each mode. Then, by means of an inverse fast Fourier transform, the wake damping due to each HOM has been recovered. Figure 3.8 illustrates the separate contributions of the transverse wake potential as a function of the wakelength. The transverse electromagnetic field distribution of the fundamental mode and HOMs are also shown. As expected, the fundamental TM_{010}-like mode provides a slow-decaying transverse wake potential in the EBG tank, and a constant transverse wake in the SCL tank. The TM_{230}-like quadrupole mode of the EBG tank is excited with less than half of the intensity of the fundamental mode. The faster decay of the TM_{230}-like mode is also due to the larger diffractive losses which lower its Q factor ($Q^{\mathrm{EBG}}_{0,\mathrm{TM}_{230}} = 1254$). Conversely, the higher Q factor of the TM_{120}-like dipole mode of the SCL ($Q^{\mathrm{SCL}}_{0,\mathrm{TM}_{120}} = 6852$) involves negligible damping of such HOM. These results confirm that the EBG cavities provides effective damping of the HOM wakefields relative to the SCL cavities.

Other advantages of EBG cavities with respect to SCL cavities are:

1. a smaller number of geometrical parameters, providing easier design;
2. an easier high frequency scaling of the cavity transverse dimensions, which also allow higher accelerating gradients with negligible RF breakdown probability, according to the Kilpatrick criterion [17].

3.5 CONCLUDING REMARKS

A novel proton linac based on on-axis coupled EBG cavities has been designed and optimized. The experimentally-validated hybrid numerical/analytical approach described in Chapter 2 has been here exploited for the design and

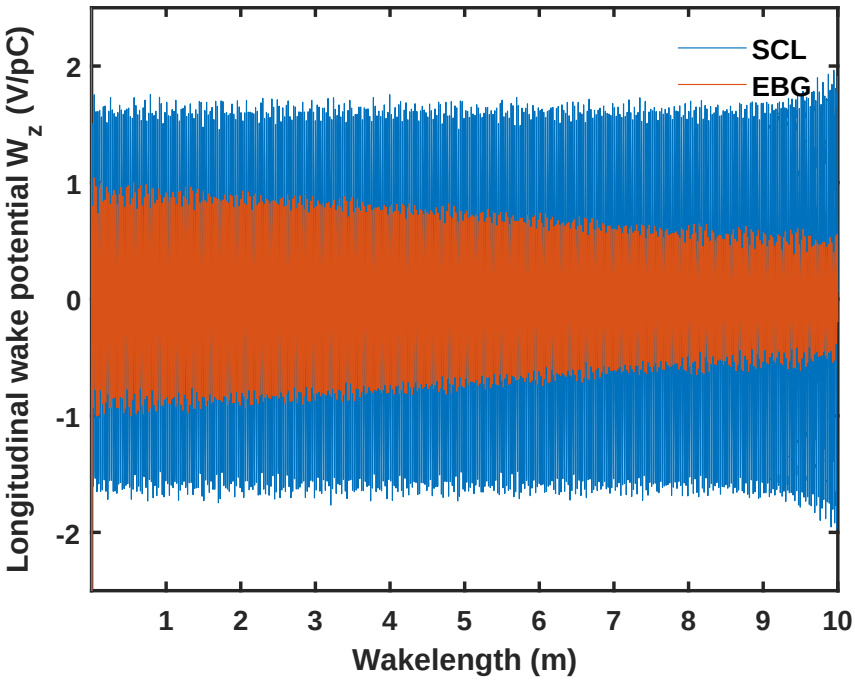

(a)

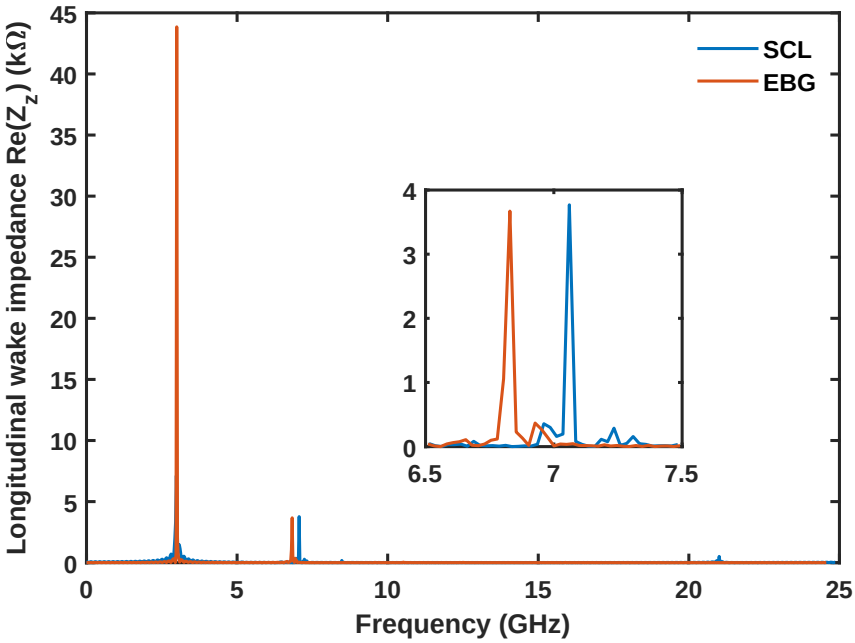

(b)

Figure 3.6: (a) Numerical simulation of the longitudinal wake potential in the EBG structure on a line parallel to the beam propagation line and displaced 2 mm in the x direction; the longitudinal wakes of the SCL structure in Chapter 2 is also shown for comparison. (b) Longitudinal wake impedances (spectra) of the EBG and SCL structures.

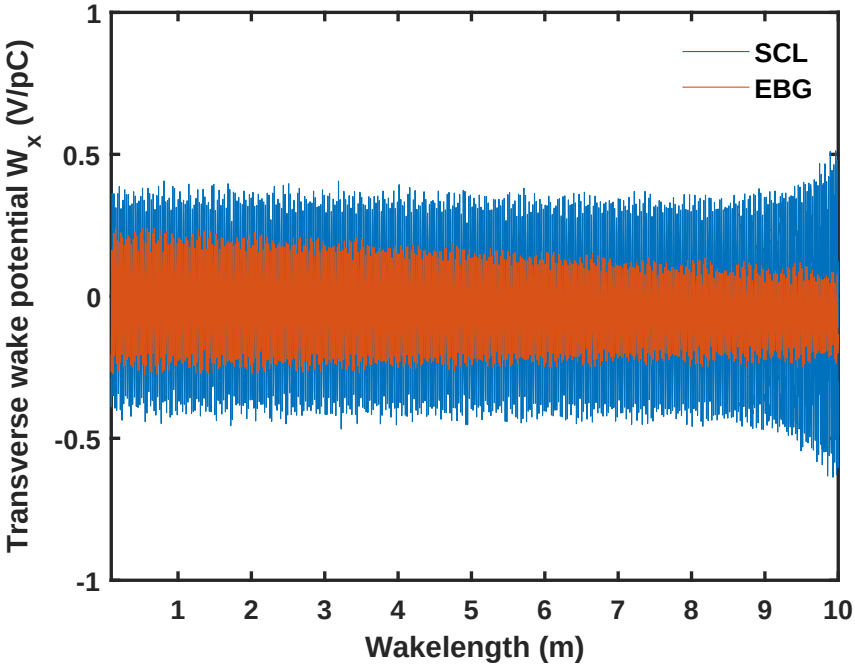

(a)

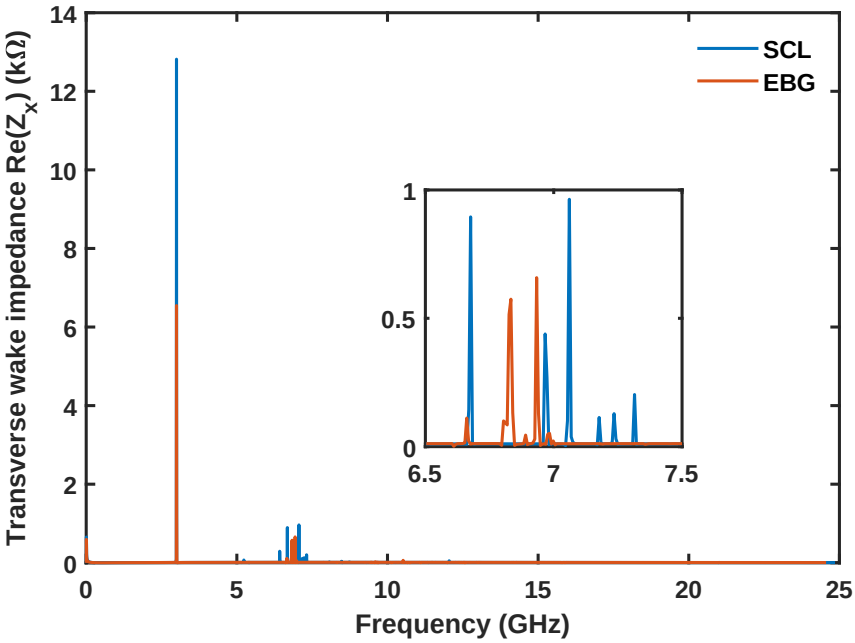

(b)

Figure 3.7: (a) Numerical simulation of the transverse wake potential in the EBG structure on a line parallel to the beam propagation line and displaced 2 mm in the x direction; the transverse wakes of the SCL structure in Chapter 2 is also shown for comparison. (b) Transverse wake impedances (spectra) of the EBG and SCL structures.

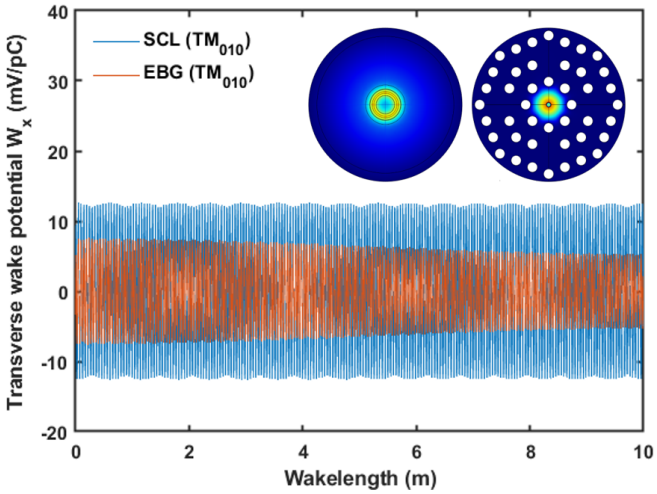

(a)

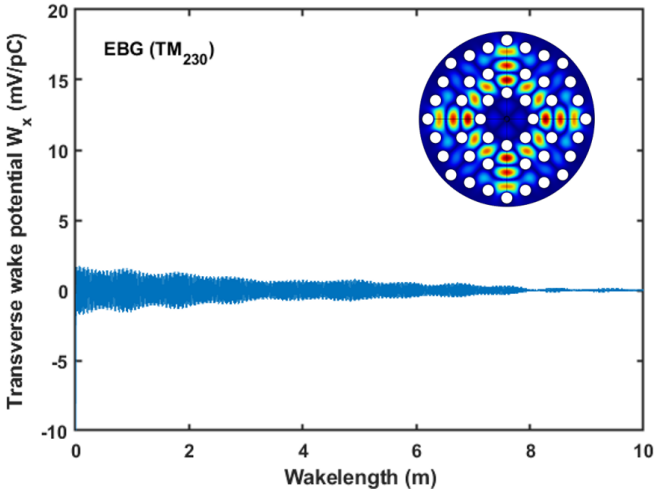

(b)

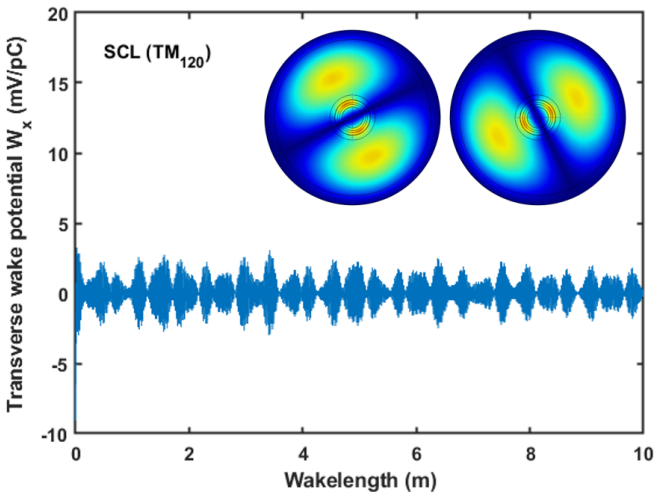

(c)

Figure 3.8: Transverse wake potentials as a function of the wakelength for each mode in the EBG and SCL structures: (a) TM_{010}-like fundamental modes (EBG and SCL); (b) TM_{230}-like quadrupole mode (EBG); (c) TM_{120}-like dipole mode (SCL).

optimization of the EBG cavities. In particular, the hybrid strategy has been used to design a 27-MeV 3-GHz EBG tank closed with full ECs. The simulated frequency of the EBG tank $\pi/2$ mode is $f_{\pi/2,\mathrm{sim}} = 2.998\,09\,\mathrm{GHz}$, very close to the nominal value $f_{\pi/2,\mathrm{ref}} = 2.997\,92\,\mathrm{GHz}$. The calculated stopband is very small, being about 292 kHz. Moreover, an accelerating field nonuniformity as small as $\sigma_R = 1.1\,\%$ has been calculated. The typical linac figures of merit of the optimized EBG accelerating cavities has been compared with those pertaining to the accelerating cavities of the 27-MeV 3-GHz SCL tank, whose design is detailed in Chapter 2, having the same design specifications. The transit-time factor of the EBG accelerating cavities is about 8 % higher (SCL: 0.78, EBG: 0.84), approaching values typically found in higher energy linac cavities. The Q factor of the EBG accelerating cavities is about 30 % lower (SCL: 6180, EBG: 4032), suggesting considering higher $\pi/2$ mode frequency and/or higher proton beam input energy. Furthermore, the peak surface electric field in the EBG accelerating cavities is about 65 % lower (SCL: 93.2 MV/m, EBG: 32.6 MV/m). Thus, EBG cavities are very promising for the design of higher frequency and higher accelerating gradient proton linacs with low RF breakdown probability. As an example, by considering the Kilpatrick limit $E_k = 46.8\,\mathrm{MV/m}$ at $f_{\pi/2,\mathrm{ref}}$, a conservative peak surface electric field $E_s = 2E_k$ would allow to increase the accelerating gradient of the EBG tank by about three times ($E_0 = 45\,\mathrm{MV/m}$), thus reducing to one third its length. Higher values of $f_{\pi/2,\mathrm{ref}}$ would enable even higher accelerating gradients and more compact tanks, as well as lower losses. The longitudinal and transverse wake potentials excited by the proton beam in the EBG and SCL structures have been simulated and compared too. The contribution to the transverse wake potentials from each HOM has been recovered. The results confirm that the EBG structure effectively damps the transverse wake potential due to HOMs. As the value of $f_{\pi/2,\mathrm{ref}}$ increases, other design constraints must be carefully considered, such as the fabrication tolerances, the thermal stress at the innermost rod joints and the increasing wakefield effects.

4 WHISPERING GALLERY MODE THEORY

Dielectric microresonators with circular geometries (e. g. spheres, disks, rings, toroids and bubbles) support a special kind of optical propagation modes, which are known as whispering gallery modes (WGMs). Light is strongly confined within WGM microresonators via total internal reflection at the boundary between the microresonator surface and the surrounding medium [97]. Thus, light undergoes several hundreds of revolutions along circular orbits. This leads to peculiar properties owned by WGM microresonators, including very high power density, extremely small mode volume, very high quality factors and very narrow spectral linewidth [44], [98]. Furthermore, WGM microresonator are characterized by submillimeter-scale volumes (diameters vary from tens of micrometers to hundreds of micrometers) and cost-saving manufacturing. Planar resonators can be fabricated onto silicon substrates by using conventional photolithography and etching techniques [99]. Optical fiber-based microresonators, such as microspheres and microbubbles, can be fabricated by melting the tip of a single-mode fiber or by heating a glass capillary via arc discharge, respectively [40], [98]. Moreover, a number of functional coatings can be easily deposited onto the surface of a sphere resonator by the dip-coating method [100]. All the remarkable properties of the WGM resonators described so far make them a valuable alternative to the traditional optical microresonators, such as the Fabry-Pérot cavities.

WGMs are excited in a microresonator via evanescent field coupling which can be provided by different input couplers. For planar WGM resonators, integrated waveguides are preferred in order to obtain high circuit integration, mechanical stability and cost-saving manufacturing [37], [99]. For optical fiber-based WGM resonators, the most common coupling techniques include prisms, half-blocks, angle-polished fiber tips, and tapered fibers. In this regard, tapered fibers allow to provide the most efficient coupling with the WGMs [101]–[103].

In the following sections, the general analytic theory for accurately describing a WGM dielectric resonator evanescently coupled with an input waveguide is illustrated. In particular, the mathematical formalism pertaining to the WGMs supported by a multilayer microresonator with circular geometry is first introduced. Then, the coupled mode theory is used to model the optical coupling of the WGMs with the input waveguide. The space and time formulations of the coupling of modes are both taken into account. Finally, the response of the coupling system to an excitation optical signal is given in terms of power transmittance.

4.1 ANALYTICAL MODEL OF A MULTILAYER WGM MICRORESONATOR

To illustrate the WGM theory, a multilayer sphere resonator coupled with an adiabatically-tapered optical fiber is considered, as shown in Figure 4.1. The z-axis is the direction of propagation of the input fiber modes. The origin of the global x and y coordinates is at the center of the taper waist. The coordinates of the multilayer sphere are represented by the usual variables r, θ and ϕ for the radial, polar and azimuthal components, respectively. The polar direction $\hat{\boldsymbol{\theta}}$ is perpendicular to the equatorial plane and the effective direction

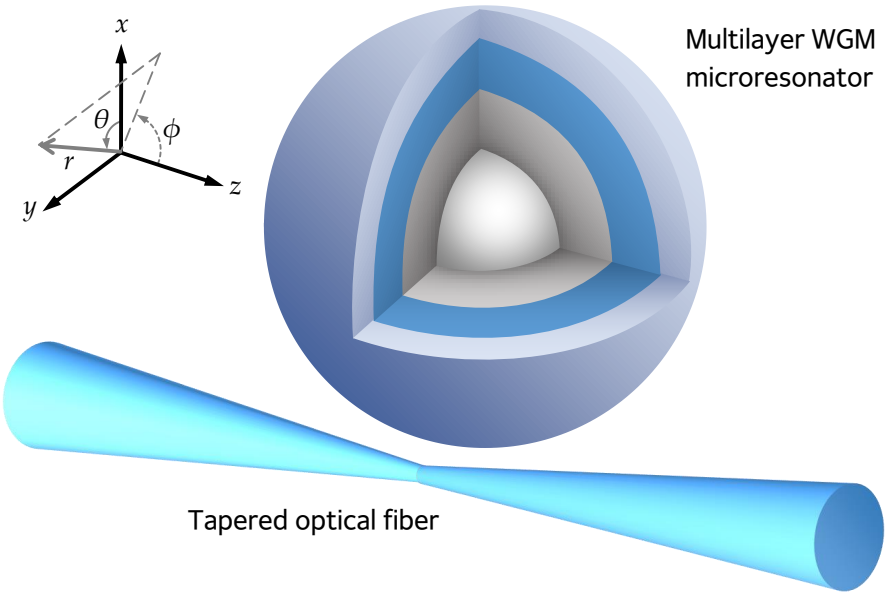

Figure 4.1: 3D sketch of a multilayer WGM sphere microresonator coupled with a tapered optical fiber.

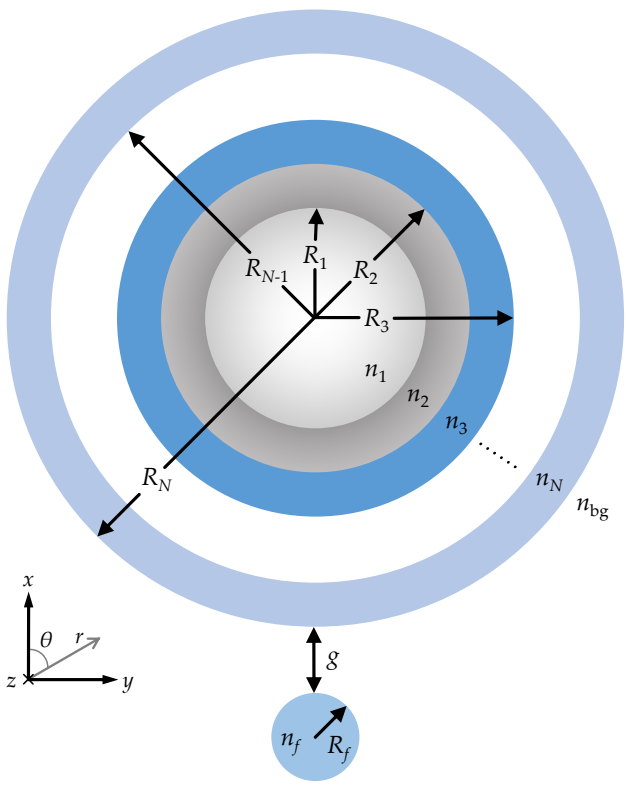

Figure 4.2: Cross-section of a multilayer WGM sphere microresonator coupled with a tapered optical fiber. The cross-section of the taper waist is shown. .

of propagation of the WGMs within the sphere is along the $\hat{\boldsymbol{\phi}}$ direction, in the equatorial plane. Even though a tapered fiber and a spherical resonator are considered here, the theory described in the following is general and it can be applied to any WGM resonator and any waveguides used for input/output coupling.

In Figure 4.2, the cross-sections of the N-layer microresonator and the fiber taper waist are shown. The ith microresonator layer has a radius R_i and a uniform refractive index n_i. The surrounding background medium is supposed to have a uniform refractive index $n_{\text{bg}} < n_N$. The refractive index of the taper core is n_f, the radius of the taper waist is R_f. The N-layer sphere resonator is at a distance g from the taper waist. It is worth noting that, for a fused tapered fiber with a waist diameter ranging from a few micrometers to tens of micrometers, the modes are those of an air-clad fiber (the power originally confined in the core leaks into the cladding).

The em fields propagating in a spherical volume with a uniform refractive index, n, are the solutions of the well-known Helmholtz wave equation [52]:

$$\nabla^2\Psi(r,\theta,\phi) + k^2 n\Psi(r,\theta,\phi) = 0, \tag{4.1}$$

where the differential operator ∇^2 is expressed in spherical coordinates; k is the wave vector in vacuum; $\Psi(r,\theta,\phi)$ is a scalar function that represent either the electric or magnetic field component. If the polarization direction of the em fields is supposed to be constant throughout all points in space, the method of separation of variables can be applied and the solutions of (4.1) can be expressed in the following form:

$$\Psi(r,\theta,\phi) = N_s R(r)\Theta(\theta)\Phi(\phi), \tag{4.2}$$

where $R(r)$, $\Theta(\theta)$ and $\Phi(\phi)$ are the radial, polar and azimuthal contributions of the fields, respectively; N_s is a power normalization constant related to the power flowing through a cross section of the sphere, i. e. through a plane transverse to the $\hat{\boldsymbol{\phi}}$ direction (see the θ-r plane in Figure 4.2) [104]. As a consequence of the separation of variables, the solutions of (4.1) can be grouped in transverse electric (TE) and transverse magnetic (TM) modes. For TE modes, $\Psi(r,\theta,\phi) \equiv E_\theta$, and the electric field is parallel to the sphere surface, i. e. $\boldsymbol{E} = E_\theta\hat{\boldsymbol{\theta}}$, $E_r = E_\phi = 0$. For TM modes, $\Psi(r,\theta,\phi) \equiv H_\theta$, and the magnetic field is parallel to the sphere surface, i. e. $\boldsymbol{H} = H_\theta\hat{\boldsymbol{\theta}}$, $H_r = H_\phi = 0$ [104]. Maxwell's equations are used to calculate the other field components, H_r, H_ϕ, for TE modes, and E_r, E_ϕ, for TM modes, as will be illustrated in the following. The wave equation in (4.1) and its solutions in (4.2) apply to any layer of the microresonator shown in Figure 4.2. By substituting (4.2) in (4.1), the following expressions for the WGM field contributions in all sphere layers are obtained:

$$\Phi(\phi) = \mathrm{e}^{\pm \jmath m\phi}, \tag{4.3a}$$

$$\Theta(\theta) = \mathrm{e}^{-m\theta^2/2}H_p(\theta\sqrt{m}), \quad m \gg 1 \gg \theta, \tag{4.3b}$$

$$R(r) = \begin{cases} A_1 j_l(kn_1 r), & r \le R_1 \\ A_2 j_l(kn_2 r) + B_2 y_l(kn_2 r), & R_1 < r \le R_2, \\ \dots\dots\dots\dots\dots & \\ A_i j_l(kn_i r) + B_i y_l(kn_i r), & R_{i-1} < r \le R_i, \\ \dots\dots\dots\dots\dots & \\ A_N j_l(kn_N r) + B_N y_l(kn_N r), & R_{N-1} < r \le R_N, \\ A_{N+1}\mathrm{e}^{-\alpha(r-R_N)}, & r > R_N, \end{cases} \tag{4.3c}$$

where H_p is the Hermite polynomial of order $p = l - m$; j_l and y_l are the spherical Bessel function of the first and second kind of order l, respectively; A_i and B_i, $i = 1, \ldots, N+1$, are amplitude constants to be evaluated by applying the boundary conditions to the θ- and ϕ-polarized field components at the interfaces $r = R_i$; $\alpha = (\beta_l^2 - k^2 n_{\text{bg}}^2)^{1/2}$ is the exponential decay constant of the evanescent field outside the microresonator; β_l is the propagation constant of the WGM parallel to the microresonator surface. The substitution of (4.3) in (4.2) gives the complete expression for the $\text{WGM}_{l,m,n}$ fields of the multilayer microresonator. Each $\text{WGM}_{l,m,n}$ is uniquely described by the three integers l, m and n. The value m is the number of field maxima along the ϕ-direction; the value $l - m + 1$ is the number of field maxima along the θ-direction; the value n is the number of absolute field maxima along the r-direction. In the expression of $R(r)$, $B_1 = 0$ since $y_l(kn_1 r)$ is an unacceptable physical solution because it would give infinitely large WGM fields for $R_1 \to 0$. Moreover, the radial component of the WGM fields outside the microresonator ($r > R_N$) is approximated by an exponentially decay evanescent field [104].

In (4.3), only the expression of the radial field contribution, $R(r)$, takes different values to account for the $N-1$ separation interfaces, for which appropriate boundary conditions must be imposed. Since any layer corresponds to an equation in $R(r)$, any layer involves two boundary conditions, which require tangential fields be continuous across its interface. The tangential fields are calculated from Maxwell's equations, by using the expression of $R(r)$ in (4.3). For TE modes:

$$\begin{aligned} \boldsymbol{H} &= -\jmath \frac{1}{\omega\mu_0} \nabla \times \boldsymbol{E} \\ &= \jmath \frac{1}{\omega\mu_0} \left[-\jmath \frac{m}{r\cos\theta} E_\theta \hat{\boldsymbol{r}} + \left(\frac{1}{r} + \frac{\partial}{\partial r} \right) E_\theta \hat{\boldsymbol{\phi}} \right] \\ &\cong \frac{1}{\omega\mu_0} \frac{m}{r\cos\theta} E_\theta \hat{\boldsymbol{r}} + \jmath \frac{1}{\omega\mu_0} \frac{\partial E_\theta}{\partial r} \hat{\boldsymbol{\phi}}, \end{aligned} \tag{4.4}$$

where the approximation $\partial E_\theta / \partial r \gg E_\theta / r$ is used. For TM modes:

$$\begin{aligned} \boldsymbol{E} &= -\jmath \frac{1}{\omega\epsilon_0 n^2} \nabla \times \boldsymbol{H} \\ &= -\jmath \frac{1}{\omega\epsilon_0 n^2} \left[\jmath \frac{m}{r\cos\theta} H_\theta \hat{\boldsymbol{r}} + \left(\frac{1}{r} + \frac{\partial}{\partial r} \right) H_\theta \hat{\boldsymbol{\phi}} \right] \\ &\cong \frac{1}{\omega\epsilon_0 n^2} \frac{m}{r\cos\theta} H_\theta \hat{\boldsymbol{r}} - \jmath \frac{1}{\omega\epsilon_0 n^2} \frac{\partial H_\theta}{\partial r} \hat{\boldsymbol{\phi}}, \end{aligned} \tag{4.5}$$

where the approximation $\partial H_\theta / \partial r \gg H_\theta / r$ is used. By matching the tangential θ- and ϕ-polarized field components of TE and TM modes at $r = R_i$, $i = 1, \ldots, N$, a homogeneous linear equation system of the form $\mathrm{M}\boldsymbol{x} = \boldsymbol{0}$ is obtained, where $\boldsymbol{x} = [A_1, A_2, B_2, \ldots, A_N, B_N, A_{N+1}]^\intercal$ and

$$\mathrm{M} = \begin{bmatrix} \mathrm{M}_{11} & 0 & \ldots & 0 & \ldots & 0 \\ 0 & \mathrm{M}_{22} & \ldots & 0 & \ldots & 0 \\ \vdots & \vdots & \ddots & \vdots & & \vdots \\ 0 & 0 & \ldots & \mathrm{M}_{ii} & \ldots & 0 \\ \vdots & \vdots & & \vdots & \ddots & \vdots \\ 0 & 0 & \ldots & 0 & \ldots & \mathrm{M}_{NN} \end{bmatrix}, \tag{4.6}$$

where, for the first layer ($i = 1$),

$$\mathrm{M}_{11} = \begin{bmatrix} j_l(kn_1R_1) & -j_l(kn_2R_1) & -y_l(kn_2R_1) & 0 \\ n_1 j_l'(kn_1R_1) & -\chi_1 n_2 j_l'(kn_2R_1) & -\chi_1 n_2 y_l'(kn_2R_1) & 0 \end{bmatrix},$$

for the interior layers ($i = 2, \ldots, N-1$),

$$\mathrm{M}_{ii} = \begin{bmatrix} j_l(kn_iR_i) & y_l(kn_iR_i) & -j_l(kn_{i+1}R_i) & -y_l(kn_{i+1}R_i) \\ n_i j_l'(kn_iR_i) & n_i y_l'(kn_iR_i) & -\chi_i n_{i+1} j_l'(kn_{i+1}R_i) & -\chi_i n_{i+1} y_l'(kn_{i+1}R_i) \end{bmatrix},$$

for the last layers ($i = N$),

$$\mathrm{M}_{NN} = \begin{bmatrix} 0 & j_l(kn_NR_N) & y_l(kn_NR_N) & -1 \\ 0 & kn_N j_l'(kn_NR_N) & kn_N y_l'(kn_NR_N) & \chi_N \alpha_s \end{bmatrix},$$

and $\chi_i = 1$, $i = 1, \ldots, N$, for TE modes, $\chi_i = n_i^2/n_{i+1}^2$, $i = 1, \ldots, N$, for TM modes ($n_{N+1} \equiv n_{\mathrm{bg}}$). By imposing equal to zero the determinant of the matrix M in (4.6), the characteristic equation for the N-layer sphere microresonator is obtained. The characteristic equation relates the resonant wavelengths of the WGMs to the mode orders l and n.

4.2 COUPLING MODEL

The coupled-mode theory [105], [106] is applied to model the optical coupling between the microresonator $\mathrm{WGM}_{l,m,n}$ modes and the tapered fiber modes. The fiber fields are assumed to be linearly polarized (LP) and well-known analytic solutions are used to describe them [107]. Then, in the following, the coupling of the $\mathrm{WGM}_{l,m,n}$ with the $\mathrm{LP}_{0,X}$ modes are considered, where the 0 and X subscripts represent the azimuthal and radial orders, respectively, of the LP taper modes. The analytical coupling model also takes into account the coupling of modes both in space and time formulations [108].

The optical interaction between the fiber taper field, $\boldsymbol{F}_X$, and the microresonator field, $\boldsymbol{\Psi}_{l,m,n}$, is calculated via the following overlap integral:

$$\kappa_{xy}(z) = \frac{k^2}{2\beta_f}(n_{\mathrm{eff}}^2 - n_{\mathrm{bg}}^2) \iint \boldsymbol{\Psi}_{l,m,n} \cdot \boldsymbol{F}_X^* \, \mathrm{d}x \, \mathrm{d}y, \tag{4.7}$$

where β_f is the propagation constant of the LP mode and n_{eff} is the effective refractive index of the microresonator, which is related to the propagation constant of the WGM [104]. The integration in (4.7) is carried out over the transverse xy-plane at a fixed point along the longitudinal axis of the tapered fiber, i. e. the z-axis (see Figure 4.1). Then, $k_{xy}(z)$ is integrated along the z-axis over the interaction length, L, i. e.,

$$\kappa = \int_L \kappa_{xy}(z) \, \mathrm{d}z. \tag{4.8}$$

κ is the power coupling constant, whereas κ^2 is the fraction of the power transferred from the fiber to the microresonator over the interaction region [108]. It is worth noting that k_{xy} is proportional to $\mathrm{e}^{-\jmath\Delta\beta z}$, where $\Delta\beta = \beta_f - \beta_m$ is the phase mismatch between the LP mode and the WGM, whose propagation constant is $\beta_m = m/R_g$ [104], R_g is the radius of the guiding layer in which the WGM is confined.

The power coupling constant κ is also related to the time evolution of the coupled modes. By considering the microresonator as a lumped oscillator of energy amplitude $a_{\mathrm{WGM}}(t)$, the (weak) power coupling with the tapered fiber induces a (slow) time variation of $a_{\mathrm{WGM}}(t)$, which can be expressed by means of the following rate equation [108]:

$$\frac{\mathrm{d}}{\mathrm{d}t} a_{\mathrm{WGM}}(t) = \left(\jmath \omega_{\mathrm{WGM}} - \frac{1}{\tau_0} - \frac{2}{\tau_e} \right) a_{\mathrm{WGM}}(t) - \jmath \sqrt{\frac{2}{\tau_e \tau_r}} a_{\mathrm{in}}(t), \tag{4.9}$$

where $\tau_0 = Q_0/\omega_{\mathrm{WGM}}$ is the amplitude decay time-constant due to the intrinsic losses of the microresonator (including surface scattering, absorption and curvature losses); Q_0 is the intrinsic quality factor; ω_{WGM} is the $\mathrm{WGM}_{l,m,n}$ resonant frequency; $\tau_e = Q_e/\omega$ is the decay time-constant related to the coupling with the fiber; $Q_e = m\pi/\kappa^2$ is the external quality factor; κ is the foregoing power coupling constant; ω is the input excitation frequency; $\tau_r = 2\pi R_g/v_g \cong 2\pi R_g n_{\mathrm{eff}}/c$ is the revolution time in the guiding layer of the microresonator; a_{in} (t) is the energy amplitude of the excitation signal at the taper input section.

The transfer I/O characteristic of the coupling system shown in Figure 4.1 is found by considering the steady state form of the (4.9), thus obtaining a_{WGM}, and then applying the following power conservation rule:

$$\frac{|a_{\mathrm{in}}|^2}{\tau_r} = \frac{1}{\tau_r} \left| a_{\mathrm{in}} - \jmath \sqrt{\frac{2\tau_r}{\tau_e}} a_{\mathrm{WGM}} \right|^2 + \frac{2}{\tau_e} |a_{\mathrm{WGM}}|^2, \tag{4.10}$$

where the first term on the right-hand side is the non-resonant power transmitted directly to the tapered fiber output, while the second term is the resonant power coupled out of the microresonator [108]. Therefore, the transmittance of the coupling system can be expressed as:

$$T = \frac{|a_{\mathrm{out}}|^2}{|a_{\mathrm{in}}|^2} \tag{4.11}$$

where a_{out} is the amplitude of the signal at the tapered fiber output, i. e. $|a_{\mathrm{out}}|^2/\tau_r$ is equivalent to the right-hand side of (4.10).

5 OPTICAL COUPLING OF WGM MICRORESONATORS WITH TAPERED FIBERS FOR CHEMICAL/BIOLOGICAL SENSING APPLICATIONS

The comprehensive analytical model described in Chapter 4 has been used to design robust microresonator-based optical sensing set-ups [4]–[6]. In particular, microspheres and microbubbles evanescently side-coupled with a tapered fiber have been exploited for sensing of chemical/biological fluids in the visible and near infrared (NIR) wavelength ranges. The investigated set-ups allow light to selectively excite high-Q WGMs into the optical microresonators, thanks to a pair of identical long period gratings (LPGs) placed on both taper ends. The analytical model, implemented via a homemade code, has been first validated via experimental data. Then, a microbubble-based set-up has been used to detect different concentrations of aqueous sodium chloride (NaCl) and glucose ($C_6H_{12}O_6$) solutions. The microbubble response, in terms of the different resonance detuning shifts, to increasing analyte concentrations has been investigated. The simulation of the sensing set-up gives a numerical proof-of-concept toward the exploitation of novel sensing applications in medical diagnostic and environment monitoring. By exploiting the refractive index and/or absorption characteristics at suitable wavelengths, the sensing of several substances or pollutants can be predicted.

5.1 WGM-BASED SENSING APPLICATIONS

WGM microresonators, including microbubbles [40], microdisks [37] and microspheres [109], allow a strong confinement of light in very compact volumes with very low losses, leading to high Q-factor resonances. During the several round trips of the light signal, the WGM field evanescently couples with the surrounding environment. As a consequence, small variations of the microresonator size and/or its complex refractive index can induce significant changes in the Q-factor and/or resonant frequencies of the microresonator. Thanks to this attractive property, several WGM-based sensing applications are reported in literature, including the sensing of local temperature [109]–[113], refractive index [114], pressure [115], biological [27] and spectroscopic parameters [116]. The great potential of WGMs in biosensing applications by means of label-free detection down to single molecules was also proved [117]. Moreover, by suitable rare-earths doping, the WGM microresonators can be effectively employed to design and fabricate integrated light sources with narrow line emission [118].

Combining the peculiarities of optical fibers and WGM microresonators can provide great opportunities in the field of sensing especially. As an example, a coupling system for wavelength-selective addressing of different WGM microresonators along the same optical link can be used to develop distributed or quasi-distributed sensing applications. The first fiber-based setup for efficient coupling of light to a high-Q WGM microresonator is described in [119]. The setup is based on an LPG followed by a thick fiber taper, both of which are derived from the same fiber. The LPG allows the wavelength-selective excitation of high-order cladding modes for more effective coupling with WGMs. In this way, thicker and more robust tapers

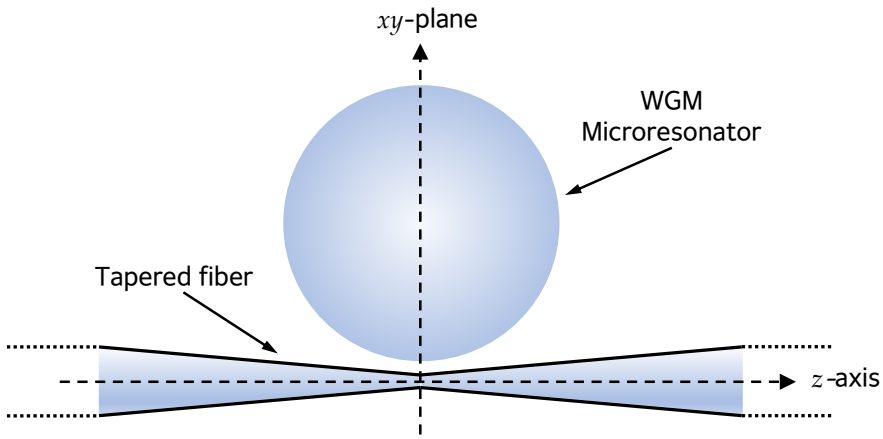

Figure 5.1: Sketch of the coupling system of an optical WGM microcavity by means of a tapered fiber.

with waist diameters larger than 15 μm (easier to fabricate than the usual 1-2 μm tapers) can be used for coupling. Further improvement is obtained by adding a second LPG, identical to first one, after the taper [120]. The system is now constituted by a pair of identical LPGs with a tapered fiber in between. The second LPG allows the light coupling back into the fiber core. Hence, all the information within the core mode is transmitted up to the fiber output and it can be collected by a single photodetector. It is worth noting that the pair of identical LPGs can operate in different wavelength bands within the range of the photodetector, thus allowing multiple selective coupling of spatially distributed or quasi-distributed WGM microresonators by means of different wavelengths.

In the following sections, two different sensing set-ups, similar to those described in [120], are considered. The two set-ups consist of either a microsphere or a microbubble coupled to a thick tapered fiber. The analytic theory of Chapter 4, implemented via homemade code, has been used for simulating these two set-ups. The modelling approach has been well validated with the experimental results.

5.2 OVERVIEW OF THE WGM MICRORESONATOR-TAPER COUPLING SYSTEM

Figure 5.1 shows a sketch of the simulated coupling system, which constists of an optical WGM microcavity coupled with a tapered fiber. In Figure 5.1, the pair of identical LPGs on both sides of the taper are not shown. In fact, the effects of the LPGs in the transmittance calculation can be neglected, since the LPGs simply allow the selective fiber mode excitation. Furthermore, in the transmittance calculation, given by (4.11), the output light is normalized with respect to the input one.

In Figure 5.2, the simulated microsphere- and microbubble-based coupling systems are shown. In particular, the cross-sections of the microresonators and the taper waist are shown. Silica glass is considered for both the microsphere and the microbubble, as well as for the tapered fiber.

5.3 MANUFACTURING OF WGM MICRORESONATORS, TAPERS AND LPGS

Adiabatic tapered fibers were fabricated via heating and pulling of a commercially available boron-germanium co-doped single-mode optical fiber

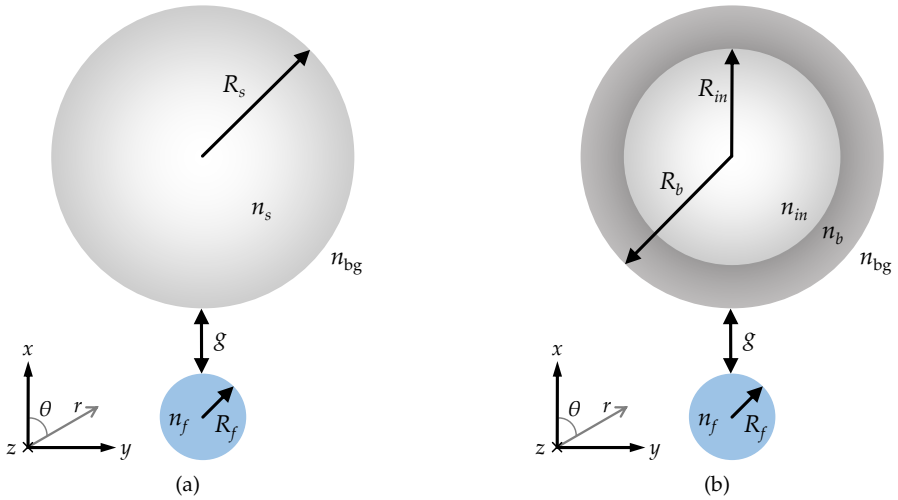

Figure 5.2: Sketch of the simulated coupling systems consisting of a tapered fiber coupled with (a) a microsphere and (b) a microbubble. The microsphere, the microbubble and the taper are made of silica glass.

(Fibercore PS1250/1500) [121]. In particular, the fiber core and cladding diameters are 6.9 μm and 124.6 μm, respectively. Tapers with a diameter ranging from 15 to 18 μm are manufactured to guide/handle the cladding modes of interest. It is worth pointing out that, for an efficient coupling of these cladding modes to the WGM microresonators, a partial tapering of the optical fiber is essential to shrink the optical field size and to increase the evanescent field [119]. However, the average diameter of the manufactured tapered fibers is one order of magnitude thicker than that of standard fiber tapers (1-2 μm), allowing for improved robustness of the coupling structures in practical applications.

Regarding the fabrication of the LPGs, a point-to-point technique employing a KrF excimer laser (Lambda Physic COMPex 110) is used to inscribe the gratings [122]. Two different pairs of LPGs are manufactured with a grating period $\Lambda = 340$ μm and $\Lambda = 365$ μm, respectively, and a grating length $L = 18.7$ mm and $L = 20.1$ mm, respectively (55 grating planes).

The silica microspheres and microbubbles are manufactured as described in [40], [121]. The diameters of the resonators range from 260 μm to 290 μm, for microspheres, and from 380 μm to 500 μm, for microbubbles. In both cases, the diameters are large enough to consider the free spectral range (FSR) significantly smaller than the bandwidth of the LPGs [119].

The experimental setup used for monitoring the transmission spectra consists of two fiber pigtailed tunable external cavity lasers (Anritsu Tunics Plus, linewidth 300 kHz), covering the spectral range from 1390 nm to 1640 nm. An optical spectrum analyzer (OSA–Ando AQ6317B) for detecting the signals is also employed. The two WGM microresonator-based coupling systems are tested by using the same laser sources, which can be finely and continuously swept in the spectral range of interest within few GHz, and a single photodetector connected to a commercially available oscilloscope.

5.4 DESIGN AND EXPERIMENTAL VALIDATION OF THE COUPLING SYSTEM

The simulations are carried out by employing the experimental parameters detailed in Section 5.3. In particular, an adiabatic fiber taper with a radius R_f = 9 μm is considered. The simulated microsphere and microbubble are made of silica glass. The refractive index wavelength dispersion of the silica glass is taken into account via a proper Sellmeier formula [123]. The microsphere radius is R_s = 145 μm, whereas the microbubble external and internal radii are R_b = 200 μm and R_{in} = 196.7 μm, respectively. The simulations are performed by considering air as the surrounding background medium. Moreover, the microbubble is considered empty. The simulated wavelength range is centered on λ_c = 1613.3 nm, which is the center wavelength of the experimental attenuation band of the LPGs [120].

To find the optimal value of the gap g, a number of simulations are performed by considering different gap values, $g = 0, 10, 100, 200, 500, 1000$ nm. For each value of g, the simulated transmittance T is compared with the experimental one. Both setups employing the microsphere and the microbubble are taken into account.

5.4.1 *Microsphere-based set-up*

Figure 5.3a shows the transmittance T of the microsphere-based setup, calculated for three different $\mathrm{WGM}_{l,m,n}$, as a function of the radial order X of the $\mathrm{LP}_{0,X}$ cladding modes, considering a gap g = 0 nm (i. e., taper and microsphere in mechanical contact). The lowest transmittance dip, which corresponds to the highest coupling with microsphere, can be attained for the $\mathrm{WGM}_{774,774,3}$ by exciting with the fiber $\mathrm{LP}_{0,5}$ cladding mode through the LPG. The simulated and measured resonances of the $\mathrm{WGM}_{774,774,3}$, expressed in terms of the detuning $\Delta\omega$ ($\Delta\omega$ = 0 MHz is equivalent to $\lambda = \lambda_c$), are shown in Figure 5.3b. The simulated results are in excellent agreement with the experimental ones, in terms of detuning $\Delta\omega$, and in good agreement, in terms of transmittance T. In fact, by exciting the $\mathrm{WGM}_{774,774,3}$, the simulated transmittance of the microsphere-based coupling system reaches a minimum of T = 0.52, while, in the experiment, the measured transmittance is about T = 0.65. The small discrepancy can be explained by considering that the actual total losses are higher. However, it is worth nothing that, in Figure 5.3a, the transmittance simulated for the $\mathrm{WGM}_{774,774,3}$ coupled with the $\mathrm{LP}_{0,7}$, indicated with a dot marker, is T = 0.66, practically coincident with the measured transmittance, for the same LP radial order. A very good agreement between simulated and experimental Q factors is also obtained. The maximum Q factor achieved in the experiment is $Q_{\mathrm{exp}} = 1.1 \times 10^8$; the Q factor of the simulated $\mathrm{WGM}_{774,774,3}$ coupled with the $\mathrm{LP}_{0,5}$ is $Q_{\mathrm{sim}} = 0.3 \times 10^8$, this slightly lower value being probably due to an overestimation of the scattering losses. Finally, it should be noted that the analytical model allows to retrieve the WGM modal orders as well as the same (or very close) LP modal orders experimentally observed.

Figure 5.4 shows the transmittance T of the microsphere-based setup, calculated for the gap values, $g = 0, 10, 100, 200, 500, 1000$ nm. For each value of g, the transmittance due to the $\mathrm{WGM}_{774,774,3}$, which exhibits the lowest dip among the coupled WGMs, is plotted as a function of the radial order X of the fiber modes. In other words, the $\mathrm{WGM}_{774,774,3}$ transmittance is predominant with respect to the contribution of the other WGMs. Except for large gap values (g = 1000 nm), the simulated minimum transmittance is almost the same in all cases. Instead, the radial order of the fiber modes slightly increases

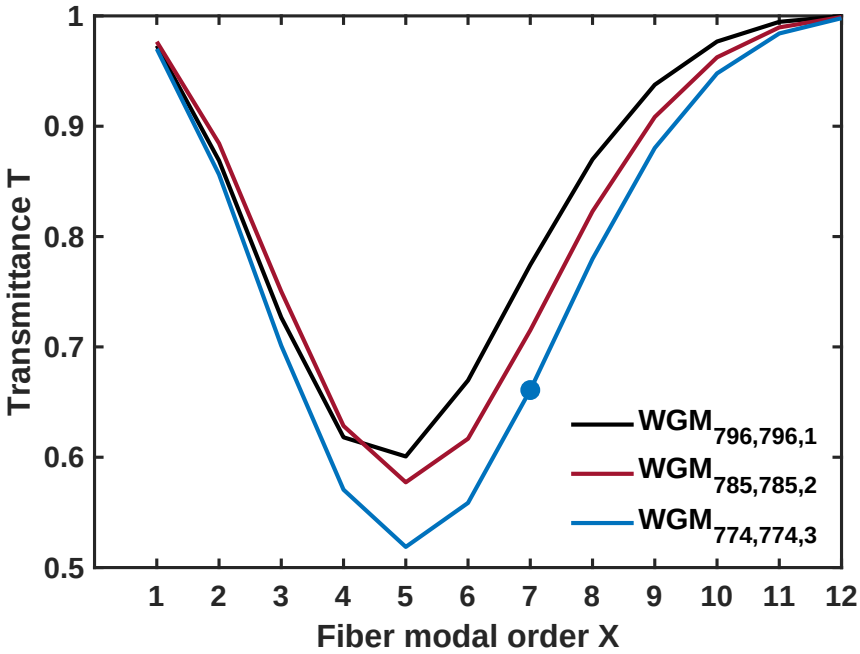

(a)

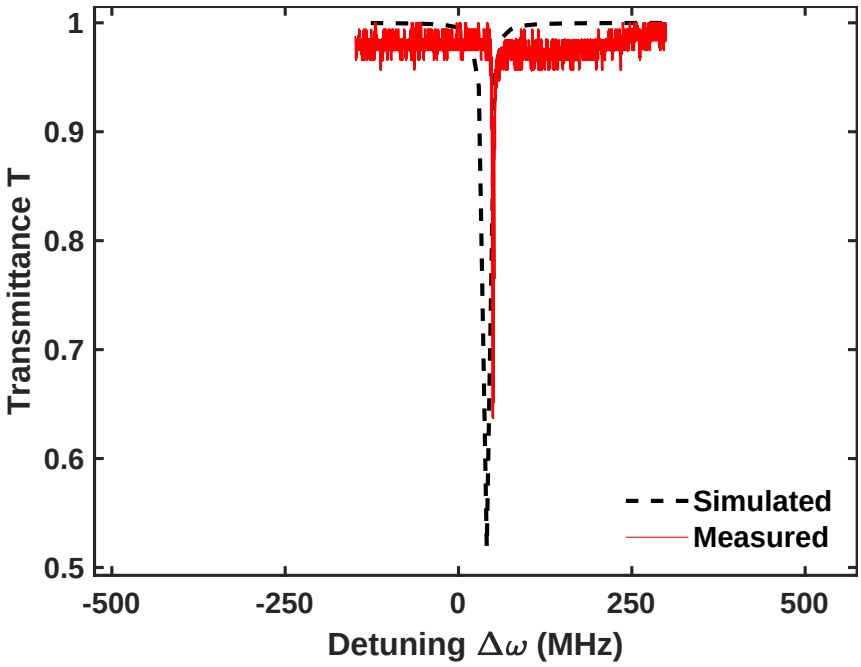

(b)

Figure 5.3: (a) Transmitted power of the microsphere-based setup, calculated for three resonant $WGM_{l,m,n}$, as a function of the modal order X of the $LP_{0,X}$ cladding modes, with a gap $g = 0\,\text{nm}$. The simulated transmittance of the $WGM_{774,774,3}$ coupled with the $LP_{0,7}$, indicated by a dot marker, is practically coincident with the measured transmittance. (b) Transmittance of the $WGM_{774,774,3}$, excited by the $LP_{0,5}$, as a function of the detuning $\Delta\omega$, with a gap $g = 0\,\text{nm}$. Both the simulated and measured resonances are shown. In (a) and (b), the background medium is air.

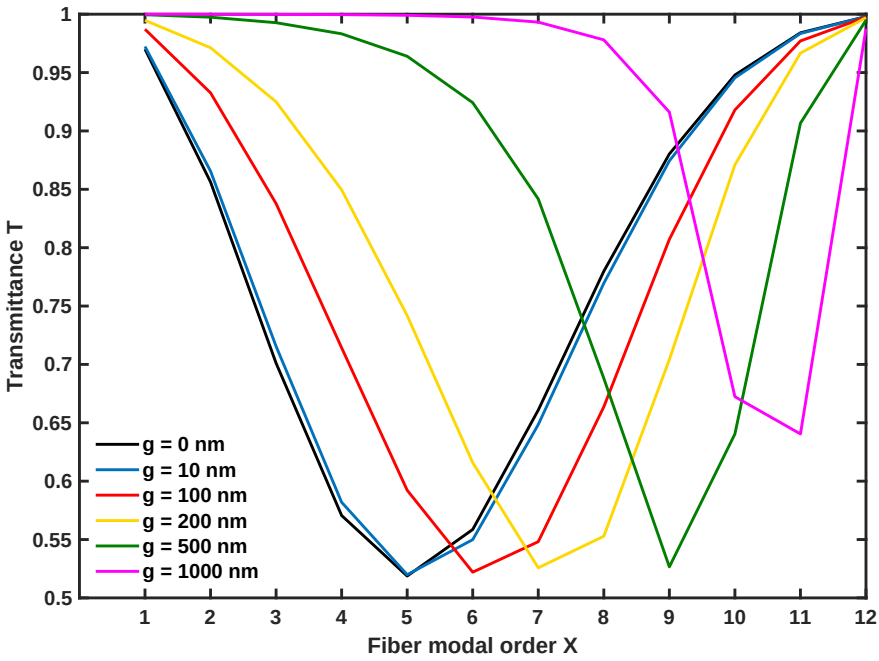

Figure 5.4: Transmitted power of the microsphere-based setup, calculated for different gap values, ranging from $g = 0$ nm to $g = 1000$ nm (background medium: air).

as the gap increases, revealing the influence of g on the phase matching between the WGMs and LP modes.

5.4.2 *Microbubble-based set-up*

Figure 5.5a reports the transmittance T of the microbubble-based setup, calculated for three different $\mathrm{WGM}_{l,m,n}$, as a function of the radial order X of the $\mathrm{LP}_{0,X}$ cladding modes, considering a gap $g = 0$ nm (i. e., taper and microbubble in mechanical contact). The lowest transmittance dip, which corresponds to the highest coupling with the microbubble, can be attained for the $\mathrm{WGM}_{998,998,3}$ by exciting with the fiber $\mathrm{LP}_{0,4}$ cladding mode through the LPG. Both the simulated and measured resonant detuning of the $\mathrm{WGM}_{998,998,3}$ are shown in Figure 5.5b. The simulated transmittance of the microbubble-based coupling system reaches a minimum of $T = 0.51$ (indicated with a dot marker), practically coincident with the measured value, even if referring to an LP radial order slightly lower than the experimental one ($\mathrm{LP}_{0,7}$). Furthermore, a difference of about 50 MHz is found between the simulated and measured resonant detuning. However, such a difference is negligible, since, at $\lambda_c = 1613.3$ nm, it is equivalent to a wavelength shift less than 1 pm. Also for the microbubble-based set-up, a very good agreement between simulated and experimental Q factors is obtained. The maximum Q factor achieved in the experiment is $Q_{\mathrm{exp}} = 9.8 \times 10^7$; the Q factor of the simulated $\mathrm{WGM}_{998,998,3}$ coupled with the $\mathrm{LP}_{0,4}$ is $Q_{\mathrm{sim}} = 2.7 \times 10^7$. As in the microsphere case, the slightly lower value of Q_{sim} is probably due to an overestimation of the bubble scattering losses.

Figure 5.6 shows the transmittance T of the microbubble-based setup, calculated for the gap values, $g = 0, 10, 100, 200, 500, 1000$ nm. For each value of g, the transmittance due to the $\mathrm{WGM}_{998,998,3}$, which exhibits the lowest dip

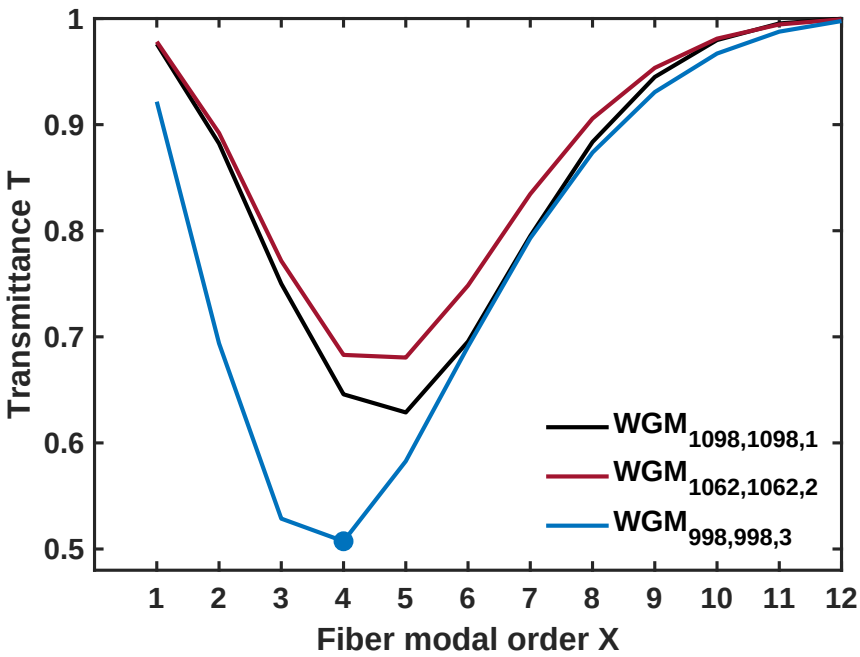

(a)

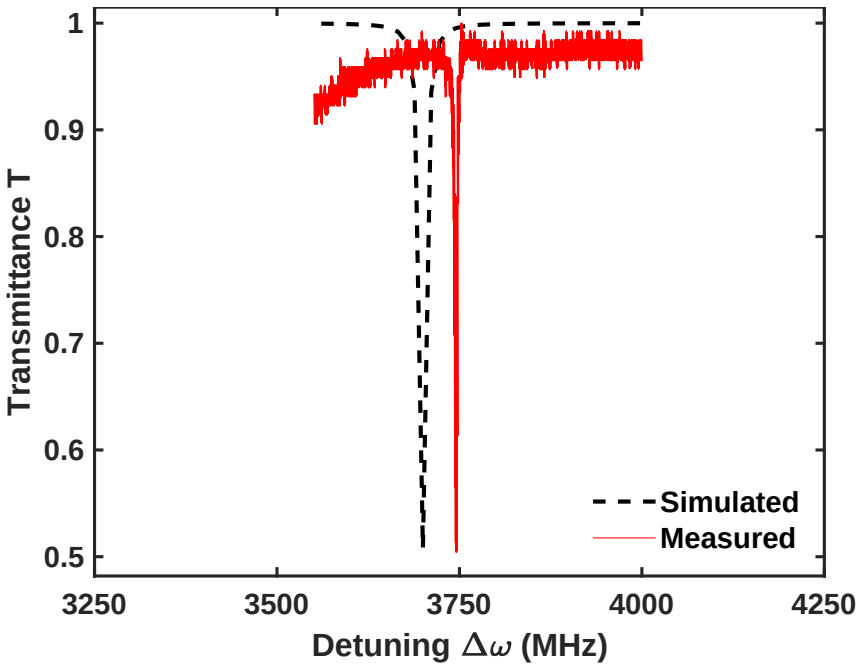

(b)

Figure 5.5: (a) Transmitted power of the microbubble-based setup, calculated for three resonant $WGM_{l,m,n}$, as a function of the modal order X of the $LP_{0,X}$ cladding modes, with a gap $g = 0\,\text{nm}$. The simulated transmittance of the $WGM_{998,998,3}$ coupled with the $LP_{0,4}$, indicated by a dot marker, is practically coincident with the measured transmittance. (b) Transmittance of the $WGM_{998,998,3}$, excited by the $LP_{0,4}$, as a function of the detuning $\Delta\omega$, with a gap $g = 0\,\text{nm}$. Both the simulated and measured resonances are shown. In (a) and (b), the background medium is air and the bubble is empty.

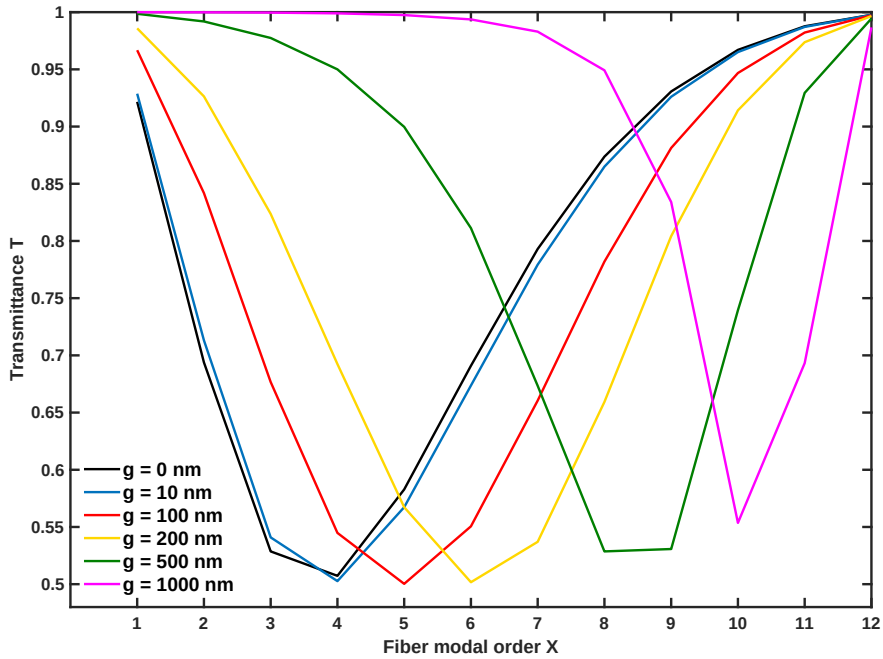

Figure 5.6: Transmitted power of the microbubble-based setup, calculated for different gap values, ranging from $g = 0$ nm to $g = 1000$ nm (background medium: air; empty bubble).

among the coupled WGMs, is plotted as a function of the radial order X of the fiber modes. In this case, the $WGM_{998,998,3}$ transmittance is predominant with respect to the contribution of the other WGMs. As in the microsphere case, except for large gap values ($g = 1000$ nm), the simulated minimum transmittance is almost the same in all cases, while the radial order of the fiber modes slightly increases as the gap increases. It is worthwhile noting that, in Figure 5.4 and Figure 5.6, the critical coupling condition can be achieved by considering different fiber optic modal order.

Figure 5.7 illustrates the normalized electric field of the microbubble $WGM_{998,998,3}$ evanescently coupled to the normalized electric field of the fiber $LP_{0,4}$ cladding mode, both fields obtained from the homemade code. The four radial maxima of the $LP_{0,4}$ is evident as well as the third radial order of the $WGM_{998,998,3}$.

5.5 MICROBUBBLES FOR CHEMICAL/BIOLOGICAL FLUID SENSING

As a numerical proof-of-concept toward the exploitation of chemical/biological fluid sensing applications, the sensitivity of the microbubble-based setup to different concentrations of an aqueous sodium chloride (NaCl) solution has been simulated. Again, the analytical model illustrated in Chapter 4 has been used for simulations. The response of the microbubble, in terms of the different WGMs resonance detuning shifts, to an increasing NaCl concentration has been investigated. The simulations are performed with the same microbubble used in Section 5.4. The simulated wavelength range is 1550 ± 1.5 nm. The simulated NaCl concentrations are in the range $0 \div 10$ wt.%, with an increment of 2.5 wt.%. The refractive indices of the solutions within the bubble are

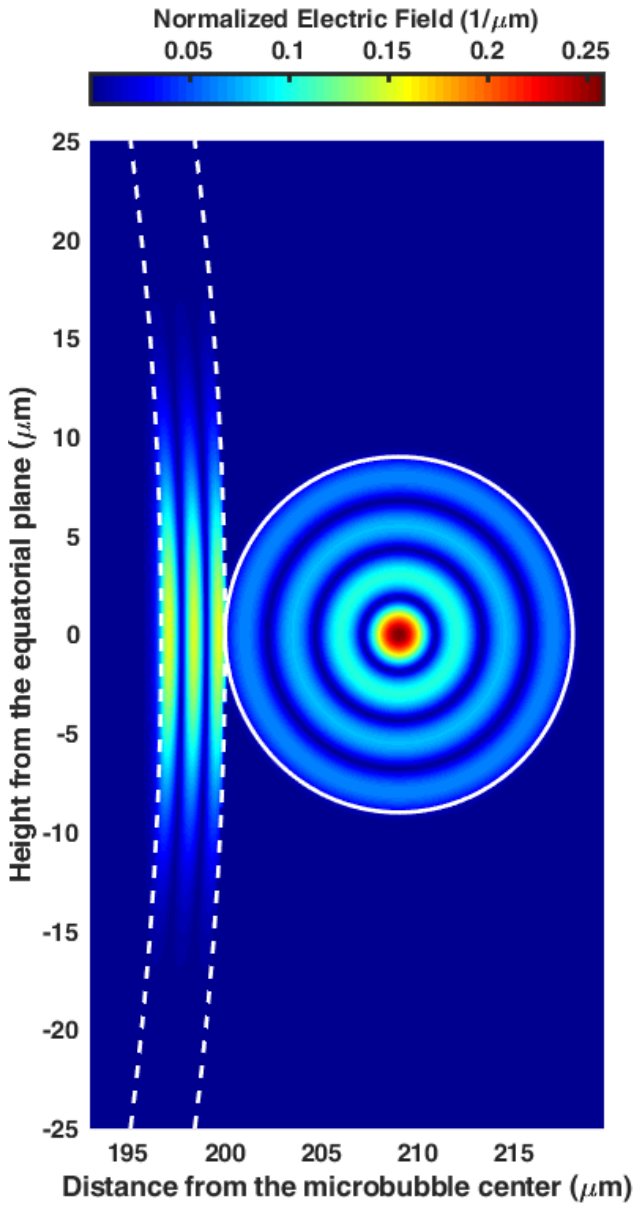

Figure 5.7: Distribution of the normalized electric fields confined in the microbubble glass layer (on the left) and in the fiber taper (on the right) for the $WGM_{998,998,3}$ coupled with the $LP_{0,4}$, gap $g = 0\,\text{nm}$.

Table 5.1: Refractive index dispersion of an aqueous sodium chloride (NaCl) solution as a function of the mass concentration. The refractive indices are calculated from (5.1).

w (wt.%)	0	2.5	5	7.5	10
n_{in}	1.3162	1.3203	1.3245	1.3287	1.3331

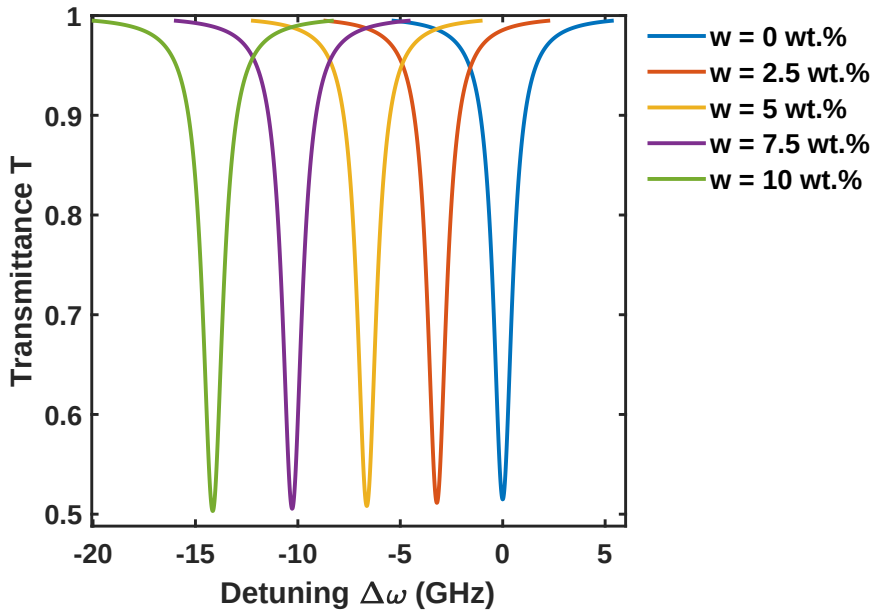

Figure 5.8: Resonance shift of the $WGM_{1149,1149,1}$, coupled with the $LP_{0,11}$, as a function of the increasing NaCl concentration w.

calculated as a function of the NaCl concentrations, according to the following dispersion formula [124]:

$$n_{in} = Aw^3 + Bw^2 + Cw + D, \tag{5.1}$$

where $A = -0.0800$, $B = 0.0740$, $C = 0.1620$, $D = 1.3162$ and w is the mass fraction of the NaCl. Table 5.1 lists the refractive indices considered in simulations, calculated through the dispersion formula in (5.1). For each concentration value, the same three WGMs with increasing radial orders are simulated: $WGM_{1149,1149,1}$, $WGM_{1117,1117,2}$ and $WGM_{1067,1067,3}$. As expected, the microbubble resonances are sensitive to the concentration increase. In particular, the resonant wavelength (detuning) of each WGM increases (decreases) as the concentration increases. In Figure 5.8, the detuning shift of the $WGM_{1149,1149,1}$ is shown. As the NaCl concentration, w, increases, the transmittance dip moves to the left and this shift is proportional to the concentration. The same behavior is observed for the other two simulated WGMs. In Figure 5.9, the detuning shift of the $WGM_{1117,1117,2}$ is shown. Compared to the previous case, the frequency shift is more evident. The higher radial order of the $WGM_{1117,1117,2}$ allows a stronger coupling of the evanescent field with the solutions inside the bubble. That is, the response to refractive index variations, as given by (5.1), is more sensitive. For the same reason, the frequency shift of the $WGM_{1067,1067,3}$, illustrated in Figure 5.10, is much more evident than those ones shown in Figure 5.8 and Figure 5.9.

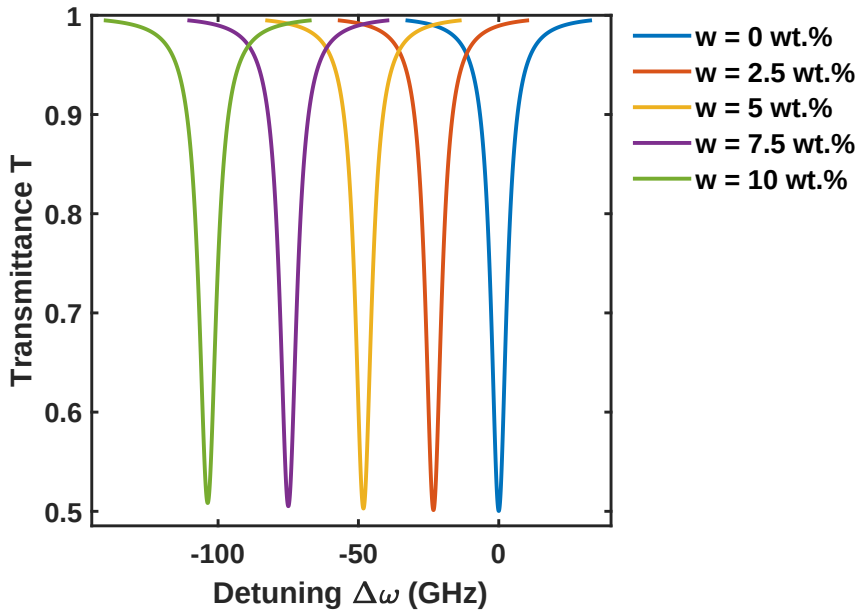

Figure 5.9: Resonance shift of the $WGM_{1117,1117,2}$, coupled with the $LP_{0,12}$, as a function of the increasing NaCl concentration w.

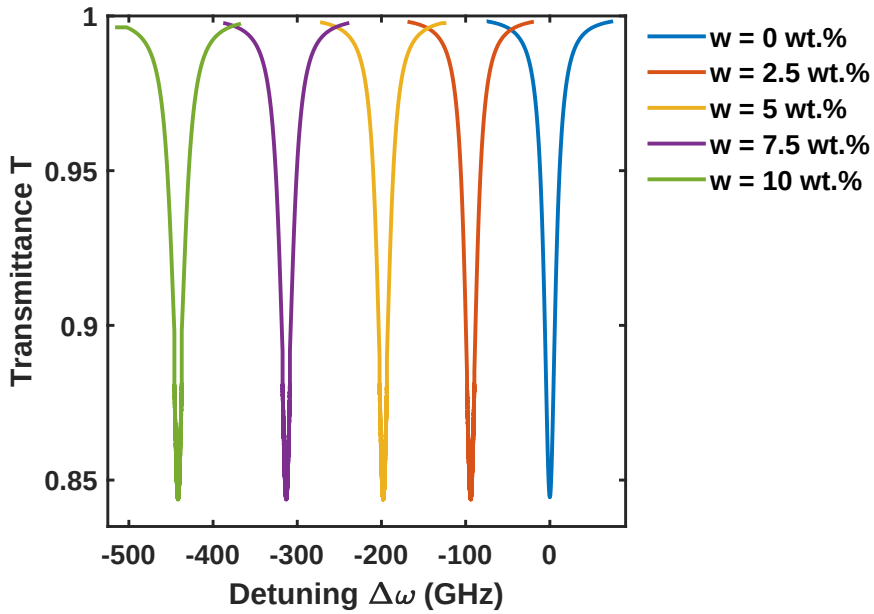

Figure 5.10: Resonance shift of the $WGM_{1067,1067,3}$, coupled with the $LP_{0,12}$, as a function of the increasing NaCl concentration w.

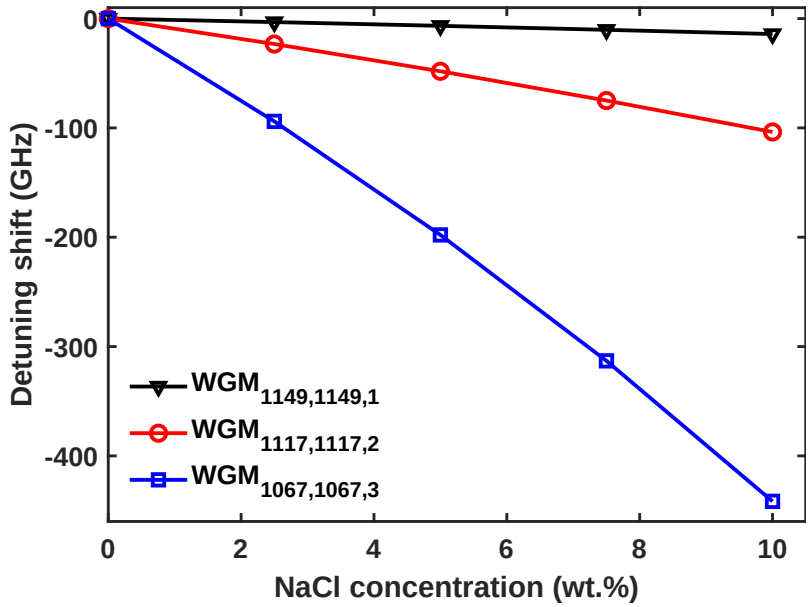

Figure 5.11: Detuning shift of the simulated microbubble WGMs as a function of the NaCl concentration expressed in terms of mass fraction.

By observing the Figures 5.8–5.10, a nearly linear relationship between the frequency shift of the bubble resonances and the increasing NaCl concentration is observed. In Figure 5.11, the detuning shift of the simulated WGMs as a function of the NaCl concentration is shown. As expected, the WGMs with a higher number of radial maxima are more sensitive to the refractive index variation induced by the increasing concentration. In fact, in these cases, the WGM fields are less confined in the glass layer of the microbubble, because of the larger evanescent field coupled with the solution inside the bubble. The average slope of the curves in Figure 5.11 represents the sensitivity values, S, of the microbubble-based sensor, which are approximately equal to (i) $S = -1.42$ GHz/wt.% for the $\mathrm{WGM}_{1149,1149,1}$; (ii) $S = -10.37$ GHz/wt.% for the $\mathrm{WGM}_{1117,1117,2}$; (iii) $S = -44.16$ GHz/wt.% for the $\mathrm{WGM}_{1067,1067,3}$. The feasibility investigation of a similar setup, by considering the fabrication tolerances, was reported in [125]. This aspect requires great care since it could represent a weakness. In fact, the uncertainty on the fiber taper and the microresonator geometry or the gap between the microresonator and the fiber taper must be considered in the actual use of these devices for sensing applications. Peculiar calibration of the WGM-based sensing set-up is required. Alternatively, to mitigate the effect of uncertainty on geometrical dimensions, a double-step approach can be followed [125]. In particular, the geometrical and physical parameters of the set-up can be effectively recovered via simple transmittance measurements. To this aim, a method based on the electromagnetic model of the device suitably integrated with a global search approach, such as the PSO, can be exploited. In [125], it was demonstrated that, by supposing the largest error in geometrical characterization of the gap between the microresonator and the taper equal to 0.03 %, very accurate sensing measurements can be performed. Therefore, such a double-step approach makes feasible a number of different applications, from environment monitoring to medicine diagnostics, involving the set-up illustrated in Figure 5.1.

Table 5.2: Refractive index dispersion of an aqueous glucose ($C_6H_{12}O_6$) solution as a function of the mass concentration [126].

w (wt.%)	0	5	10	15	20
n_{in}	1.3332	1.3402	1.3477	1.3555	1.3635

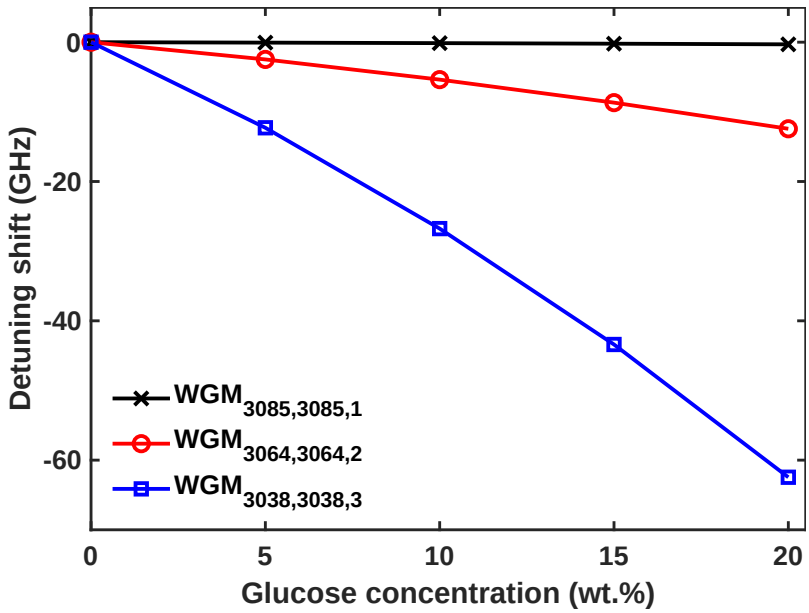

Figure 5.12: Detuning shift of the simulated microbubble WGMs as a function of the glucose ($C_6H_{12}O_6$) concentration expressed in terms of mass fraction.

As a further example of biological fluid sensing, the sensitivity of the microbubble-based setup to different concentrations of an aqueous glucose ($C_6H_{12}O_6$) solution flowing within the bubble has been simulated too. Also in this case, the refractive index of the inner layer of the bubble has been changed as a function of the glucose mass concentration, but at visible wavelength (589 nm). The refractive index dispersion of the aqueous glucose solution is shown in Table 5.2 [126]. In Figure 5.12, the detuning shift of the simulated microbubble WGMs as a function of the glucose concentration is shown. As for the NaCl sensing, the higher the radial order of the WGMs the higher the sensitivity of the bubble to the glucose refractive index variations. The sesnsitivity values, S, calculated from the average slope of the curves in Figure 5.12 are approximately equal to (i) $S = -15.55$ MHz/wt.% for the $WGM_{3085,3085,1}$; (ii) $S = -0.62$ GHz/wt.% for the $WGM_{3064,3064,2}$; (iii) $S = -3.12$ GHz/wt.% for the $WGM_{3038,3038,3}$.

The sensitivity of the simulated microbubble WGMs to the different chemical/biological solutions are large enough for a wavelength shift to be measured by a standard photodetector, especially for high radial order WGMs. By proper microresonator rare-earths doping and/or surface functionalization, even larger sensitivities and higher performance detection can be achieved, allowing for detection of sub-percent concentrations.

5.6 CONCLUDING REMARKS

An exhaustive model for designing a coupling system allowing the wavelength-selective excitation of spatially distributed or quasi-distributed optical WGM microresonators has been investigated. The microresonators are evanescently side-coupled with a fiber taper to increase the coupling efficiency. A pair of identical LPGs, with the microresonator and the tapered fiber in between, can be used to excite the WGMs by means of peculiar cladding modes. The pair of identical LPGs can operate in different wavelength bands allowing multiple selective interrogation of several microresonators along the same optical fiber. The model has been validated with experimental data by considering microsphere- and microbubble-based set-ups. The simulated results are in very good agreement with the experimental ones. They suggest that the investigated coupling system can be effectively used for distributed sensing applications of chemical/biological fluids.

The feasibility investigation of the microbubble-based set-up to monitor different concentrations of sodium chloride (NaCl) and glucose ($C_6H_{12}O_6$) in aqueous solutions has been performed. The detuning shift of the simulated microbubble WGMs as a function of the NaCl and $C_6H_{12}O_6$ concentrations is considered as the sensing response. As an example, the sensitivity $S = -44.16$ GHz/wt.% is obtained for NaCl detection by exciting the $WGM_{1067,1067,3}$, while the sensitivity $S = -3.12$ GHz/wt.% is obtained for $C_6H_{12}O_6$ detection by exciting the $WGM_{3038,3038,3}$.

The theoretical and experimental analysis and results could open up novel opportunities and interesting applications in the fields of the medicine diagnostic and biological investigations. The perspective applications in medicine could be extended to the Mid-IR wavelength range, to detect biomolecules in aqueous solutions, by exploiting tellurite [118] or chalcogenide glasses [37], [116] and by employing innovative sources allowing emission at the suitable wavelengths [71], [127].

CONCLUSION

The design of different microwave and optical resonant structures in the fields of the i) medicine therapy and ii) chemical/biological investigations has been accurately performed via homemade computer codes. The developed homemade codes have been validated via experimental data. Different microwave and optical resonating devices have been considered, the common background being the electromagnetic field theory and the exploitation of the resonance effect to improve their performance.

A flexible and powerful computer code has been developed in order to achieve a more efficient and automated design of the complex microwave resonant cavities of a side-coupled proton linear accelerator. A finite-element numerical method has been integrated with an analytical model which takes into account the periodic nature of the accelerator. Furthermore, a multi-objective particle swarm optimization technique has been exploited for optimizing the accelerator cavities with respect to the design specifications. The proposed hybrid strategy has been validated through frequency and electric field measurements on a 27-MeV 3-GHz side-coupled linac (SCL) tank prototype of five optimized cavities for hadron therapy applications. The simulated and measured resonant frequencies of the SCL tank accelerating mode ($\pi/2$ mode) are practically coincident: $f_{\pi/2,\mathrm{sim}} = 2.997\,916\,\mathrm{GHz}$ and $f_{\pi/2,\mathrm{meas}} = 2.997\,796\,\mathrm{GHz}$, respectively. Moreover, the simulated and measured accelerating electric field nonuniformity is $\sigma_{R,\mathrm{sim}} = 1.806\,\%$ and $\sigma_{R,\mathrm{meas}} = 1.585\,\%$, respectively. The developed hybrid approach is general, and it can be used for designing a wide class of multicavity resonant structures for different applications.

The foregoing hybrid strategy has been indeed applied to the design and optimization of a novel proton linear accelerator based on on-axis coupled electromagnetic band-gap (EBG) cavities for hadron therapy applications. In particular, the design of a 27-MeV 3-GHz EBG tank closed with full end cells has been considered. The simulated frequency of the EBG tank $\pi/2$ mode is $f_{\pi/2,\mathrm{sim}} = 2.998\,09\,\mathrm{GHz}$, very close to the nominal value $f_{\pi/2,\mathrm{ref}} = 2.997\,92\,\mathrm{GHz}$. The calculated stopband is very small, being about 292 kHz. Moreover, an accelerating field nonuniformity as small as $\sigma_{R,\mathrm{sim}} = 1.068\,\%$ has been calculated. The performances of the optimized EBG accelerating cavities has been compared with the performances of the foregoing SCL accelerating cavities. The transit-time factor of the EBG accelerating cavities is about 8 % higher, approaching values typically found in higher energy linac cavities. The Q factor of the EBG accelerating cavities is about 30 % lower; thus higher $\pi/2$ mode frequency and/or higher proton beam input energy are suggested in order to compensate for the higher losses. Furthermore, the maximum value reached by the electric field on the surface of the EBG accelerating cavities is about 65 % lower. Thus, EBG cavities are very promising for the design of high accelerating gradient proton linacs with low RF breakdown probability. By considering the Kilpatrick limit $E_k = 46.8\,\mathrm{MV/m}$ at $f_{\pi/2,\mathrm{ref}}$, a conservative peak surface electric field $E_s = 2E_k$ would allow to increase the accelerating gradient of the EBG tank by about three times ($E_0 = 45\,\mathrm{MV/m}$), thus reducing to one third its length. The longitudinal and transverse wake potentials excited by the proton beam in the EBG and SCL structures have

been simulated and compared too. The results confirm that the EBG structure effectively damps the transverse wake potential due to HOMs.

A comprehensive theoretical model, implemented via a homemade code, has been applied to the design of a coupling system in which a whispering gallery mode (WGM) microresonator is evanescently side-coupled with a tapered optical fiber for efficient coupling. A pair of identical long period gratings (LPGs), with the WGM microresonator and the tapered fiber in between, can be used to excite the WGMs by means of peculiar cladding modes. The pair of identical LPGs can operate in different wavelength bands allowing the wavelength-selective excitation/interrogation of several spatially distributed or quasi-distributed WGM microresonators along the same optical fiber. The theoretical model has been well validated with the experimental data by considering microspheres and microbubbles as WGM microresonators. A very good agreement has been found in terms of both WGM resonances and transmittances. Moreover, the theoretical model allows to retrieve the WGM modal orders. A microbubble-based sensing set-up for sodium chloride (NaCl) and glucose ($C_6H_{12}O_6$) aqueous solutions has been also investigated. The resonance shift of the simulated microbubble WGMs, as a function of the NaCl and $C_6H_{12}O_6$ concentrations, has been considered as the sensor response. The sensitivity $S = -44.16$ GHz/wt.% is obtained for NaCl detection by exciting the $WGM_{1067,1067,3}$, while the sensitivity $S = -3.12$ GHz/wt.% is obtained for $C_6H_{12}O_6$ detection by exciting the $WGM_{3038,3038,3}$. The theoretical and experimental results suggest that the foregoing coupling system can be effectively exploited for distributed sensing applications of chemical and biological fluids.

[1] D. Laneve, M. C. Falconi, M. Bozzetti, G. Rutigliani, R. A. Prisco, V. Dimiccoli, and F. Prudenzano, "Electromagnetic Design of Microwave Cavities for Side-Coupled Linear Accelerators: A Hybrid Numerical/Analytical Approach," *IEEE Trans. Nucl. Sci.*, vol. 65, no. 8, pp. 2233–2239, Aug. 2018.

[2] D. Laneve, M. C. Falconi, M. Bozzetti, G. Rutigliani, V. Dimiccoli, R. A. Prisco, and F. Prudenzano, "Efficient hybrid approach to the electromagnetic design of resonant cavities for side-coupled linacs," *IET J. Eng.*, vol. 2019, no. 6, pp. 4617–4621, Mar. 2019.

[3] D. Laneve, V. Portosi, M. C. Falconi, G. Rutigliani, R. A. Prisco, V. Dimiccoli, and F. Prudenzano, "Design of Electromagnetic Band-Gap Cavities for High-Gradient On-Axis Coupled-Cavity Linear Accelerators," *IEEE Trans. Nucl. Sci.*, Oct. 2019, *submitted*.

[4] F. Chiavaioli, D. Laneve, D. Farnesi, M. C. Falconi, G. Nunzi Conti, F. Baldini, and F. Prudenzano, "Long Period Grating-Based Fiber Coupling to WGM Microresonators," *Micromachines*, vol. 9, no. 7, 366, Jul. 2018.

[5] D. Laneve, M. C. Falconi, G. Palma, C. Scarnera, F. Chiavaioli, D. Farnesi, T. Kishi, A. Chiappini, G. Nunzi Conti, S. Soria, V. Nazabal, F. Baldini, M. Ferrari, and F. Prudenzano, "Passive and active whispering gallery mode microresonators in optical engineering," in *Proc. SPIE 2019*, San Francisco, CA, US, 2019.

[6] D. Laneve, M. C. Falconi, F. Chiavaioli, D. Farnesi, G. Nunzi Conti, S. Soria, F. Baldini, and F. Prudenzano, "Optical coupling of spherical microresonators with tapered fibers for chemical/biomedical applications," in *Proc. MetroSea 2018*, Bari, Italy, 2018.

[7] M. Grande, G. V. Bianco, D. Laneve, P. Capezzuto, V. Petruzzelli, M. Scalora, F. Prudenzano, G. Bruno, and A. D'Orazio, "Optically transparent wideband CVD graphene-based microwave antennas," *Appl. Phys. Lett.*, vol. 112, no. 25, 251103, Jun. 2018.

[8] M. Grande, G. V. Bianco, D. Laneve, P. Capezzuto, M. Scalora, V. Petruzzelli, F. Prudenzano, G. Bruno, and A. D'Orazio, "Gain and phase control in a graphene-loaded reconfigurable antenna," *Appl. Phys. Lett.*, vol. 115, no. 13, 133103, Sep. 2019.

[9] M. C. Falconi, D. Laneve, M. Bozzetti, T. T. Fernandez, G. Galzerano, and F. Prudenzano, "Design of an Efficient Pulsed Dy^{3+}:ZBLAN Fiber Laser Operating in Gain Switching Regime," *J. Lightw. Technol.*, vol. 36, no. 23, pp. 5327–5333, Dec. 2018.

[10] M. C. Falconi, D. Laneve, V. Portosi, S. Taccheo, and F. Prudenzano, "Design of a Multi-wavelength Fiber Laser Based on Tm:Er:Yb:Ho Co-doped Germanate Glass," *J. Lightw. Technol.*, Jan. 2020, *early access*.

[11] A. Ivanov, T. Agliullin, D. Laneve, V. Portosi, A. Vorobev, R. R. Nigmatullin, A. Nasybullin, O. Morozov, F. Prudenzano, A. D'Orazio, and M. Grande, "Design and Characterization of a Microwave Planar Sensor for Dielectric Assessment of Vegetable Oils," *Electronics*, vol. 8, no. 9, 1030, Sep. 2019.

[12] M. C. Falconi, D. Laneve, and F. Prudenzano, "Advances in Mid-IR Fiber Lasers: Tellurite, Fluoride and Chalcogenide," *Fibers*, vol. 5, no. 2, pp. 23–34, Jun. 2017.

[13] V. Portosi, D. Laneve, M. C. Falconi, and F. Prudenzano, "Advances on Photonic Crystal Fiber Sensors and Applications," *Sensors*, vol. 19, no. 8, 1892, Apr. 2019.

[14] A. Degiovanni and U. Amaldi, "History of hadron therapy accelerators," *Phys. Med.*, vol. 31, no. 4, pp. 322–332, Jun. 2015.

[15] U. Amaldi, R. Bonomi, S. Braccini, M. Crescenti, A. Degiovanni, M. Garlasché, A. Garonna, G. Magrin, C. Mellace, P. Pearce, G. Pittà, P. Puggioni, E. Rosso, S. V. Andrés, R.Wegner, M.Weiss, and R. Zennaro, "Accelerators for hadrontherapy: From Lawrence cyclotrons to linacs," *Nucl. Instrum. Methods Phys. Res. A, Accel. Spectrom. Detect. Assoc. Equip.*, vol. 620, no. 2–3, pp. 563–577, Aug. 2010.

[16] U. Amaldi and G. Kraft, "Radiotherapy with beams of carbon ions," *Rep. Prog. Phys.*, vol. 68, no. 8, pp. 1861–1882, Jul. 2005.

[17] T. P. Wangler, *RF Linear Accelerators*, 2nd ed. Weinheim, Germany: Wiley, 2008.

[18] U. Amaldi, P. Berra, K. Crandall, D. Toet, M. Weiss, R. Zennaro, E. Rosso, B. Szeless, M. Vretenar, C. Cicardi, C. D. Martinis, D. Giove, D. Davino, M. R. Masullo, and V. Vaccaro, "LIBO–A linac-booster for protontherapy: Construction and tests of a prototype," *Nucl. Instrum. Methods Phys. Res. A, Accel. Spectrom. Detect. Assoc. Equip.*, vol. 521, no. 2–3, pp. 512–529, Apr. 2004.

[19] E. A. Knapp, B. C. Knapp, and J. M. Potter, "Standing Wave High Energy Linear Accelerator Structures," *Rev. Sci. Instrum.*, vol. 39, no. 7, pp. 979–991, Jul. 1968.

[20] C. Ronsivalle, M. Carpanese, C. Marino, G. Messina, L. Picardi, S. Sandri, E. Basile, B. Caccia, D. M. Castelluccio, E. Cisbani, S. Frullani, F. Ghio, V. Macellari, M. Benassi, M. D'Andrea, and L. Strigari, "The TOP-IMPLART Project," *Eur. Phys. J. Plus*, vol. 126, no. 68, pp. 1–15, Jul. 2011.

[21] C. D. Martinis, D. Giove, U. Amaldi, P. Berra, K. Crandall, M. Mauri, M. Weiss, R. Zennaro, E. Rosso, B. Szeless, M. Vretenar, M. R. Masullo, V. Vaccaro, L. Calabretta, and A. Rovelli, "Acceleration tests of a 3 GHz proton linear accelerator (LIBO) for hadrontherapy," *Nucl. Instrum. Methods Phys. Res. A, Accel. Spectrom. Detect. Assoc. Equip.*, vol. 681, pp. 10–15, Jul. 2012.

[22] U. Amaldi, S. Braccini, and P. Puggioni, "High frequency linacs for hadrontherapy," *Rev. Accel. Sci. Technol.*, vol. 2, no. 1, pp. 111–131, 2009.

[23] V. G. Vaccaro, M. R. Masullo, C. D. Martinis, D. Giove, A. Rainò, V. Variale, S. Mathot, R. J. Rush, and M. Iskander, "RF high power tests on the first module of ACLIP linac," in *Proc. PAC09*, Vancouver, BC, Canada, 2009.

[24] ITEL/Linearbeam S.r.l. (Apr. 2019), [Online]. Available: `https://www.itelte.it/en/cnt/protontherapy`.

[25] S. Arnold, M. Khoshsima, I. Teraoka, S. Holler, and F. Vollmer, "Shift of whispering-gallery modes in microspheres by protein adsorption," *Opt. Lett.*, vol. 28, no. 4, pp. 272–274, Feb. 2003.

[26] A. M. Armani, R. P. Kulkarni, S. E. Fraser, R. C. Flagan, and K. J. Vahala, "Label-Free, Single-Molecule Detection with Optical Microcavities," *Science*, vol. 317, no. 5839, pp. 783–787, Aug. 2007.

[27] S. Soria, S. Berneschi, M. Brenci, F. Cosi, G. Nunzi Conti, S. Pelli, and G. C. Righini, "Optical Microspherical Resonators for Biomedical Sensing," *Sensors*, vol. 11, no. 1, pp. 785–805, Jan. 2011.

[28] J. D. Suter, D. J. Howard, H. Shi, C. W. Caldwell, and X. Fan, "Label-free DNA methylation analysis using opto-fluidic ring resonators," *Biosens. Bioelectron.*, vol. 26, no. 3, pp. 1016–1020, Nov. 2010.

[29] V. Donzella and F. Crea, "Optical biosensors to analyze novel biomarkers in oncology," *J. Biophotonics*, vol. 4, no. 6, pp. 442–452, May 2011.

[30] H. A. Huckabay, S. M. Wildgen, and R. C. Dunn, "Label-free detection of ovarian cancer biomarkers using whispering gallery mode imaging," *Biosens. Bioelectron.*, vol. 45, pp. 223–229, Jul. 2013.

[31] Y. Shin, R. A. Soo, J. Yoon, A. P. Perera, Y.-J. Yoon, and M. K. Park, "Rapid and label-free amplification and detection assay for genotyping of cancer biomarker," *Biosens. Bioelectron.*, vol. 68, pp. 107–114, Jun. 2015.

[32] W. Pongruengkiat and S. Pechprasarn, "Whispering-Gallery Mode Resonators for Detecting Cancer," *Sensors*, vol. 17, no. 9, 2095, Sep. 2017.

[33] N. Ismail, C. C. Kores, D. Geskus, and M. Pollnau, "Fabry-Pérot resonator: Spectral line shapes, generic and related Airy distributions, linewidths, finesses, and performance at low or frequency-dependent reflectivity," *Opt. Express*, vol. 24, no. 15, pp. 16 366–16 389, Jul. 2016.

[34] G. Yang, I. M. White, and X. Fan, "An opto-fluidic ring resonator biosensor for the detection of organophosphorus pesticides," *Sens. Actuator B Chem.*, vol. 133, no. 1, pp. 105–112, Jul. 2008.

[35] F. Meziane, V. Raimbault, H. Hallil, S. Joly, V. Conédéra, L. Béchou, D. Rebière, and C. Dejous, "Study of a polymer optical microring resonator for hexavalent chromium sensing," *Sens. Actuator B Chem.*, vol. 209, pp. 1049–1056, Mar. 2015.

[36] A. Schweinsberg, S. Hocdé, N. N. Lepeshkin, R. W. Boyd, C. Chase, and J. E. Fajardo, "An environmental sensor based on an integrated optical whispering gallery mode disk resonator," *Sens. Actuator B Chem.*, vol. 123, no. 2, pp. 727–732, May 2007.

[37] G. Palma, M. C. Falconi, F. Starecki, V. Nazabal, J. Ari, L. Bodiou, J. Charrier, Y. Dumeige, E. Baudet, and F. Prudenzano, "Design of praseodymium-doped chalcogenide micro-disk emitting at 4.7μm," *Opt. Express*, vol. 25, no. 6, pp. 7014–7030, Mar. 2017.

[38] H. Wang, L. Yuan, C.-W. Kim, X. Lan, J. Huang, Y. Ma, and H. Xiao, "Integrated chemical vapor sensor based on thin wall capillary coupled porous glass microsphere optical resonator," *Sens. Actuator B Chem.*, vol. 216, pp. 332–336, Sep. 2015.

[39] Z. Ballard, M. D. Baaske, and F. Vollmer, "Stand-Off Biodetection with Free-Space Coupled Asymmetric Microsphere Cavities," *Sensors*, vol. 15, no. 4, pp. 8968–8980, Apr. 2015.

[40] S. Berneschi, D. Farnesi, F. Cosi, G. Nunzi Conti, S. Pelli, G. C. Righini, and S. Soria, "High Q silica microbubble resonators fabricated by arc discharge," *Opt. Lett.*, vol. 36, no. 17, pp. 3521–3523, Sep. 2011.

[41] A. Barucci, S. Berneschi, A. Giannetti, F. Baldini, A. Cosci, S. Pelli, D. Farnesi, G. C. Righini, S. Soria, and G. Nunzi Conti, "Optical Microbubble Resonators with High Refractive Index Inner Coating for Bio-Sensing Applications: An Analytical Approach," *Sensors*, vol. 16, no. 12, 1992, Nov. 2016.

[42] M. Hossein-Zadeh and K. J. Vahala, "Free ultra-high-Q microtoroid: A tool for designing photonic devices," *Opt. Express*, vol. 15, no. 1, pp. 166–175, Jan. 2007.

[43] J. Su, A. F. G. Goldberg, and B. M. Stoltz, "Label-free detection of single nanoparticles and biological molecules using microtoroid optical resonators," *Light Sci. Appl.*, vol. 5, e16001, Jan. 2016.

[44] G. Righini, Y. Dumeige, P. Féron, M. Ferrari, G. Nunzi Conti, D. Ristic, and S. Soria, "Whispering gallery mode microresonators: Fundamentals and applications," *Riv. Nuovo Cimento*, vol. 34, no. 7, pp. 435–488, Jun. 2011.

[45] D. M. Pozar, *Microwave Engineering*, 4th ed. Hoboken, NJ, USA: Wiley, 2011.

[46] J. Gao, "Analytical formulas for the resonant frequency changes due to opening apertures on cavity walls," *Nucl. Instrum. Methods Phys. Res. A, Accel. Spectrom. Detect. Assoc. Equip.*, vol. 311, no. 3, pp. 437–443, Jan. 1992.

[47] R. Roy and O. Shanker, "Calculation of intercavity coupling coefficient for side coupled standing wave linear accelerator," *IEEE Trans. Microw. Theory Techn.*, vol. 41, no. 6, pp. 1233–1235, Jun. 1993.

[48] P. Greninger, "Next nearest neighbor coupling in side-coupled linacs based on analytical expressions," *Phys. Rev. ST Accel. Beams*, vol. 5, no. 10, 102001, Oct. 2002.

[49] P. M. Lapostolle and A. L. Septier, Eds., *Linear accelerators*. Amsterdam, The Netherlands: North Holland, 1970.

[50] W. D. Kilpatrick, "Criterion for Vacuum Sparking Designed to Include Both rf and dc," *Rev. Sci. Instrum.*, vol. 28, no. 10, pp. 824–826, Oct. 1957.

[51] D. E. Nagle, E. A. Knapp, and B. C. Knapp, "Coupled Resonator Model for Standing Wave Accelerator Tanks," *Rev. Sci. Instrum.*, vol. 38, no. 11, pp. 1583–1587, Nov. 1967.

[52] C. A. Balanis, *Advanced Engineering Electromagnetics*, 2nd ed. Hoboken, NJ, USA: Wiley, 2012.

[53] O. Shanker, "Generalization of linac mode spectrum and fitting procedure," *Rev. Sci. Instrum.*, vol. 63, no. 10, pp. 4443–4445, Oct. 1992.

[54] O. Shanker, P. A. R. Chowdhuri, and R. Verma, "Coupling coefficient informations from the linac-mode spectrum," *Rev. Sci. Instrum.*, vol. 60, no. 10, pp. 3301–3303, Oct. 1989.

[55] R. Krishnan, S. N. Pethe, R. Roy, and 0. Shanker, "Analysis of side coupled standing wave linear accelerator structure by the perturbation method," *IEEE Trans. Nucl. Sci.*, vol. 40, no. 5, pp. 1333–1336, Oct. 1993.

[56] A. D'Elia, M. R. Masullo, and V. G. Vaccaro, "An analysis of lumped circuit equation for side coupled linac (SCL)," in *Proc. EPAC06*, Edinbourgh, UK, 2006, pp. 1600–1602.

[57] R. W. de Leeuw, J. E. Coppens, W. J. G. M. Kleeven, C. J. Timmermans, and J. I. M. Botman, "Design Study for the Accelerating Cavity of the Racetrack Microtron Eindhoven," in *Proc. EPAC99*, London, UK, 1994, pp. 2092–2094.

[58] D. Zhao, X. Lu, Y. Liang, X. Yang, C. Ruan, and Y. Ding, "Researches on an X-Band Sheet Beam Klystron," *IEEE Trans. Electron Devices*, vol. 61, no. 1, pp. 151–158, Jan. 2014.

[59] Y.-M. Shin, L. R. Barnett, and N. C. Luhmann, "Quasi-optical output-cavity design for a 50-kW multicavity W-band sheet-beam klystron," *IEEE Trans. Electron Devices*, vol. 56, no. 12, pp. 3196–3202, Dec. 2009.

[60] Y.-M. Shin, J.-X. Wang, L. R. Barnett, and N. C. Luhmann, "Particle-in-cell simulation analysis of a multicavity W-band sheet beam klystron," *IEEE Trans. Electron Devices*, vol. 58, no. 1, pp. 251–258, Jan. 2011.

[61] M. E. Read, V. Jabotinski, G. Miram, and L. Ives, "Design of a gridded gun and PPM-focusing structure for a high-power sheet electron beam," *IEEE Trans. Plasma Sci.*, vol. 33, no. 2, pp. 647–653, Apr. 2005.

[62] K. W. Lee, J. G. Jeong, Y. J. Yoon, J. H. Kim, and C. Kook, "Analysis of the quality factor of input cavity with intense beam loading in a relativistic vacuum tube," *IET Sci. Meas. Technol.*, vol. 11, no. 2, pp. 141–148, Mar. 2017.

[63] H. Nowakowska, M. Jasinski, P. S. Debicki, and J. Mizeraczyk, "Numerical Analysis and Optimization of Power Coupling Efficiency in Waveguide-Based Microwave Plasma Source," *IEEE Trans. Plasma Sci.*, vol. 39, no. 10, pp. 1935–1942, Oct. 2011.

[64] Y. Wu, Z. Xu, X. Jin, Z.-H. Li, and C.-X. Tang, "A Long Pulse Relativistic Klystron Amplifier Driven by Low RF Power," *IEEE Trans. Plasma Sci.*, vol. 40, no. 10, pp. 2762–2766, Oct. 2012.

[65] K. R. Shin, Y. W. Kang, and A. E. Fathy, "Design Guidelines of a Double-Gap Microwave Rebuncher Cavity for a 400 MHz, 2.5 MeV Energy Light Ion Accelerator with Lower Gap Voltage and Field," *IEEE Trans. Nucl. Sci.*, vol. 61, no. 2, pp. 817–823, Apr. 2014.

[66] Y. Zhang, K. Huang, D. K. Agrawal, T. Slawecki, H. Zhu, and Y. Yang, "Microwave Power System Based a Combination of Two Magnetrons," *IEEE Trans. Electron Devices*, vol. 64, no. 10, pp. 4272–4278, Oct. 2017.

[67] E. A. Knapp, "Resonantly Coupled Standing Wave Accelerator Structures for Electron and Proton Linac Applications," *IEEE Trans. Nucl. Sci.*, vol. NS-16, no. 3, pp. 329–337, Jun. 1969.

[68] S. Benedetti, A. Grudiev, and A. Latina, "High gradient linac for proton therapy," *Phys. Rev. Accel. Beams*, vol. 20, no. 4, 040101, Apr. 2017.

[69] J. Kennedy and R. C. Eberhart, *Swarm Intelligence*. San Francisco, CA, USA: Morgan Kaufmann, 2001.

[70] J. Robinson and Y. Rahmat-Samii, "Particle Swarm Optimization in Electromagnetics," *IEEE Trans. Antennas Propag.*, vol. 52, no. 2, pp. 397–407, Feb. 2004.

[71] M. C. Falconi, G. Palma, F. Starecki, V. Nazabal, J. Troles, J.-L. Aadam, S. Taccheo, M. Ferrari, and F. Prudenzano, "Dysprosium-Doped Chalcogenide Master Oscillator Power Amplifier (MOPA) for Mid-IR Emission," *J. Lightw. Technol.*, vol. 35, no. 2, pp. 265–273, Jan. 2017.

[72] S. Dehuri, A. K. Jagadev, and M. Panda, Eds., *Multi-objective Swarm Intelligence*. Berlin, Germany: Springer-Verlag, 2009.

[73] C. A. Coello Coello, G. T. Pulido, and M. S. Lechuga, "Handling Multiple Objectives with Particle Swarm Optimization," *IEEE Trans. Evol. Comput.*, vol. 8, no. 3, pp. 256–279, Jun. 2004.

[74] L. Picardi, C. Ronsivalle, and A. Vignati, "Progetto del TOP LINAC," ENEA Res. Centre, Frascati, Italy, Tech. Rep. RT/INN/97/17, Jul. 1997.

[75] C. A. Coello Coello, G. B. Lamont, and D. A. van Veldhuizen, *Evolutionary Algorithms for Solving Multi-Objective Problems*, 2nd ed. New York, NY, USA: Springer, 2007.

[76] L. C. Maier Jr. and J. C. Slater, "Field Strength Measurements in Resonant Cavities," *J. Appl. Phys.*, vol. 23, no. 1, pp. 68–77, Feb. 1952.

[77] Y. Kasahara, H. Toyao, and E. Hankui, "Compact and Multiband Electromagnetic Bandgap Structures With Adjustable Bandgaps Derived From Branched Open-Circuit Lines," *IEEE Trans. Microw. Theory Techn.*, vol. 65, no. 7, pp. 2330–2340, Jul. 2017.

[78] P.-S. Wei, M.-H. Tsai, S.-K. Hsu, C.-K. Shen, and T.-L. Wu, "An Electromagnetic Bandgap Structure Integrated With RF LNA Using Integrated Fan-Out Wafer-Level Package for Gigahertz Noise Suppression," *IEEE Trans. Microw. Theory Techn.*, vol. 66, no. 12, pp. 5482–5490, Dec. 2018.

[79] I. Ederra, I. Khromova, R. Gonzalo, N. Delhote, D. Baillargeat, A. Murk, B. E. J. Alderman, and P. de Maagt, "Electromagnetic-Bandgap Waveguide for the Millimeter Range," *IEEE Trans. Microw. Theory Techn.*, vol. 58, no. 7, pp. 1734–1741, Jul. 2010.

[80] H. U. Habiba, K. Malathi, M. H. Masood, and R. Kunnath, "Tunable electromagnetic band gap-embedded multimode resonators for ultra-wideband dual band, lower-ultra-wideband and upper-ultra-wideband applications," *IET Microw. Antennas Propag.*, vol. 5, no. 10, pp. 1182–1187, Jul. 2011.

[81] J. de Dios Ruiz, F. L. Martínez-Viviente, A. Alvarez-Melcon, and J. Hinojosa, "Substrate Integrated Waveguide (SIW) With Koch Fractal Electromagnetic Bandgap Structures (KFEBG) for Bandpass Filter Design," *IEEE Microw. Wireless Compon. Lett.*, vol. 25, no. 3, pp. 160–162, Mar. 2015.

[82] Y. Guo, S. Kim, H. Gao, and G. Li, "Compact High Q Configurable Quint-Band Electromagnetic Bandgap Filter," *IEEE Access*, vol. 6, pp. 63 703–63 711, Oct. 2018.

[83] B. A. Zeb, Y. Ge, K. P. Esselle, Z. Sun, and M. E. Tobar, "A Simple Dual-Band Electromagnetic Band Gap Resonator Antenna Based on Inverted Reflection Phase Gradient," *IEEE Trans. Antennas Propag.*, vol. 60, no. 10, pp. 4522–4529, Oct. 2012.

[84] W. Chen, C. A. Balanis, and C. R. Birtcher, "Checkerboard EBG Surfaces for Wideband Radar Cross Section Reduction," *IEEE Trans. Antennas Propag.*, vol. 63, no. 6, pp. 2636–2645, Jun. 2015.

[85] C. Huang, C. Ji, X. Wu, J. Song, and X. Luo, "Combining FSS and EBG Surfaces for High-Efficiency Transmission and Low-Scattering Properties," *IEEE Trans. Antennas Propag.*, vol. 66, no. 3, pp. 1628–1632, Mar. 2018.

[86] S. Y. Jun, B. S. Izquierdo, and E. A. Parker, "Liquid Sensor/Detector Using an EBG Structure," *IEEE Trans. Antennas Propag.*, vol. 67, no. 5, pp. 3366–3373, May 2019.

[87] M. A. Shapiro, W. J. Brown, I. Mastovsky, J. R. Sirigiri, and R. J. Temkin, "17 GHz photonic band gap cavity with improved input coupling," *Phys. Rev. Accel. Beams*, vol. 4, no. 4, 042001, Apr. 2001.

[88] E. I. Smirnova, A. S. Kesar, I. Mastovsky, M. A. Shapiro, and R. J. Temkin, "Demonstration of a 17-GHz, high-gradient accelerator with a photonic-band-gap structure," *Phys. Rev. Lett.*, vol. 95, no. 7, 074801, Aug. 2005.

[89] E. I. Smirnova, I. Mastovsky, M. A. Shapiro, R. J. Temkin, L. M. Earley, and R. L. Edwards, "Fabrication and cold test of photonic band gap resonators and accelerator structures," *Phys. Rev. ST Accel. Beams*, vol. 8, no. 9, 091302, Sep. 2005.

[90] B. J. Munroe, J. Zhang, H. Xu, M. A. Shapiro, and R. J. Temkin, "Experimental high gradient testing of a 17.1 GHz photonic band-gap accelerator structure," *Phys. Rev. Accel. Beams*, vol. 19, no. 3, 031301, Mar. 2016.

[91] M. R. Masullo, A. Andreone, E. D. Gennaro, S. Albanese, F. Francomacaro, M. Panniello, V. G. Vaccaro, and G. Lamura, "Study of Hybrid Photonic Band Gap Resonators for Particle Accelerators," *Microw. Opt. Technol. Lett.*, vol. 48, no. 12, pp. 2486–2491, Dec. 2006.

[92] E. D. Gennaro, S. Savo, A. Andreone, V. Galdi, G. Castaldi, V. Pierro, and M. R. Masullo, "Mode confinement in photonic quasicrystal point-defect cavities for particle accelerators," *Appl. Phys. Lett.*, vol. 93, no. 16, 164102, Oct. 2008.

[93] E. D. Gennaro, C. Zannini, S. Savo, A. Andreone, M. R. Masullo, G. Castaldi, I. Gallina, and V. Galdi, "Hybrid photonic-bandgap accelerating cavities," *New J. Phys.*, vol. 11, 113022, Nov. 2009.

[94] J. Zhang, B. J. Munroe, H. Xu, M. A. Shapiro, and R. J. Temkin, "High power experimental studies of hybrid photonic band gap accelerator structures," *Phys. Rev. Accel. Beams*, vol. 19, no. 8, 081304, Aug. 2016.

[95] M. Hu, B. J. Munroe, M. A. Shapiro, and R. J. Temkin, "Calculation of wakefields in a 17 GHz beam-driven photonic band-gap accelerator structure," *Phys. Rev. ST Accel. Beams*, vol. 16, no. 2, 022002, Feb. 2013.

[96] C. A. Bauer, G. R. Werner, and J. R. Cary, "Origin and reduction of wakefields in photonic crystal accelerator cavities," *Phys. Rev. ST Accel. Beams*, vol. 17, no. 5, 051301, May 2014.

[97] L. Mescia, P. Bia, O. Losito, and F. Prudenzano, "Design of Mid-IR Er^{3+}-Doped Microsphere Laser," *IEEE Photon. J.*, vol. 5, no. 4, 1501308, Aug. 2013.

[98] A. Chiasera, Y. Dumeige, P. Féron, M. Ferrari, Y. Jestin, G. Nunzi Conti, S. Pelli, S. Soria, and G. C. Righini, "Spherical whispering-gallery-mode microresonators," *Laser & Photon. Rev.*, vol. 4, no. 3, pp. 457–482, Apr. 2010.

[99] P. Girault, N. Lorrain, J. Lemaitre, L. Poffo, M. Guendouz, I. Hardy, M. Gadonna, A. Gutierrez, L. Bodiou, and J. Charrier, "Racetrack micro-resonators based on ridge waveguides made of porous silica," *Opt. Mater.*, vol. 50, pp. 167–174, Dec. 2015.

[100] Y. Jestin, C. Armellini, A. Chiappini, A. Chiasera, Y. Dumeige, M. Ferrari, P. Féron, L. Ghisa, G. Nunzi Conti, S. Trebaol, and G. C. Righini, "Photonic properties of erbium activated coated microspheres," in *Proc. SPIE 2008*, San Jose, CA, USA, 2008.

[101] J. C. Knight, G. Cheung, F. Jacques, and T. A. Birks, "Phase-matched excitation of whispering-gallery-mode resonances by a fiber taper," *Opt. Lett.*, vol. 22, no. 15, pp. 1129–1131, Aug. 1997.

[102] M. Cai, O. Painter, and K. J. Vahala, "Observation of Critical Coupling in a Fiber Taper to a Silica-Microsphere Whispering-Gallery Mode System," *Phys. Rev. Lett.*, vol. 85, no. 1, pp. 74–77, Jul. 2000.

[103] M. Cai and K. Vahala, "Highly efficient hybrid fiber taper coupled microsphere laser," *Opt. Lett.*, vol. 26, no. 12, pp. 884–886, Jun. 2001.

[104] B. E. Little, J.-P. Laine, and H. A. Haus, "Analytic Theory of Coupling from Tapered Fibers and Half-Blocks into Microsphere Resonators," *J. Lightw. Technol.*, vol. 17, no. 4, pp. 704–715, Apr. 1999.

[105] H. A. Haus, W. P. Huang, S. Kawakami, and N. A. Whitaker, "Coupled-Mode Theory of Optical Waveguides," *J. Lightw. Technol.*, vol. LT-5, no. 1, pp. 16–23, Jan. 1987.

[106] H. A. Haus, *Waves and Fields in Optoelectronics*. Englewood Cliffs, NJ, USA: Prentice-Hall, 1984.

[107] G. P. Agrawal, *Fiber-Optic Communications Systems*, 4th ed. Hoboken, NJ, USA: Wiley, 2010.

[108] B. E. Little, S. T. Chu, H. A. Haus, J. Foresi, and J.-P. Laine, "Microring Resonator Channel Dropping Filters," *J. Lightw. Technol.*, vol. 15, no. 6, pp. 998–1005, Jun. 1997.

[109] B. Özel, R. Nett, T. Weigel, G. Schweiger, and A. Ostendorf, "Temperature sensing by using whispering gallery modes with hollow core fibers," *Meas. Sci. Technol.*, vol. 21, no. 9, pp. 094 015–094 020, Jul. 2010.

[110] J. M. Ward, Y. Yang, and S. N. Chormaic, "Highly Sensitive Temperature Measurements With Liquid-Core Microbubble Resonators," *IEEE Photon. Technol. Lett.*, vol. 25, no. 23, pp. 2350–2353, Dec. 2013.

[111] Q. Ma, T. Rossmann, and Z. Guo, "Whispering-gallery mode silica microsensors for cryogenic to room temperature measurement," *Meas. Sci. Technol.*, vol. 21, no. 2, pp. 025 310–025 317, Jan. 2010.

[112] Z. P. Cai, L. Xiao, H. Y. Xu, and M. Mortier, "Point temperature sensor based on green decay in an Er:ZBLALiP microsphere," *J. Lumin.*, vol. 129, no. 12, pp. 1994–1996, Dec. 2009.

[113] C.-H. Dong, L. He, Y.-F. Xiao, V. R. Gaddam, S. K. Ozdemir, Z.-F. Han, G.-C. Guo, and L. Yang, "Fabrication of high-Q polydimethylsiloxane optical microspheres for thermal sensing," *Appl. Phys. Lett.*, vol. 94, no. 23, pp. 231 119–231 121, Jun. 2009.

[114] N. M. Hanumegowda, C. J. Stica, B. C. Patel, I. White, and X. Fan, "Refractometric sensors based on microsphere resonators," *Appl. Phys. Lett.*, vol. 87, no. 20, pp. 201 107–201 110, Nov. 2005.

[115] R. Henze, T. Seifert, J. Ward, and O. Benson, "Tuning whispering gallery modes using internal aerostatic pressure," *Opt. Lett.*, vol. 36, no. 23, pp. 4536–4538, Nov. 2011.

[116] G. Palma, C. Falconi, V. Nazabal, T. Yano, T. Kishi, T. Kumagai, M. Ferrari, and F. Prudenzano, "Modeling of Whispering Gallery Modes for Rare Earth Spectroscopic Characterization," *IEEE Photon. Technol. Lett.*, vol. 27, no. 17, pp. 1861–1863, Sep. 2015.

[117] F. Vollmer and S. Arnold, "Whispering-gallery-mode biosensing: Label-free detection down to single molecules," *Nat. Methods*, vol. 5, pp. 591–596, Jun. 2008.

[118] T. Kishi, T. Kumagai, S. Shibuya, F. Prudenzano, T. Yano, and S. Shibata, "Quasi-single mode laser output from a terrace structure added on a Nd^{3+}-doped tellurite-glass microsphere prepared using localized laser heating," *Opt. Express*, vol. 23, no. 16, pp. 20 629–20 635, Jul. 2015.

[119] D. Farnesi, F. Chiavaioli, G. C. Righini, S. Soria, C. Trono, P. Jorge, and G. Nunzi Conti, "Long period grating-based fiber coupler to whispering gallery mode resonators," *Opt. Lett.*, vol. 39, no. 22, pp. 6525–6528, Nov. 2014.

[120] D. Farnesi, F. Chiavaioli, F. Baldini, G. C. Righini, S. Soria, C. Trono, and G. Nunzi Conti, "Quasi-distributed and wavelength selective addressing of optical micro-resonators based on long period fiber gratings," *Opt. Express*, vol. 23, no. 16, pp. 21 175–21 180, Aug. 2015.

[121] M. Brenci, R. Calzolai, F. Cosi, G. Nunzi Conti, S. Pelli, and G. C. Righini, "Microspherical resonators for biophotonic sensors," in *Proc. SPIE 2004*, Warsaw, Poland, 2004.

[122] C. Trono, F. Baldini, M. Brenci, F. Chiavaioli, and M. Mugnaini, "Flow cell for strain- and temperature-compensated refractive index measurements by means of cascaded optical fibre long period and Bragg gratings," *Meas. Sci. Technol.*, vol. 22, no. 7, 075204, Jun. 2011.

[123] I. H. Malitson, "Interspecimen Comparison of the Refractive Index of Fused Silica," *J. Opt. Soc. Am.*, vol. 55, no. 10, pp. 1205–1209, Aug. 1965.

[124] J. E. Saunders, C. Sanders, H. Chen, and H.-P. Loock, "Refractive indices of common solvents and solutions at 1550 nm," *Appl. Opt.*, vol. 55, no. 4, pp. 947–953, Feb. 2016.

[125] G. Palma, M. C. Falconi, F. Starecki, V. Nazabal, T. Yano, T. Kishi, T. Kumagai, and F. Prudenzano, "Novel double step approach for optical sensing via microsphere WGM resonance," *Opt. Express*, vol. 24, no. 23, pp. 26 956–26 971, Nov. 2016.

[126] D. R. Lide, Ed., *CRC Handbook of Chemistry and Physics*, 85th ed. Boca Raton, FL, USA: CRC Press, 2003.

[127] M. C. Falconi, G. Palma, F. Starecki, V. Nazabal, J. Troles, S. Taccheo, M. Ferrari, and F. Prudenzano, "Design of an Efficient Pumping Scheme for Mid-IR Dy^{3+}: $Ga_5Ge_20Sb_10S_65$ PCF Fiber Laser," *IEEE Photon. Technol. Lett.*, vol. 28, no. 18, pp. 1984–1987, Sep. 2016.